NTNU

Norwegian University of
Science and Technology

Autonomous navigation of an ROV using tightly coupled integration of inertial and pseudo-range measurements

Katrine Seel

Marine Technology
Submission date: June 2017
Supervisor: Ingrid Schjølberg, IMT
Co-supervisor: Brede Thorkildsen, TechnipFMC
Stian Skaalvik Sandøy, IMT

Norwegian University of Science and Technology
Department of Marine Technology

NTNU Trondheim
Norwegian University of Science and Technology
Department of Marine Technology

MASTER THESIS IN MARINE CYBERNETICS

SPRING 2017

for

STUD. TECH KATRINE SEEL

Autonomous navigation of an ROV using tightly coupled integration of inertial and pseudo-range measurements

Work description

Remotely Operated Vehicles (ROVs) are used in a number of operations performed subsea, ranging from the oil and gas industry, to fisheries and aquaculture as well as in subsea mining. Especially the subsea oil and gas industry has come to rely on ROVs for conducting Intervention, Maintenance and Repair (IMR) operations.

Today, human operators, with the use of joysticks, control ROVs manually. Consequently, the costs incurred for proper training of ROV operators as well as using these to operate offshore, become high. In addition to the costs, the possibility of human error also becomes a risk. It is therefore desirable to make operation of ROVs more autonomous, by introducing more automatic functions that can be performed independent of an ROV operator.

Accurate underwater navigation systems will be essential in order to achieve successful autonomous operation of ROVs and is considered in this master thesis. Two different filters will be developed to solve integration of inertial and pseudo-range measurements. The implementation of the integration filters will be verified in simulations, and in addition their performance will be compared. Finally, both filters will be tested in offline runs using experimental data collected during two separate experiments conducted in the test basin in the Marine Cybernetics Laboratory at Tyholt, NTNU.

Scope of work:

1. Literature review of specific topics relevant for the thesis work. The main focus is on underwater navigation, with emphasis on the following

a. Overview of state of the art underwater navigation
b. Range-aided inertial navigation
c. State estimation using integration of inertial and range-based measurements

2. Modify the three-stage filter (TSF) for integration of inertial measurements and pseudo-range acoustic measurements described in the work by B. Stovner et al. (2016), so that acceleration biases also are estimated. In addition, implement an Extended Kalman Filter (EKF) for estimation of the same states, and use this as basis for comparison.

3. Develop a kinematic ROV simulator that generates the necessary measurements, and that can be used for testing the filters. Verify the implementation of the TSF and EKF in simulations, and compare their performance.

4. Perform experimental work in the MC-laboratory, and log sensor data to perform offline tests of the filters. Compare the TSF and EKF.

5. Discuss and compare simulations and results from experimental work

6. A report on the simulation and experimental testing. Conclusions will be presented along with recommendations for further work.

The master thesis is written in English, and is structured as a research report. Following a preface, a summary is given in both English as well as Norwegian, according to the departmental guidelines for a master thesis from NTNU. In the introduction of the report the background and motivation for the thesis are explained further. A short review of previous research on the chosen topic is also given. The introduction will also list the main contributions made, as well as an outline of the rest of the thesis. The main part of the report contains a literature review, as specified above, a description of the integration filters and how these are tested, as well as a presentation of results from simulations and experimental work. Discussions and conclusions are made based on these, and finally suggestions for further work are given. Computer codes, pictures, data series and a PDF version of the report shall be included electronically with the submitted version.

Ingrid Schjølberg
Supervisor

Preface

This report is the result of a master thesis in Marine Technology with a specialization within Marine Cybernetics, from the Norwegian University of Science and Technology. The main motivation for this work has been to look further into accurate navigation for underwater applications, for use on ROVs. It is assumed that the reader has relevant competence when it comes to marine technology and cybernetics. This thesis is a continuation of a Project Thesis done autumn 2016, and the period of work spans from January to June 2017.

The work is done with support from supervisor Ingrid Schjølberg and co-supervisors Stian Skaalvik Sandøy and Brede Thorkildsen. I would like to thank Ingrid and Brede for their guidance and encouragement. A special thanks goes to Stian, whom always made himself available whenever I felt stuck, and made helpful suggestions along the way. Also, I would like to thank Ph.D candidate Bent O. Arnesen, for all his help with the Videoray Pro 4 ROV. I would also like to thank Ph.D candidates Bård B. Stovner and Eirik Henriksen for providing me with experimental data that I could use to generate relevant results.

Finally, my sincerest thanks goes to friends, family and close ones which have supported me throughout my years of study, reminding me that there is more to life than studying.

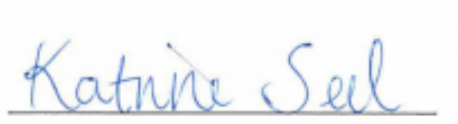

Katrine Seel

Trondheim, June 8, 2017

Summary

Underwater navigation is one of the key issues that need to be addressed in order to make operation of underwater vehicles more autonomous. This thesis investigates two different methods for integration of inertial and pseudo-range measurements that is to be suited for underwater navigation of a Remotely Operated Vehicle (ROV). For underwater applications acoustic range measurements can be provided by Long Baseline (LBL) systems. And if the wave speed for which the acoustic signals propagate with is unknown, the measurements will be corrupted by an uncertainty modeled as a slowly-varying bias. The measurements are then referred to as pseudo-range measurements. An Inertial Measurement Unit (IMU) that is mounted on the underwater vehicle can measure the vehicle's linear accelerations.

A Three-Stage filter (TSF) was implemented for integration of inertial and pseudo-range measurements. The filter estimates the position, linear velocities, and a wave speed bias parameter in addition to acceleration measurement biases. Because the filter uses tightly coupled integration, the raw measurements are used directly in the filter, and the estimation problem is nonlinear. The TSF is based on a novel approach of using an *exogenous state estimator* for providing an external estimate. This is used to linearize a second filter. And consequently it can be proven that the error dynamics have global exponential stability (GES). An Extended Kalman filter (EKF) was implemented for the same estimation problem, also using a tightly coupled integration.

A simulator was built in MATLAB, so the TSF and EKF could be verified and compared in simulations. Range and acceleration measurements were generated at realistic frequencies, 2 Hz and 100 Hz respectively. The measurements were added a realistic amount of noise, and in addition the acceleration measurements were corrupted by a constant bias. The filters were initialized with accurate initial estimates, and showed similar performance in steady-state, resulting in a similar Root-Mean-Square (RMS) position estimation error. Initializing the filters with inaccurate initial state estimates tested the transient behavior of the filters. And the plotted states suggested that the TSF converged

faster in transient behavior. Also the TSF converged with a smaller overshoot than the EKF estimates. This resulted in a smaller RMS position estimation error in transient behavior.

Physical experiments were conducted in the MC-laboratory at NTNU, where a test basin facilitates underwater experiments. An underwater positioning system, Qualisys Motion Tracking (QMT), was used to obtain the position of the ROV and was used as ground truth for the estimated position. Two different methods were used for generating range measurements, and two different ROVs were used to perform experiments. All sensor data was logged during both experiments, and used for offline tests of the integration filters. The data sets were used for testing steady-state and transient behavior of both filters. Overall the experimental results backed the same trends as seen in simulations, in favor of similar performance in steady-state and TSF having a faster transient behavior.

The EKF is currently the standard choice for integration of measurements for nonlinear estimation problems. The performance of the filters could vary beyond what has been found in this thesis, due to uncertainties related to the "true values" available during experiments, tuning of the filters or variations that come with different transponder set-ups. However, results from both simulations and two different experiments indicated good performance of the TSF when benchmarked against the EKF. To conclude, the TSF, based on the investigation done in this thesis, is recommended for the estimation problem considered. This inspires further work to continue examining the performance and the potential that the TSF could have for underwater navigation of ROVs.

Sammendrag

Undervannsnavigasjon vil være avgjørende for å kunne gjøre undervannsfartøy mer autonome. Denne oppgaven undersøker to ulike metoder for integrasjon av treghets- og pseudo-rangemålinger som kan egne seg for undervannsnavigasjon av en fjernstyrt undervannsrobot (ROV, eng: Remotely Operated Vehicle). For undervannsapplikasjoner vil akustiske rangemålinger typisk bli levert av Long Baseline (LBL) systemer. Og dersom bølgehastigheten som de akustiske signalene propagerer med er ukjent, vil målingene være påvirket av en unøyaktighet som modelleres som en saktevarierende feil. Målingene vil da omtales som pseudo-rangemålinger. Treghetsmålinger blir levert av en treghetsmåleenhet (IMU, eng: Inertial Measurement Unit), som er festet direkte på undervannsfartøyet og som blant annet kan måle fartøyets lineære akselerasjoner.

Et trestegsfilter (TSF, eng: Three-Stage Filter) ble implementert for integrasjon av treghets- og pseudo-rangemålinger. Filtrene estimerer posisjon, lineære hastigheter, feilen i lydbølgehastighet i tillegg til en konstant feil i akselerasjonsmålingene. Fordi filteret bruker en tett koblet integrasjon, og råmålingene blir brukt direkte i filteret, blir dette estimeringsproblemet ulineært. Trestegsfilteret bruker en ny tilnærming der en *ekstern estimator* brukes for å levere et eksternt tilstandsestimat. Dette brukes til å linearisere et annet filter. Og for denne strukturen kan man vise at feildynamikken er globalt eksponentielt stabil (GES). Et Extended Kalman Filter (EKF) ble implementert for det samme estimeringsproblemet og bruker også en tett koblet integrasjon.

En simulator ble laget i MATLAB, slik at TSF og EKF kunne verifiseres og sammenliknes i simuleringer. Range- og treghetsmålinger ble generert ved realistiske frekvenser, henholdsvis 2 Hz og 100 Hz. Det ble lagt til støy i målingene, i tillegg til at akselerasjonsmålingene også ble lagt til konstante feil. Ved nøyaktig initialisering, viste filtrene svært lik stasjonær oppførsel, som resulterte i en lik gjennomsnittsverdi (RMS, eng: Root-Mean-Square) for estimeringsfeilen i posisjon. Transient oppførsel ble testet ved å initialisere filtrene med unøyaktige startestimater. Plot av tilstandsestimatene viste at TSF konvergerte raskere i transient oppførsel. TSF hadde også mindre oversvingeamplitude, som

til sammen ga en mindre gjennomsnittsverdi for estimeringsfeilen i posisjon i transient oppførsel.

Fysiske forsøk ble utført i MC-laboratoriet på NTNU, der et testbasseng legger til rette for undervannsforsøk. Et undervannsposisjoneringssystem, Qualisys Motion Tracking (QMT), ble brukt til å bestemme posisjonen til ROVen under forsøk, og ble i tillegg brukt som fasit for den estimerte posisjonen. Rangemålinger ble generert på to ulike måter, og i tillegg ble to ulike ROVer brukt til å utføre to ulike forsøk. All sensor-data ble logget underveis, og brukt i offline-tester av filtrene, både i stasjonær og transient tilstand. Kort oppsummert viste de eksperimentelle resultatene de samme trendene som ble observert under simuleringer. Igjen så man at TSF konvergerte raskere i transient tilstand, og oppførte seg svært likt i stasjonær tilstand.

Per i dag blir EKF typisk valgt som filter for integrasjon av målinger i ulineære estimeringsproblemer. Ytelsen på filtrene vil kunne variere ut fra det som har blitt funnet i denne oppgaven, på grunn av usikkerhet knyttet til de "sanne verdiene" brukt under forsøkene, tuning av filtrene i tillegg til variasjoner som kan komme av ulike transponderoppsett. Til tross for dette, viste resultater både fra simuleringer og to ulike eksperimenter at TSF presterte bra sammenliknet med EKF. Basert på undersøkelsen gjort i denne oppgaven, blir TSF derfor anbefalt for estimeringsproblemet som det er tatt utgangspunkt i. Dette inspirerer til videre arbeid som fortsetter å undersøke ytelsen og potensialet TSF kan ha for undervannsnavigasjon av ROVer.

Contents

Preface i

1 Introduction **1**

1.1 Background and motivation 1

1.1.1 Subsea IMR operations 1

1.1.2 ROV operations in fisheries and aquaculture 2

1.1.3 Autonomy in ROV operations 3

1.2 Previous Research 4

1.3 Objective 5

1.4 Contributions 5

1.5 Structure of the report 6

2 Underwater navigation **7**

2.1 An overview 7

2.2 Inertial Navigation System 9

2.2.1 Inertial measurement Unit 10

2.2.2 IMU error characteristics 10

2.3 Acoustic navigation 11

2.3.1 Acoustic positioning 11

2.3.2 Range-based navigation 13

2.3.3 Shortcomings of acoustic navigation 14

2.4 Geophysical navigation 14

2.5 Observer design and state estimation 15

2.5.1 Models vs. measurements 16

2.5.2 Sensor-based observers 16

2.5.3 Stability properties 18

2.6 Integration filters 18

2.6.1 Integration of inertial navigation and range measurements 18

2.6.2 Loosely and tightly coupled scheme 19

2.6.3 Extended Kalman Filter . . . 20
2.6.4 The eXogenous Kalman Filter . . . 20
2.6.5 Three-Stage filter . . . 21

3 Modeling **23**
3.1 Mathematical ROV model . . . 23
3.2 Kinematics . . . 24
3.2.1 Notation . . . 24
3.2.2 Reference frames . . . 24
3.2.3 Generalized coordinates . . . 26
3.2.4 Transformations . . . 27
3.3 Measurement models . . . 29
3.3.1 Gaussian white noise . . . 30
3.3.2 Random walk process . . . 30
3.3.3 Range measurements . . . 31
3.3.4 Acceleration measurements . . . 32

4 Integration filter design **35**
4.1 Observer model . . . 35
4.2 Discretization . . . 37
4.3 Discrete Kalman Filter Design . . . 37
4.4 Three-Stage filter . . . 38
4.4.1 Nonlinear algebraic transformation . . . 39
4.4.2 LTV Kalman filter . . . 42
4.4.3 Linearized Kalman filter . . . 43
4.5 Extended Kalman Filter . . . 44
4.6 Observability . . . 44
4.6.1 Uniform observability . . . 45
4.6.2 Uniform controllability . . . 46
4.6.3 Observability for LTV Kalman filter . . . 46
4.6.4 Observability for linearized Kalman filter . . . 47
4.6.5 Stability for TSF and EKF . . . 48
4.6.6 Condition number and degree of observability . . . 48

5 Implementation of navigation system **51**
5.1 Simulator . . . 51
5.1.1 Simulation I . . . 53
5.1.2 Simulation II . . . 53

5.1.3 Execution time . . . 54
5.2 Physical experiments . . . 54
5.2.1 Experiment I . . . 54
5.2.2 Experiment II . . . 55
5.2.3 The Videoray Pro 4 ROV . . . 55
5.2.4 SeaBotix LBV600-6 ROV . . . 56
5.2.5 Qualisys Motion Tracking system . . . 57
5.2.6 Water Linked acoustic system . . . 59
5.2.7 Determining measurement noise . . . 60
5.2.8 Determining process noise . . . 62
5.2.9 Calibration of acceleration measurements . . . 63
5.2.10 Handling sensor drop-outs . . . 63

6 Simulation results **65**
6.1 Summary of simulation specifications . . . 65
6.2 Simulation I: Steady-state behavior . . . 66
6.2.1 Analyzing the steps of the TSF . . . 68
6.2.2 Resolving the ambiguity between r_1 and r_2 . . . 69
6.3 Simulation II: Transient behavior . . . 70
6.4 RMS in simulations . . . 72
6.5 Execution time . . . 72
6.6 Discussion of simulation results . . . 73
6.6.1 Range navigation solution accuracy . . . 73
6.6.2 Analyzing the steps of the TSF . . . 73
6.6.3 Resolving the ambiguity between r_1 and r_2 . . . 74
6.6.4 Execution time . . . 75

7 Experimental results **77**
7.1 Summary of experiment specifications . . . 77
7.2 Experiment I: Results using Videoray . . . 79
7.2.1 Steady-state behavior . . . 79
7.2.2 Transient behavior . . . 81
7.2.3 Discussion of results obtained using Videoray . . . 83
7.3 Experiment II: Results using Seabotix . . . 85
7.3.1 Steady-state behavior . . . 85
7.3.2 Transient behavior . . . 88
7.3.3 Discussion of results obtained using Seabotix . . . 90
7.4 RMS in experiments . . . 92

8 Discussion of results **93**
8.1 Comparing simulation and experimental results 93
8.1.1 Steady-state behavior 94
8.1.2 Transient behavior 95
8.2 Dead-reckoning performance 95
8.2.1 Acceleration bias estimation 96

9 Conclusion **97**

10 Further work **99**

Bibliography **100**

A IMU accelerometer calibration **105**

B Attachments **107**
B.1 Poster 107
B.2 Simulator 107
B.3 Experiments 107
B.3.1 Experiment I 108
B.3.2 Experiment II 108

List of Figures

1.1 ROV performing IMR operation, courtesy of TechnipFMC 2
1.2 Guidance, navigation and control, courtesy of Fossen (2011) 4

2.1 Underwater navigation classifications, courtesy of Paull et al. (2014) . . . 8
2.2 Underwater acoustic positioning methods, courtesy of Kongsberg Maritime 12
2.3 Strapdown INS combining attitude estimation with integration filter, courtesy of Dukan (2014) 17
2.4 eXogenous Kalman filter (XKF), courtesy of Johansen and Fossen (2016a) 21
2.5 Three-stage filter (TSF), courtesy of A. Johansen et al. (2016) 22

3.1 ROV BODY frame and NED frame in towing tank 26
3.2 The strapdown INS equations, courtesy of Fossen (2012) 32

4.1 Structure of TSF 39
4.2 Structure of EKF 44

5.1 Structure of MATLAB simulator 52
5.2 Videoray Pro 4, courtesy of AtlantasMarine 56
5.3 SeaBotix LBV600-6, courtesy of BlueSolutions 56
5.4 Videoray marker configuration 58
5.5 SeaBotix marker configuration 59
5.6 Nonlinear transformation of a Gaussian variable, courtesy of Thrun et al. (2005) 61

6.1 Simulation I: Trajectory in 3D 66
6.2 Simulation I: Position estimation error 66
6.3 Simulation I: Velocity estimation error 67
6.4 Simulation I: Wave speed estimate 67
6.5 Simulation I: Acceleration bias estimates 68
6.6 Simulation I: Steady-state behavior of second and third stage of the TSF 68
6.7 Simulation I: Solution to algebraic transformation 69

6.8 Simulation I: Estimated and true position and wave speed bias 69
6.9 Simulation II: Trajectory in 3D 70
6.10 Simulation II: Position estimation error 70
6.11 Simulation II: Velocity estimation error 71
6.12 Simulation II: Wave speed estimate 71
6.13 Simulation II: Acceleration bias estimates 72

7.1 Experiment I: Trajectory in 2D 79
7.2 Experiment I: Position estimation error 79
7.3 Experiment I: Velocity estimation error 80
7.4 Experiment I: Wave speed estimate 80
7.5 Experiment I: Acceleration bias estimates 81
7.6 Experiment I: Trajectory in 2D 81
7.7 Experiment I: Position estimation error 82
7.8 Experiment I: Velocity estimation error 82
7.9 Experiment I: Wave speed estimate 83
7.10 Experiment I: Acceleration bias estimates 83
7.11 Experiment II: Trajectory in 2D 85
7.12 Experiment II: Position estimation error 85
7.13 Experiment II: Velocity estimation error 86
7.14 Experiment II: Wave speed estimate 86
7.15 Experiment II: Acceleration bias estimates 87
7.16 Experiment II: Trajectory in 2D 88
7.17 Experiment II: Position estimation error 88
7.18 Experiment II: Velocity estimation error 89
7.19 Experiment II: Wave speed estimate 89
7.20 Experiment II: Acceleration bias estimates 90
7.21 Experiment II: Attitude estimates 91

List of Tables

3.1 Notation used for marine vessels, courtesy of SNAME (1950) 24

5.1 Qualisys measurement noise variance, courtesy of Sandøy et al. (2016) . . 60
5.2 Range measurements noise variance 61
5.3 IMU accelerometer measurement noise variance 62

6.1 Sensor specifications used in simulations 65
6.2 Position RMS error in simulations 72
6.3 Average execution time per iteration 72

7.1 Experiment specifications 77
7.2 Sensor specifications during experiments 78
7.3 Position RMS error in experiments 92

Nomenclature

Abbreviations

ROV Remotely Operated Vehicle

LBL Long Baseline

KF Kalman Filter

EKF Extended Kalman Filter

TSF Three-Stage Filter

XKF eXogenous Kalman Filter

IMR Inspection Maintenace and Repair

INS Inertial Navigation System

IMU Inertial Measurement Unit

TOA Time-of-Arrival

DOF Degrees of Freedom

NED North-East-Down

$GNSS$ Global Navigation Satellite System

LTV Linear Time-Variant

CO Center of Origin

RMS Root-Mean-Square

DOP Dilution of Precision

QMT Qualisys Motion Tracking

$SLAM$ Simultaneous Localization and Mapping

$MC-lab$ Marine Cybernetics Laboratory

GES Global Exponential Stability

Chapter 1

Introduction

1.1 Background and motivation

A Remotely Operated Vehicle (ROV) is a tethered, unmanned vehicle that will be operated at a distance from where it is located. ROVs are normally tethered by an umbilical that supplies electrical power as well as fiber optics, providing communication with an operator and transfer of data. This allows an operator to control the ROV from a surface vessel, limiting the range of the ROV to the length of the tether. An ROV can be equipped with a selection of sensors that can collect useful data, which today is used in the oil- and gas industry, in scientific research communities, in subsea mining, by the military and is also emerging in fisheries and aquaculture.

1.1.1 Subsea IMR operations

Subsea oil and gas production refers to facilities where equipment is placed on the seabed. The main motivation for moving oil and gas production subsea is primarily to cut the costs of building and installing production platforms on the sea surface. Subsea technology is especially favorable when oil and gas fields are placed on deep waters. Subsea processing systems are becoming more comprehensive, which will enhance field economics by maximizing oil and gas recovery, increasing production and reducing costs. This will also contribute to extending field lifetime.

As production equipment is moved subsea and into deeper waters, the subsea oil and gas industry has come to rely on ROVs for a number of operations. These are with a common term referred to as inspection, repair and maintenance (IMR) operations, and range from

drilling support, subsea construction to asset and pipeline inspection, subsea site surveys, protection surveys, other repair operations in addition to much more. In Figure 1.1 an ROV is doing subsea intervention work. Today ROVs used for subsea intervention come with manipulators and other tools designed to work on subsea equipment.

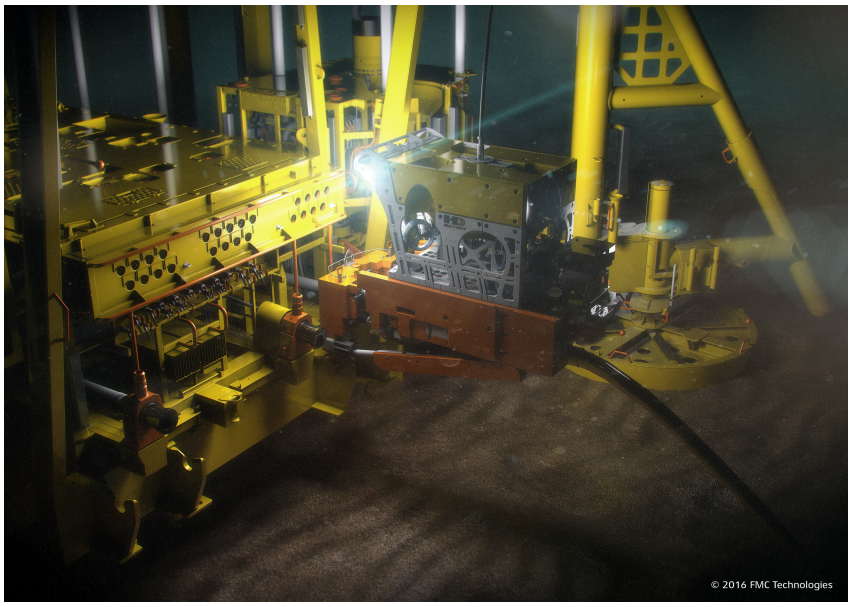

Figure 1.1: ROV performing IMR operation, courtesy of TechnipFMC

Performing ROV operations in proximity of subsea installations means that the ROV must be maneuvered with extreme accuracy. Not only because the subsea units and structures are expensive, but also because a collision is potentially catastrophic in case of leakage to the surroundings. This means that accurate underwater navigation will be especially important during the IMR part of the mission, in addition to any part of the mission when the ROV will be operating close to subsea installations.

Oil and gas related activity is expected to move further offshore in the future, and when it does ROVs will become an even more important tool for performing IMR operations on deep waters. The use of ROVs is in many ways an enabler for exploring more harsh and remote operation sites.

1.1.2 ROV operations in fisheries and aquaculture

Fish farming is becoming an increasingly large supplier of the world's seafood. And the use of ROVs for production support at the fish farms is a growing industry. Introducing ROVs in aquaculture means that inspection of fish cages can be done more systematically and without human divers. Typically smaller, more low-cost ROVs can be used for

checking nets for holes, assuring integrity of moorings and other underwater infrastructure and for monitoring fish behavior.

The development of smaller and cheaper ROVs has been essential for the growing use of underwater vehicles in this industry. Improving underwater navigation, exploiting relatively cheap navigation sensors and making the operation less dependent on skilled operators, will enable an ongoing use of ROVs also in small fish businesses.

1.1.3 Autonomy in ROV operations

Currently, the majority of all ROV IMR operations are manually controlled, using only a few or no automatic control functions (Schjølberg et al., 2016). Consequently the efficiency in operation is highly dependent on the experience of the ROV operator (Schjølberg and Utne, 2015). The operation is because of this also dependent on the support from offshore vessels during the entire duration of the operation. The day rates for these vessels are excessive, and in total the costs related to these operations constitute a huge expense for the industry. Making motion control of ROVs more autonomous will contribute to reduced workload on the operators, minimize human errors and increase efficiency in operations. Here autonomy refers to a robot's ability to use available information in order to make independent decisions on how to perform a mission. Autonomy can be regarded as one of the solutions that will help optimize subsea IMR operations in the oil and gas industry (Schjølberg and Utne, 2015). More autonomous ROV functions will also increase their value and potential in other industries.

Today functions such as station keeping, velocity control, path tracking and terrain following are being developed. This allows an operator to interact less with vehicle control, and allows them to keep closer track of data that is collected by cameras and sensors. These types of developments are important contributions towards more autonomy in ROV operations. A challenge is to make these functions reliable enough, so they can be implemented in subsea IMR operations. Figure 1.2 shows how the tasks of a motion control system are related to the navigation system. Here it appears that the motion control system is indeed dependent on estimates of position, velocity and attitude from the navigation system. In order to leave the human out of the control loop, the control system will need accurate states to react upon. Making navigation more autonomous will therefore impose strict requirements to accurate feedback, and will be a prerequisite for being able to perform closed-loop control (Dukan, 2014).

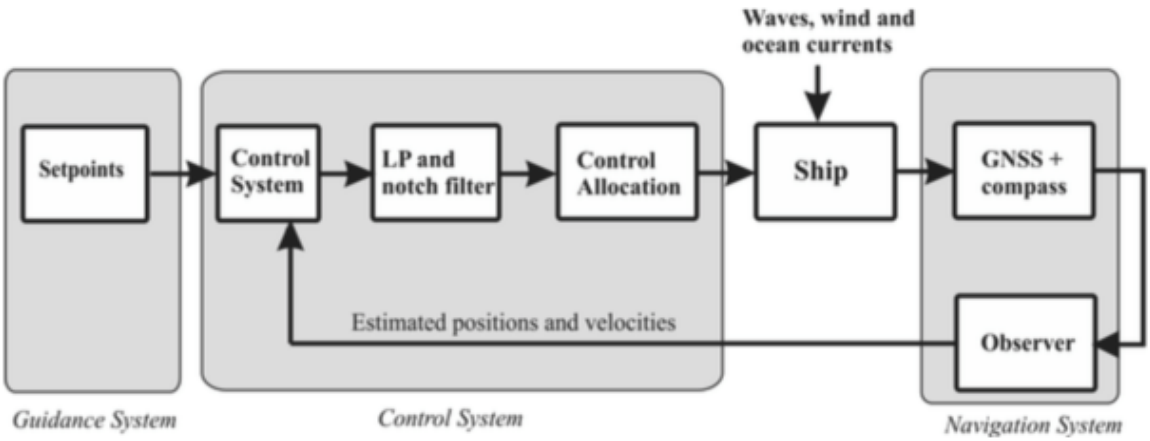

Figure 1.2: Guidance, navigation and control, courtesy of Fossen (2011)

1.2 Previous Research

Recent advances in underwater navigation are based on merging information from acoustic positioning techniques with other inertial sensors. Classical filtering strategies often resort to the well-known Extended Kalman Filter (EKF). In Morgado et al. (2013) the EKF was implemented with a tightly coupled strategy, and compared to the more classical loosely coupled integration. For the tightly coupled scheme different variations of the nonlinear Kalman Filters (KF), which in addition to the EKF also include the unscented KF (UKF) and particle filters (PF), have also been widely used.

The tightly coupled schemes also include methods where "new measurements" are constructed from the pseudo-range measurements, which give a linear relationship between the constructed measurements and the estimated states. A nonlinear algebraic transformation has been used to derive a set of quasi-linear measurement equations, for example in the work by A. Johansen et al. (2016) and A. Johansen (2015).

Position and velocity estimation based on integration of inertial navigation and Long Baseline (LBL) range measurements has also been studied in Batista et al. (2010). Here a cascaded navigation system was used, which opposed to the EKF, was proven to have globally exponentially stable (GES) error dynamics. In A. Johansen et al. (2016) the same cascaded approach was used to combine two filters, in addition to making use of the nonlinear algebraic transformation of the pseudo-range measurements. This resulted in a Three-Stage Filter (TSF) for position and linear velocity estimation using inertial and pseudo-range measurements. In B. Stovner et al. (2016) the TSF from A. Johansen et al.

(2016) is employed for estimating position and linear velocity, and uses a multiplicative bias parameter to model the unknown wave speed. A formulation relating the pseudo-range to position and wave speed bias parameter was developed in Batista (2015), and in B. Stovner et al. (2016) this formulation is adjusted so that the states could be linearly related to the measurements.

1.3 Objective

The main objective of this thesis is to investigate two different filters for integration of inertial and pseudo-range measurements that would be suited for underwater navigation of an ROV. The focus of this investigation lies on the accuracy of the state estimates, convergence in case of accurate and inaccurate initialization in addition to stability properties. The filters are tested in simulations in order to verify their implementation and compare their performance. Finally, the integration filters are also tested offline using experimental data, in order to test their robustness in more realistic conditions for underwater navigation.

1.4 Contributions

The main contributions made in this thesis, are listed below.

1. The TSF as described in B. Stovner et al. (2016) was implemented, adding the additional states of acceleration biases
2. An EKF was implemented for the same estimation problem
3. A simulator was developed in MATLAB for testing sensor-based observers
4. The filters were verified and compared in simulations
5. Modification of the integration filters were done so they could be tested offline, using logged experimental data
6. The performance of the filters was compared in offline runs

1.5 Structure of the report

The rest of the thesis is structured as follows:

Chapter 2 is dedicated to a literature review. This includes an overview of underwater navigation techniques, with a main focus on integration of inertial and pseudo-range measurements.

Chapter 3 presents the mathematical modeling and reference frames that are used in order to describe the motion of the simulated ROV as well as the measurements that are generated.

Chapter 4 renders the observer design of the TSF and the EKF.

Chapter 5 describes the implementation of the simulator and also the experiments that were conducted in the MC-laboratory which were the source of the experimental data that the filters were tested for. The chapter includes a description of the ROVs, sensors and other equipment that were used.

Chapter 6 presents results from simulations. The simulation results are briefly discussed.

Chapter 7 presents results from offline tests using experimental data. The experimental results are briefly discussed.

Chapter 8 discusses the results obtained both from simulations as well as from physical experiments. A comparison between simulation and experimental results is given.

Chapter 9 draws conclusions from the results and discussions.

Chapter 10 proposes further work.

Chapter 2

Underwater navigation

This chapter is dedicated to review some of the literature and recent research in the field of underwater navigation. In this thesis *navigation* is the process of directing a craft by determining its position. *Positioning* is the process of establishing the position of a vehicle, and is a subset of navigation. This should not be confused with the term *localization* which is placing a moving object within a map (Paull et al., 2014).

In a marine control system, the navigation system includes sensor devices measuring the system's states. This may be position, velocity or the distance travelled. In circumstances where relevant states might be too expensive to measure or there simply exists no sensor that measures this state, an observer can be used for state estimation. An observer can be a high or low fidelity model of the system that is used to estimate the model's state (Sørensen, 2013). The observer can establish for example the vehicle's position within a specific reference frame among other system states, based on the sensor measurements that are available.

The topics highlighted in this literature review are state of the art underwater navigation techniques, with a closer look on inertial navigation aided by range measurements and filter design for this particular case.

2.1 An overview

For aerial and ground vehicles, the Global Navigation Satellite System (GNSS) is widely used for navigation solutions. A major challenge for underwater navigation is that there exists no global positioning system. Due to the strong attenuation of electromagnetic

waves under water, underwater applications cannot rely on GNSS. Underwater navigation must therefore rely on other techniques, which can be divided into three main categories according to Paull et al. (2014):

- Inertial navigation/dead reckoning
- Acoustic transponders/modems
- Geophysical navigation

Figure 2.1 gives an overview of underwater navigation methods available today. The figure is intended for AUV navigation, but the same methods apply for other underwater vehicles. The overview includes the same three techniques as mentioned above, listing also the most commonly used sensor technologies applied by each of them.

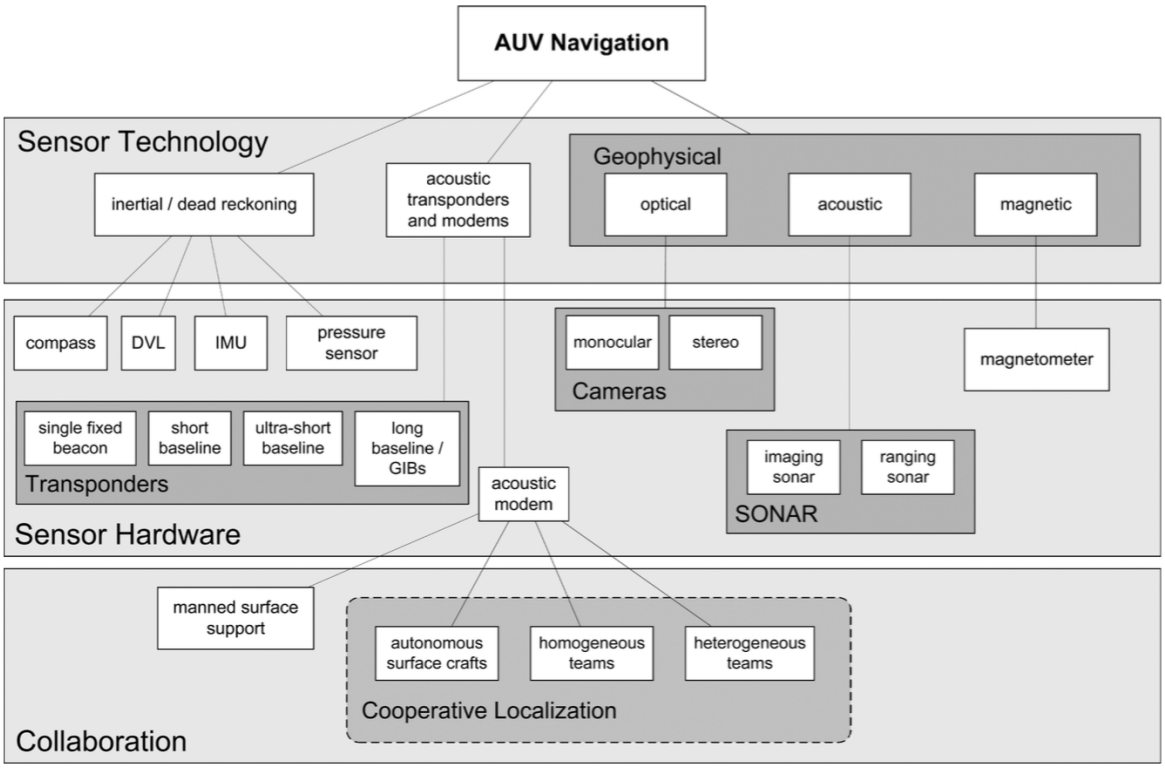

Figure 2.1: Underwater navigation classifications, courtesy of Paull et al. (2014)

Inertial navigation is based on measurements from a variety of navigation sensors in order to propagate the current state of an underwater vehicle. This is also known as dead reckoning. **Acoustic navigation** is based on propagation of sound waves under water. **Geophysical navigation** refers to methods that use external environmental features to determine a vehicle's position (Paull et al., 2014), and relies on scientific sensors to a greater extent than navigation sensors (C. Kinsey et al., 2006).

The type of navigation technique used is highly dependent on what type of operation is being done, the associated requirements to navigation accuracy as well as infrastructure and available sensor data. A common practice is to combine systems to enhance performance. An *integrated navigation system* determines the states of a system using more than one technology (Groves, 2008). In Section 2.6.1 integration of inertial and range measurements is elaborated further. And in Section 2.6 several filters for this application are discussed.

2.2 Inertial Navigation System

An INS will typically calculate position, velocity and attitude using high frequency data, from an Inertial Measurement Unit (IMU). Today, the sensors contained in the IMU are simply strapped to the vehicle, which is known as a strapdown INS. Because navigation is based on dead reckoning, this requires that the initial states are known. The system will then calculate future states by integrating the information provided by the inertial sensors. The kinematic equations formulated for the strapdown case, are integrated numerically based on the IMU measurements, and constitute the INS.

Inertial navigation is known to give accurate short-term results, but its performance quickly degrades with time, because of integration of sensor noise as well as sensor biases. Due to these inherent errors in the IMU, all dead-reckoning methods based on these measurements will suffer from cumulative errors. In order to correct this drift-off, and stabilize the estimation errors, INS can be combined with other aiding sensors and different navigation techniques to correct this.

In addition to the navigation sensors contained in the IMU, the INS algorithm can also include sensor data from a compass, a Doppler Velocity Log (DVL) or a pressure sensor, as illustrated in Figure 2.1. A compass is able to sense the heading of a vehicle in motion, by measuring the direction of the horizontal components of Earth's magnetic field. This can therefore partially correct the drift-off in the orientation estimate. A pressure sensor provides the depth of a vehicle, by assuming that the atmospheric pressure at the surface is known and using that static pressure is proportional to depth. This can correct the position estimate in Down. The DVL can measure the 3-DOF linear velocities of a moving body. This is done by emitting acoustic pulses, that are reflected for example by the seabed, and measuring the Doppler shift in the returned signals to determine the velocity.

2.2.1 Inertial measurement Unit

An IMU typically consists of three accelerometers and three gyroscopes mounted with orthogonal axes, that measure the 3-Degrees-of-Freedom (DOF) accelerations and turn rates respectively (Dukan, 2014). The IMU can also include magnetometers that measure the magnetic field components in 3-DOF. The acceleration measurements can be integrated once to obtain velocity, twice to obtain position, while the turn rates can be used for determining an estimate of the attitude of the vehicle. These are known as the INS strapdown equations, and are illustrated in Figure 3.2. In Chapter 3 the relevant measurement equations are described further.

The IMU measurement models are only valid for low-speed applications, such as for ships and underwater vehicles, because it is assumed that the inertial frame in which the measurements are obtained in is non-rotating. Read more about the relevant reference frame in a navigation context, in Chapter 3.

In recent years there has been a breakthrough in the development of low-cost inertial sensors based on micro-electromechanical system (MEMS) technology. This has resulted in the use of MEMS-based inertial sensors in a wide range of products, among these underwater navigation applications. Consequently more research has been targeted on developing integration navigation algorithms that can be implemented at low cost, combining MEMS-based inertial sensors with other navigation techniques.

2.2.2 IMU error characteristics

Inaccurate scaling, sensor axis misalignments, and cross-axis sensitivities in addition to non-zero biases will usually affect low-cost MEMS-based IMUs. IMU calibration is the process of identifying these quantities, and compensating for the error identified in the measurements.

Scale factor error is an erroneous relation between input and output, used to convert digital outputs of the sensors to real physical quantity. For accelerometers in the IMU, sensor misalignment describes the angular difference between the accelerometer's axis of rotation and the system defined inertial reference frame.

Each systematic error source has four components: a fixed contribution, a temperature-dependent variation, a run-to-run variation, and an in-run variation (Groves, 2008). The fixed contribution and the temperature-dependent variation can be corrected using calibration algorithms. The run-to-run variation results in error sources that are different

each time the sensor is run, but will remain constant within the same run. These can be calibrated using the integration algorithm. The in-run variation gives a slowly-varying error source, and is in practice hard to observe and therefore hard to compensate for (Groves, 2008).

2.3 Acoustic navigation

Acoustic navigation techniques are based on measuring ranges using acoustic signals. The range is not measured directly, but instead a parameter that is proportional to the geometric range is measured, namely the *time-of-arrival* (TOA). Acoustics are applied in a number of different navigation methods used under water, which all have in common that they are based on TOA measurements. A main distinction is made between techniques that use acoustic beacons, usually fixed on either a surface vessel or on the seabed, and acoustic modems, that can be mounted on an underwater vehicle and are therefore usually non-stationary. An acoustic modem allows both simultaneous communication of small data packets as well as ranging based on TOA measurements (Paull et al., 2014). This has enabled so-called cooperative navigation, where multiple underwater vehicles can share navigation data.

2.3.1 Acoustic positioning

Acoustic positioning employs fixed subsea beacons or transponders to generate range measurements. In Figure 2.2 the three main methods for underwater acoustic positioning are illustrated. For underwater applications ultra-short baseline (USBL) and LBL navigation are most commonly used (Ludvigsen, 2010). The two methods are explained further in the following sections.

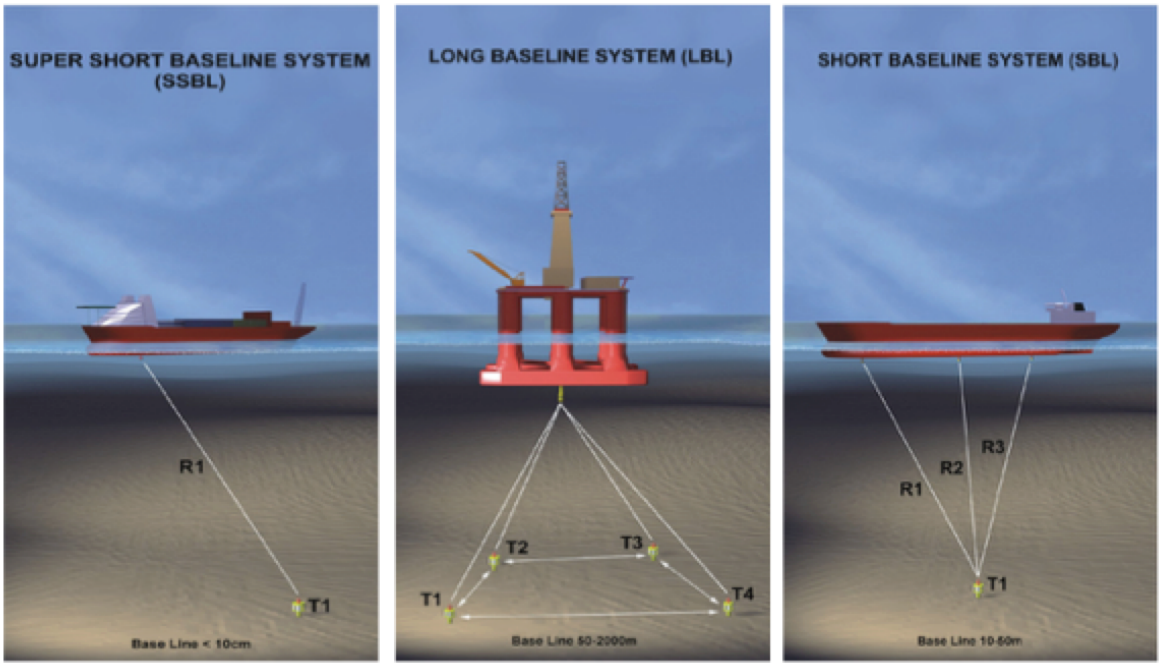

Figure 2.2: Underwater acoustic positioning methods, courtesy of Kongsberg Maritime

Acoustic positioning with fixed subsea beacons applies mainly two devices, namely an interrogator and a transponder, which both are combined transmitter-receiver devices (Christ and Wernli, 2013). The interrogator will transmit a short acoustic signal, and when registered by the transponder, a output signal with a new frequency is sent in reply. So the transponder will send out a signal on receipt of the interrogation signal from the interrogator, but with a different frequency (Christ and Wernli, 2013). By measuring the time from the transmission of one signal to a new signal is registered in return, the TOA measurement is obtained. Using that the sound propagation velocity is known, range measurements, that is the distance between the interrogator and the transponder, can be calculated based on TOA measurements.

Ultra-short baseline navigation

USBL navigation allows an underwater vehicle to position itself relative to a surface ship. The interrogators will typically be mounted on the ship, while transponders are placed on the underwater vehicle, for example an ROV, in motion. This method is also known as super short baseline, where "baseline" refers to the distance between the transducers, the device making acoustic signals, on the interrogator. The angle between the transponder mounted on the ROV and the interrogator on the ship, also known as the bearing, is found from phase-differencing of the signal arriving at the interrogator. For the USBL

system the bearing and the TOA measurements are used to determine the position based on *triangulation principles* (Groves, 2008).

Long Baseline navigation

A LBL system consists of a number of acoustic transponder beacons at fixed locations on the seabed or potentially on ships or platforms, in addition to interrogators mounted on a moving underwater vehicle. The vehicle will be able to position itself relative to the transponder network. Here the term "baseline" refers to the distance between the fixed beacons (Christ and Wernli, 2013). LBL navigation uses range measurements only. And these are used in order to determine the position based on *trilateration* principles (Groves, 2008). In principle, navigation can be performed using only two transponders. However, with only two range measurements, a *baseline ambiguity* arises (Christ and Wernli, 2013). This means that it is not possible to determine which side of the baseline the object is located on, and the depth of the object is unknown. A third transponder is therefore used to obtain the exact point, to ensure unambiguous navigation, while four transponders typically will be used in order to give redundancy and to serve as a quality check of the range measurements.

Today, long baseline navigation is the most accurate method for obtaining position in X and Y. The price to pay is that a LBL network will require more expensive equipment, and a more extensive and time-consuming installation and calibration phase (Hegrenas et al., 2009). Also, a LBL network provides navigation within a limited maximum range, typically up to 5-10 km from the fixed beacon network (Webster et al., 2012).

2.3.2 Range-based navigation

Range-based positioning is a common term for positioning based on range measurements and trilateration principles. Examples of range-based positioning methods are GNSS as well as LBL systems that are based on the same principles. The TOA measurements that these systems provide will normally be corrupted by slowly-varying uncertainties. For GNSS applications this is typically because of clock-synchronization errors when measuring time, while for subsea applications uncertainties typically occur because of unknown wave speed of sound in water. Because of this the measurements will be biased. To account for this the range measurements are modeled with an slowly-varying bias parameter, and are referred to as *pseudo-range measurements*. Consequently, four variables typically need to be estimated based on the pseudo-range measurements: three

position coordinates and a bias parameter. This requires a minimum of four pseudo-range measurements. Range-based positioning systems can also be used to generate so-called *difference-in-time-of-arrival* (DTOA) of a signal sent from a known position. These are known as range-rate measurements, and if these are corrupted by the same bias parameter, they will be known as pseudo-range-rate measurements.

2.3.3 Shortcomings of acoustic navigation

Common for the acoustic positioning techniques, is that they suffer from a number of shortcomings. Listed below are those indicated by Paull et al. (2014).

- Small bandwidth
- Low data rate
- High latency
- Variable sound speed
- Multipath transmissions
- Unreliability

The TOA measurements that acoustic positioning relies on, are limited by the speed of sound in water, which is approximately 1500 m/s (C. Kinsey et al., 2006). This limits how fast the acoustic system is able to provide new measurements and contributes to latencies. Also, the fact that the speed of sound fluctuates, due to changes in water temperature, pressure or salinity, is further complicated by the fact that actual speed of sound also is difficult to measure accurately (Kussat et al., 2005). Variety of speed of sound across the water column, creates layers with variable sound speed, which also can result in multipath transmissions. And put together all of the above-mentioned drawbacks contribute to a level of uncertainty.

2.4 Geophysical navigation

Geophysical or terrain-based navigation methods use external environmental features as references for navigation. In recent years extensive research has been done on developing environmentally-based navigation methods, that omits the need for additional infrastruc-

ture. This form of navigation is truly autonomous, because the vehicle is independent of external measurements and infrastructure.

Geophysical navigation uses sensors and processing that enables detecting, identification and classification of specific environmental features. This can for example be done using real-time sensing and a terrain or landmark map using either topographic, magnetic, gravitational or geodetic data (C. Kinsey et al., 2006). The majority of geophysical navigation methods will use some form of simultaneous localization and mapping (SLAM). SLAM is the process where a robot builds a map of its environment while at the same time, it localizes itself within this map (Paull et al., 2014). Terrain-aided navigation (TAN) is becoming more common for underwater applications, and has demonstrated a great potential for the development of a new generation of navigation systems. Currently TAN navigation will typically use TOA sonars as the principal navigation sensors, in order to detect and identify features in the environment that can be used as navigation landmarks. An example of a geophysical navigation is work done by Teixeira and Pascoal (2008). In this article the navigation algorithm uses TAN complemented with geophysical data. Bathymetric and geomagnetic measurements were obtained using acoustic and magnetic sensor technology, and merged with dead-reckoning data, in order to estimate the position and velocity of an AUV. Despite the flexibility that geophysical navigation gives, the navigation techniques will also suffer from the fact that the more "natural" and unstructured the environment is, the more challenging feature extraction and matching becomes (C. Kinsey et al., 2006).

2.5 Observer design and state estimation

An observer will be an essential part of most navigation systems. Its main functions are listed below (Candeloro et al., 2012).

- Estimation of unmeasured states based on available measurements
- Estimation of environmental disturbances
- The ability of dead reckoning in case of sensor-faults
- Filtering of the measured signal

2.5.1 Models vs. measurements

An observer can be based on either a model of the body in motion or on measurements. The typical strapdown INS system as described in Section 2.2, is an example of measurement-based navigation and relies on measurements only. In turn this means that the accuracy of the estimated states are highly dependent on the quality of the inertial measurement unit and the accuracy of the measurements they provide (Paull et al., 2014). However, if high accuracy sensors are used, measurement-based navigation can provide accurate estimates of position, velocity and attitude. Because all unknown forces acting on a moving body is felt instantaneously by accelerometers, these are included directly in the INS. Otherwise these can be hard to predict.

Model-based navigation solutions rely on a model of the underwater vehicle. These are efficient for filtering noise and estimating states without phase lag (Dukan, 2014). Even though it can be challenging to estimate the hydrodynamics of underwater vehicles, even a very simple model that captures the main dynamics can improve the navigation solution considerably. Despite this, unmodeled dynamics and disturbances can result in estimation errors.

2.5.2 Sensor-based observers

The strapdown INS problem can be divided into two main categories, where one of them is the attitude estimation and the other is the integration filter for estimation of translational states, which are position and linear velocity. The attitude estimator comprises all sensors that measure Euler angles or turn rates, which is used for estimating the orientation or attitude of the vehicle. Sensors that give information on the vehicle position, linear velocity or linear acceleration are considered part of the integration filter, and are used to estimate the translational motion of a vehicle (Paull et al., 2014). The attitude estimator and integration filter can be interconnected in order to enhance the accuracy of the total navigation solution. This is shown in Figure 2.3.

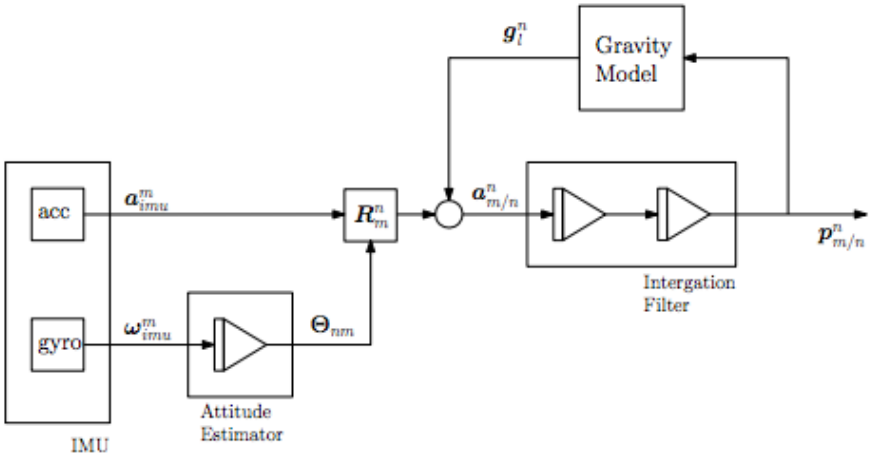

Figure 2.3: Strapdown INS combining attitude estimation with integration filter, courtesy of Dukan (2014)

Above it is seen how the attitude estimates can be integrated from turn rates, if the measurements provided are accurate enough. The acceleration measurements can be integrated twice to obtain position. The notation which is used in Figure 2.3 is explained further in Chapter 3. This configuration is convenient because the orientation of the vehicle is needed to obtain the acceleration measurements in the correct, inertial frame. These can then be integrated to obtain position and velocity estimates. However, this solution is heavily affected by the accuracy of attitude estimation. And small attitude errors can result in faulty resolved acceleration measurements, which will cause the velocity and position estimate to drift-off rapidly.

Position and velocity estimation using a combination of inertial and range measurements is a nonlinear estimation problem. Essentially two main categories exist for solving nonlinear estimation problems. These are divided into methods based on either local linearizations or nonlinear observers. For the linearized estimators a first-order Taylor series expansion is used to find an approximation of the nonlinear problem. The stochastic estimators have the advantage of optimal performance with respect to unknown measurement and process noise for the linear case, when tuned properly. The nonlinear observers lack the same systematic approach for optimizing their performance. However, they have strong stability properties, and are usually globally asymptotic stable (GAS) or at least have a large region of attraction. The mentioned stability properties are explained further in Section 2.5.3. Because the state is unknown, the linearized filters must normally rely on linearization about their own state estimate. And consequently global stability cannot be guaranteed. The linearization also causes errors and correlations that are sub-optimal (Johansen and Fossen, 2016b).

2.5.3 Stability properties

In order to analyze the stability of an observer, their error dynamics are studied. Crudely defined, stability of a dynamical system ensures that any solution that starts near an *equilibrium point* of the system, will stay near this for all time. If the solution also tends to the equilibrium point as time approaches infinity, the system is *asymptotically stable*. The equilibrium point of any dynamical system can be shifted to the origin. For convenience all definitions and theorems regarding stability is usually defined for the case when the equilibrium point is in the origin (Khalil, 2015).

For Linear-Time-Varying (LTV) systems, the term uniform stability becomes relevant. Uniform stability is a concept which guarantees that the stability is maintained, meaning that stability is obtained for all initial times, t_0. Further, there is a distinction between global and local stability. Global stability is obtained when the error dynamics converge to the origin for all possible initial conditions. If stability is only local, the solution must start within an area of the equilibrium point in order to ensure convergence. The set of initial values for which the error dynamics will converge to the origin is known as the *region of attraction* or *the region of asymptotic stability* (Khalil, 2015).

If the error dynamics of a LTV system converge to the origin independent of the initial solution and the initial time, t_0, the error dynamics are uniformly globally asymptotically stable (UGAS). The asymptotic form of stability does not quantify the rate of convergence. *Exponential stability* is a stronger form of stability, and implies uniform, asymptotic stability, and in addition demands an exponential rate of convergence. Whenever possible one wishes to prove uniformly globally exponential stability (UGES). For linear systems asymptotic and exponential stability are equivalent (Khalil, 2015).

2.6 Integration filters

Integration filters are used to combine different sensor data in order to estimate the desired states. In the following sections, integration filters for merging inertial and range measurements are considered.

2.6.1 Integration of inertial navigation and range measurements

One of the main attractions of combining sensor data is that measurements with opposite characteristics can be compensated by the strength of the other. INS suffers from

unbounded drift, but has low measurement noise. Acoustic measurements on the other hand have no drift, but high noise. As acoustic range measurements and INS suffer from opposite error characteristics, these are also good candidates for sensor fusion, in order to obtain state estimates with low levels of noise and smaller drift (Rowan, 2008).

Inertial sensors provide measurements with a much higher frequency than acoustic sensors that provide TOA signals. This means that in between range measurements, navigation must rely on vehicle position estimated based on available inertial sensor measurements. Even with low-frequency range measurements, the result of combining INS with range measurements is that the inertial solution will not drift and that the position estimation error is bounded (Webster et al., 2012).

The integration algorithm used for combining INS and range measurements will compare the inertial solution to the one found from the range measurements and estimate corrections to the system's states. This will typically be done using a Kalman Filter (KF). The final state estimate is then the corrected inertial navigation solution (Groves, 2008).

2.6.2 Loosely and tightly coupled scheme

A translational motion observer (TMO) designed for integration of range and inertial measurements, will typically estimate position, velocity and possibly a bias parameter. Two design philosophies exist for such state estimators. In the *loosely coupled scheme* an estimate of the position, velocity and bias is found from the pseudo-range measurements, meaning that direct measurements of the states are used in the integration algorithm. This yields a linear relationship between the measurements and the states. In a *tightly coupled scheme*, the pseudo-range measurements are used directly, so that the measurements are given by a nonlinear measurement model. State estimation using tightly coupled integration of pseudo-range and inertial measurements therefore typically uses a local linearization as the basis for a nonlinear Kalman filter or particle filter or uses a nonlinear observer.

The advantage of using a loosely coupled integration is a linear measurement model that simplifies the structure of the observer. However, the tightly coupled architecture will almost always perform better when it comes to accuracy as well as robustness (Groves, 2008).

2.6.3 Extended Kalman Filter

The EKF is regarded as a state of the art solution to the tightly coupled approach, and reaps the benefits of optimality in the presence of noise. Applied in its linear form, the LTV KF is known to be GES. However, when used in its nonlinear form, known as the EKF, global stability can no longer be guaranteed. The lack of global stability can essentially be traced back to the feedback loop, in which the filters own state estimate is used to make a local linearization of the nonlinear model of the system. In a scenario where the filter is initiated with a poor state estimate, the resulting linearization will be poor and produce a poor update, so that the filter might not be able to reduce the estimation error (Johansen and Fossen, 2016b). This means that the *global* stability of the system cannot be guaranteed, because convergence of the filter is dependent on an initialization that is sufficiently accurate. This means that the EKF obtains only *local* stability.

2.6.4 The eXogenous Kalman Filter

In order to overcome the weak stability property of the EKF, an *auxillary state estimator* has been studied by Johansen and Fossen (2016a) and Johansen and Fossen (2016b) among others. By using a different state estimator to provide an *exogenous* input to a linearized Kalman filter, the feedback loop that destabilizes the EKF is avoided. The nonlinear system is then linearized about the exogenous state estimate, rather than the KF's own state estimate. This is known as a two-stage estimator and is referred to as an *eXogenous Kalman filter* (XKF). The most important requirement to the auxiliary state estimator is that this should have strong stability properties, ideally GES. It follows from standard results on cascaded systems, that the cascade of estimators inherits the stability properties of the auxiliary state estimator.

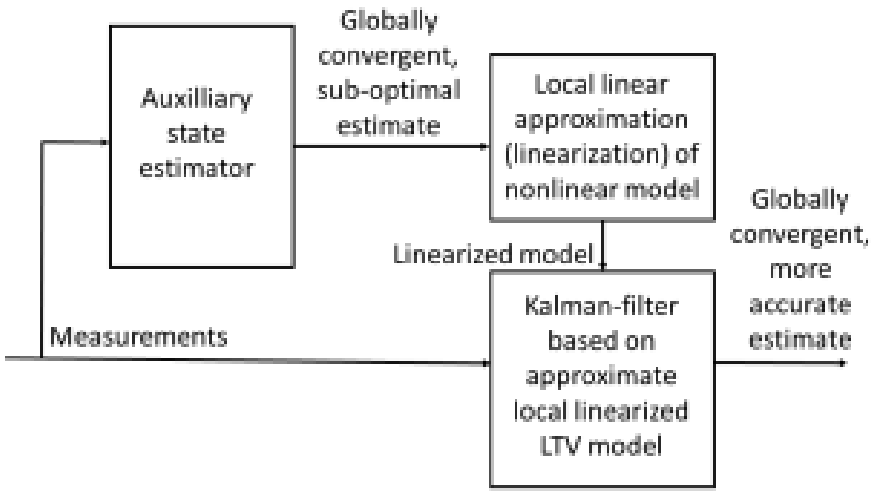

Figure 2.4: eXogenous Kalman filter (XKF), courtesy of Johansen and Fossen (2016a)

2.6.5 Three-Stage filter

The tightly coupled integration of inertial and pseudo-range measurements are considered specifically. And for this estimation problem a *globally valid nonlinear algebraic transformation* can be used on the nonlinear measurement equation in order to derive a set of quasi-linear time-varying equations. The term *quasi-linear* is used because the measurement model has been manipulated into a linear form, by introducing new variables. Because the algebraic transformation yields a quasi-linear time-varying (LTV) model, a UGES state estimator can be designed using the standard KF (Johansen and Fossen, 2016b). In the noise-free case, the quasi-linear measurement model is free of approximations. When noise is present however, the result of the algebraic transformation will give sub-optimal estimates. This is because the original nonlinear relationship is eliminated in order to obtain the global quasi-linear model, which will result in sub-optimal estimates when pseudo-range measurements are noisy.

To address the sub-optimality in presence of noise, the two-stage estimator approach has been proposed for this specific case. A second-stage KF is introduced in order to reduce the influence of noise on the estimates. The two-stage estimator aims to improve the accuracy of the estimates, by combining the quasi-linear time-varying measurement equations with the original nonlinear measurement model. The state estimate provided by the auxiliary estimator is used to ensure global convergence without considering optimality with respect to noise. The second stage estimator recovers estimation accuracy by considering both measurement and process noise (Johansen and Fossen, 2016b). This novel formulation has been referred to as the TSF, where the first stage constitutes the

algebraic transformation.

The TSF has earlier been presented in the work by A. Johansen et al. (2016), and later on also in work by B. Stovner et al. (2016) and Jørgensen et al. (2016). By using the principle of the XKF, the feedback loop used to linearize the nonlinear system is avoided, and global stability is restored. The TSF is able to give a globally convergent solution and accurate estimates, also when measurements are subject to noise.

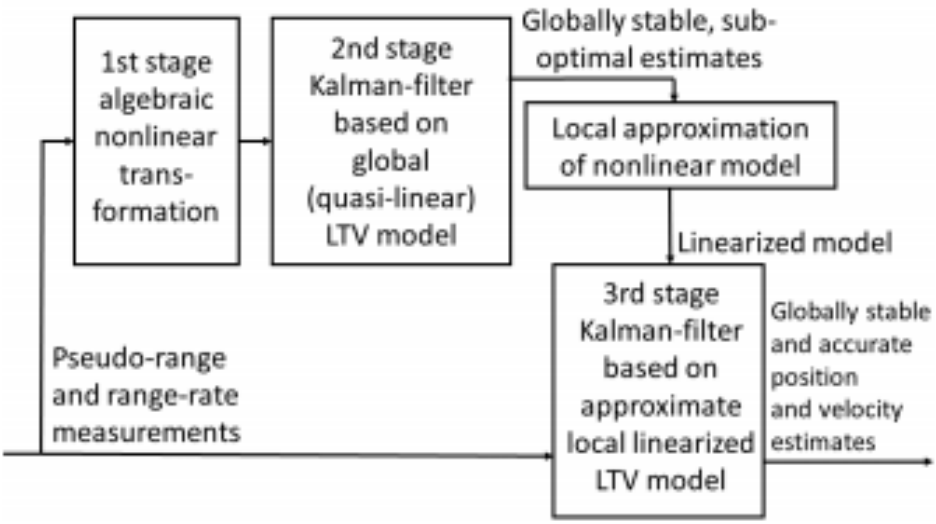

Figure 2.5: Three-stage filter (TSF), courtesy of A. Johansen et al. (2016)

In Figure 2.5 the main steps of the TSF are illustrated. In the first stage the global nonlinear transformation of the measurement equation takes place, which puts the measurement model on a quasi-linear form. The next stage is then to obtain a globally convergent estimate by using the quasi-linear measurement model and data from the 1st stage together with a model of the vehicle dynamics using a LTV KF that is UGES. The 2nd stage state estimate is then used to determine a point for which a local linearization can be made of the original nonlinear measurement model. The 3rd stage KF is then used to provide a more accurate estimate based on this linearization. In the work done by A. Johansen et al. (2016) it is shown that the three-stage filter must be UGES because of the cascaded structure of the two UGES filters and the transformation.

Chapter 3

Modeling

This chapter aims to describe the mathematical modeling that lies behind the navigation system that is developed. Theory is mainly taken from Fossen (2011), and from this the matrix notation is also adopted. A kinematic model is described, and this has been used to simulate the motion of an ROV and is part of the kinematic filter model. Relevant measurement models for acoustic and acceleration measurements are also included. These are used for generating measurements during simulations, and are also part of the filter design.

3.1 Mathematical ROV model

According to Fossen (2011) a mathematical model for a robotic system can be divided into two parts, kinematics and kinetics. The kinematic model compromises the geometrical aspect of motion, without considering the cause of motion. The kinetic model considers the forces and moments that act on the body, and how these create motions.

Because the transformations and references frames of a moving vehicle are known, the kinematics will be accurate. More uncertainty is however associated with the forces and moments acting on a vehicle, causing the need for the kinetics to be more simplified and usually subject to a number of assumptions.

In the developed filters only the kinematic model of an ROV is considered. The vehicle kinetics are therefore not included. In practice this means that the proposed navigation system can be applied to any underwater vehicle, independent of its geometry and hydrodynamic properties. Kinetic modeling is therefore not further addressed in this

thesis.

3.2 Kinematics

In the following section kinematic relations are used to define motion in different reference frames.

3.2.1 Notation

The motion, position and orientation of a vehicle are given by vectors and generalized coordinates. The notation that will be used throughout this thesis, is based on a 6 DOF representation for vessels, given by (SNAME, 1950).

Table 3.1: Notation used for marine vessels, courtesy of SNAME (1950)

DOF		Forces and moments	Linear and angular velocities	Positions and Euler angles
1	motions in x-direction (surge)	X	u	x
2	motions in y-direction (sway)	Y	v	y
3	motions in z-direction (heave)	Z	w	z
4	rotations about the x-axis (roll)	K	p	ϕ
5	rotations about the y-axis (pitch)	M	q	θ
6	rotations about the z-axis (yaw)	N	r	ψ

3.2.2 Reference frames

A reference frame is needed in order to describe and represent any vehicle in motion. There exists several reference frames, and the most common ones are the North-East-Down frame (NED) and the body-fixed reference frame (BODY).

- NED, {n}
  The North-East-Down frame with axes $\{\mathrm{n}\} = [x_n, y_n, z_n]$ has an origin o_n defined relative to the Earth's reference ellipsoid. This frame is often defined as the tangent plane on the surface of the Earth moving with the craft. The x-axis points towards true North, the y-axis towards true East, and the z-axis points downwards normal to the Earth surface. For a vehicle operating with relatively low speed, within a

local area, so that the longitude and latitude can be assumed constant, the NED frame can be assumed inertial. This means that Earth's angular rate is neglected, and that Newton's laws are applicable (Fossen, 2011).

- BODY, {b}
  The body frame with axes {b} = $[x_b, y_b, z_b]$ and origin o_b is a coordinate frame fixed to the craft in motion. The origin of $\{b\}$ can be placed anywhere, but is most convenient on the centerline or at intersections of symmetry planes. This is also referred to as the Center of Origin (CO). The position and orientation of a craft is expressed relative to an inertial frame, while linear and angular velocity is described in a body-fixed frame.

A third relevant reference frame, is the measurement frame, MES, {m}, with axes {m} = $[x_m, y_m, z_m]$. Measurements obtained from instruments that are mounted on the vehicle will be given in the instrument's measurement frame, which is also in motion and moving with the body (Dukan, 2014). For the work done in this thesis the measurement frame is assumed coinciding with the BODY frame, so that measurements do not need to be transformed from {m} to {b}.

The test basin in the MC-laboratory has been used to perform experiments. This tank is illustrated in Figure 3.1, with the BODY frame for the ROV and the reference frame for the test basin. The test basin reference frame is defined by the Qualisys Motion Tracking (QMT) system, which is an underwater positioning system. The test basin reference frame is used as NED frame in experiments, in the same way that GNSS reference frame is used as NED frame in real life. The origin of the test basin reference frame is placed on the bottom of the basin, approximately in the middle of the tank.

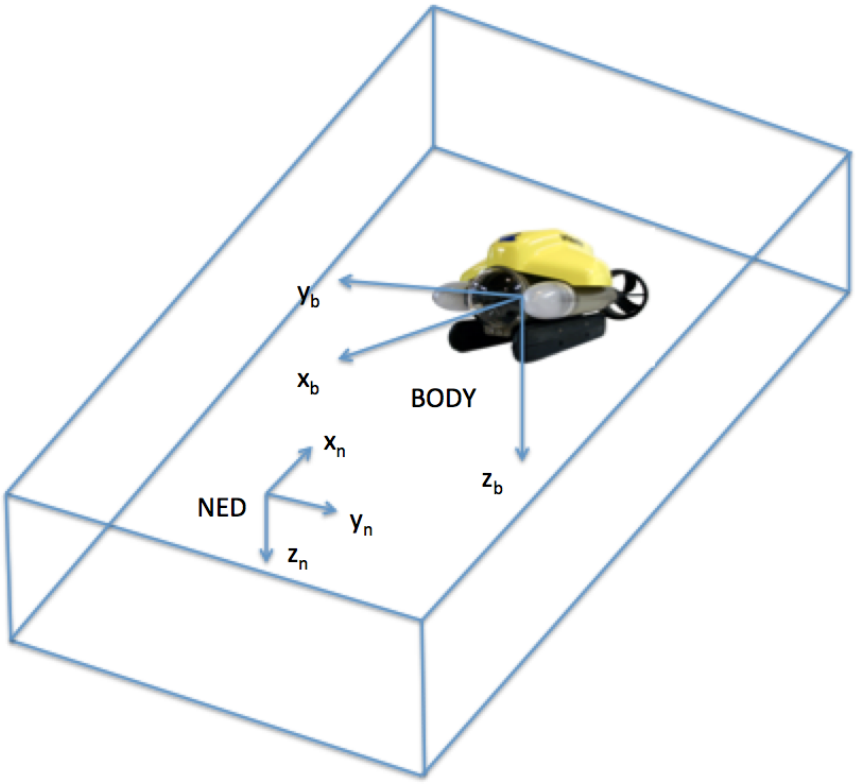

Figure 3.1: ROV BODY frame and NED frame in towing tank

3.2.3 Generalized coordinates

Generalized position and velocity coordinates are given by (3.1) and (3.2), respectively.

$$\eta = [x \;\; y \;\; z \;\; \phi \;\; \theta \;\; \psi]^\top \tag{3.1}$$

$$\nu = [u \;\; v \;\; w \;\; p \;\; q \;\; r]^\top \tag{3.2}$$

The linear and angular velocity vectors are sub-vectors of the generalized coordinates, and are given by (3.3).

$$p = \begin{bmatrix} x \\ y \\ z \end{bmatrix} \qquad v = \begin{bmatrix} u \\ v \\ w \end{bmatrix} \qquad \Theta = \begin{bmatrix} \phi \\ \theta \\ \psi \end{bmatrix} \qquad \omega = \begin{bmatrix} p \\ q \\ r \end{bmatrix} \tag{3.3}$$

where $p \in \mathbb{R}^{3\times1}$ is the linear position, $v \in \mathbb{R}^{3\times1}$ is the linear velocity, $\Theta \in \mathbb{R}^{3\times1}$ is the

vector of Euler angles and finally $\omega \in \mathbb{R}^{3\times 1}$ is the angular velocity or the turn rates of the body.

The orientation of a vehicle with respect to NED can be represented by means of Euler angles Θ, as defined in (3.3), or unit quaternions, $q \in \mathbb{R}^4$, defined in (3.4). The main motivation for using quaternions is that this notation avoids problems with singularities that occur in the angular transformation matrix, when expressing orientation using Euler angles. Compared to the Euler angle representation, the quaternion representation is also more computationally effective, as the linear and angular transformation matrices include less trigonometric functions. On the downside, the quaternion representation is less intuitive compared to using Euler angles.

$$Q := \{q \,|q^\top q = 1, q = [\eta, \varepsilon^\top]^\top,\ \varepsilon \in \mathbb{R}^3 \text{ and } \eta \in \mathbb{R}\} \tag{3.4}$$

where

$$q = \begin{bmatrix} \eta \\ \varepsilon_1 \\ \varepsilon_2 \\ \varepsilon_3 \end{bmatrix} \in Q \tag{3.5}$$

The quaternion must satisfy the geometric constraint, $q^T q = 1$. To ensure this, a normalization can done according to (3.6).

$$q_{k+1} = \frac{q_{k+1}}{\|q_{k+1}\|} \tag{3.6}$$

3.2.4 Transformations

A transformation is necessary to be able to change the representation of motion from one reference frame to another, for example from BODY to NED. The transformation function is denoted by J, more specifically J_q when attitude is expressed using the unit quaternion. The kinematics expressed using generalized coordinates in 6 degrees of freedom (DOF) are given in (3.7).

$$\dot{\eta} = J_q(\eta)\nu \tag{3.7}$$

where $\eta = [x, y, z, \eta, \varepsilon_1, \varepsilon_2, \varepsilon_3]^\top$, $\eta \in \mathbb{R}^7$, $\nu \in \mathbb{R}^6$ and $J_q(\eta) \in \mathbb{R}^{7\times 6}$ when using the quaternion representation for attitude. The 6 DOF kinematic equations are now expressed with seven differential equations, which can be written on matrix form according to (3.8).

$$\begin{bmatrix} \dot{p}^n_{b/n} \\ \dot{q} \end{bmatrix} = \begin{bmatrix} R^n_b(q) & 0_{3\times 3} \\ 0_{4\times 3} & T_q(q) \end{bmatrix} \begin{bmatrix} v^b_{b/n} \\ \omega^b_{b/n} \end{bmatrix} \tag{3.8}$$

The terms included in (3.8) are explained in the two following sections.

Linear velocity transformation

The linear velocity in NED frame, $v^n_{b/n}$, also denoted by $\dot{p}^n_{b/n}$, can be extracted from the matrix form of the kinematics (3.8) and gives

$$\dot{p}^n_{b/n} = R^n_b(q) v^b_{b/n} \tag{3.9}$$

where $R^n_b(q)$ is the linear transformation matrix, that transforms velocities in a body-fixed reference frame $\{b\}$ to the inertial frame $\{n\}$.

$$R^n_b(q) = \begin{bmatrix} 1-2(\varepsilon_2^2+\varepsilon_3^2) & 2(\varepsilon_1\varepsilon_2-\varepsilon_3\eta) & 2(\varepsilon_1\varepsilon_3+\varepsilon_2\eta) \\ 2(\varepsilon_1\varepsilon_2+\varepsilon_3\eta) & 1-2(\varepsilon_1^2+\varepsilon_3^2) & 2(\varepsilon_2\varepsilon_3-\varepsilon_1\eta) \\ 2(\varepsilon_1\varepsilon_3-\varepsilon_2\eta) & 2(\varepsilon_2\varepsilon_3+\varepsilon_1\eta) & 1-2(\varepsilon_1^2+\varepsilon_3^2) \end{bmatrix} \tag{3.10}$$

The position on a path or a trajectory, $p^n_{b/n}$, of a craft relative to the NED coordinate system can be found by numerical integration, here using Euler integration. Below h is the sampling time.

$$p^n_{b/n,k+1} = p^n_{b/n,k} + h \cdot R^n_b(q) \cdot v^b_{b/n,k} \tag{3.11}$$

In order to find the linear acceleration in the NED frame, $a^n_{b/n}$, or $\dot{v}^n_{b/n}$, the following property of the rotation matrix is used

$$\dot{R}^n_b = R^n_b S(\omega^b_{b/n}) \tag{3.12}$$

where $S(\omega^b_{b/n})$ is the skew-symmetric matrix, defined as

$$S(\omega_{b/n}^b) = \begin{bmatrix} 0 & -r & -q \\ r & 0 & -p \\ -q & p & 0 \end{bmatrix} \tag{3.13}$$

so that the linear accelerations in NED frame are found from

$$a_{b/n}^n = S(\omega_{b/n}^b) R_b^n v_{b/n}^b + R_b^n \dot{v}_{b/n}^b \tag{3.14}$$

Angular velocity transformation

The angular velocity transformation is also contained in the kinematics given by (3.8).

$$\dot{q} = T_q(q)\omega_{b/n}^b \tag{3.15}$$

where T_q is the angular transformation matrix expressed using the quaternions (3.16).

$$T_q(q) = \frac{1}{2} \begin{bmatrix} -\varepsilon_1 & -\varepsilon_2 & -\varepsilon_3 \\ \eta & -\varepsilon_3 & \varepsilon_2 \\ \varepsilon_3 & \eta & -\varepsilon_1 \\ -\varepsilon_2 & \varepsilon_1 & \eta \end{bmatrix} \tag{3.16}$$

Using Euler integration like in (3.11), the next quaternion is found by

$$q_{k+1} = q_k + h \cdot T_q(q) \cdot \omega_{b/n,k}^b \tag{3.17}$$

3.3 Measurement models

In the following sections, the relevant measurement models are described. These are used to put together the kinematic observer model. In simulations "perfect" measurements are generated, and noise is therefore modeled and added to these measurements to make simulations more realistic. Modeling of sensor noise and biases is explained further.

In physical experiments, measurements are further complicated by the fact that sensors can be placed and aligned in different positions on the ROV. The measurements will then

need to be transformed to the CO or another common point, so that all measurements are made relative to the same point on the body.

3.3.1 Gaussian white noise

Signal noise occurs both due to external and internal disturbances in sensors. Various types of noise is often either characterized as process or sensor noise. And due to its random nature, these will be modeled as random processes using stochastic variables. A random variable is described by a probability density function, defined by a variance and a mean.

The Gaussian or normal distribution is the most known probability function, and can be used to model noise. Gaussian white noise is normally distributed random process noise which contains all frequencies. A sensor measurement is typically on the form

$$y = Hx + w(t) \tag{3.18}$$

where $y \in \mathbb{R}^m$ contains the sensor measurements, $x \in \mathbb{R}^n$ is the state vector and $H \in \mathbb{R}^{m \times n}$ is the measurement matrix. $w(t)$ denotes the Gaussian white noise, and the Gaussian white noise process can be described as

$$w(t) \sim N(0, \sigma^2) \tag{3.19}$$

with zero mean, and variance σ^2.

3.3.2 Random walk process

The random walk process or the Wiener-motion process is Gaussian white-noise integrated. The variable $w(t)$ is then modeled as

$$\dot{w} = \varepsilon_b \tag{3.20}$$

where $\varepsilon_b \sim (0, \sigma_b^2)$. In turn this means that that the random walk process in theory has an infinite variance. The random-walk process is however often well behaved. It is suggested by Fossen (2011) to use a random walk for modeling slowly varying biases.

3.3.3 Range measurements

Range measurements can be found from TOA measurements, here denoted by t_i. Using the wave speed of sound under water, the acoustic range measurement is given by (3.21).

$$y_i = c_0 t_i \tag{3.21}$$

In Equation (3.21) c_o denotes the assumed sound wave propagation speed, and the subscript i indicates a measurement from transponder i. The wave speed is known to vary with pressure, temperature and salinity. The real propagation speed, c, can therefore be modeled as $c = \sqrt{\beta} c_0$, where the multiplicative bias-parameter, β, accounts for the uncertainty in this value. This is modeled as a random walk process, as described in Section 3.3.2.

$$\dot{\beta} = \varepsilon_\beta \tag{3.22}$$

where $\varepsilon_\beta \sim (0, \sigma_\beta^2)$. Let p^n and v^n denote the position and velocity of the ROV, and $\breve{p}_i^n$ denote the position of transponder i, all in NED frame. The geometric range, ρ_i, is given by a nonlinear function of the vehicle position, p^n, and the ith transponder position, $\breve{p}^n$, given by the Euclidean distance, denoted by $\|\cdot\|$.

$$\rho_i = \|p^n - \breve{p}_i^n\| \tag{3.23}$$

The measurements, y_i, are subject to zero-mean, Gaussian measurement noise, as described in Section 3.3.1. In the measurement equation (3.24) the range measurement is modeled with unknown wave propagation speed, and referred to as *pseudo-range* measurements.

$$y_i = \frac{1}{\sqrt{\beta}}(\rho_i + \varepsilon_{y,i}) \tag{3.24}$$

where $\varepsilon_{y,i} \sim (0, \sigma_y^2)$.

The range measurements are made relative to the position of the acoustic interrogator on the ROV. This means that the resulting positions that are based on the range measurements and trilateration principles have an offset or a lever arm with respect to the

CO of the ROV. This can be compensated for using the distance from the interrogator to the CO, according to

$$p_b^n = p_m^n - R(\Theta)l \tag{3.25}$$

where p_b is the position relative to vehicle origin, and p_m is the resulting position found from trilateration, $l \in \mathbb{R}^{3\times1}$ is the lever-arm, and $R(\Theta) \in \mathbb{R}^{3\times3}$ is the rotation matrix.

3.3.4 Acceleration measurements

Acceleration measurements are obtained from an IMU mounted on the moving vehicle. In Figure 3.2 the strapdown equations for both the accelerometers and gyroscopes are illustrated. The attitude is expressed in quaternions, q, and the figure clearly illustrates the interconnection between the position and attitude estimator. For the integration filters that are developed, the attitude is assumed available and will not be estimated, so that only the acceleration measurement equations are explained further.

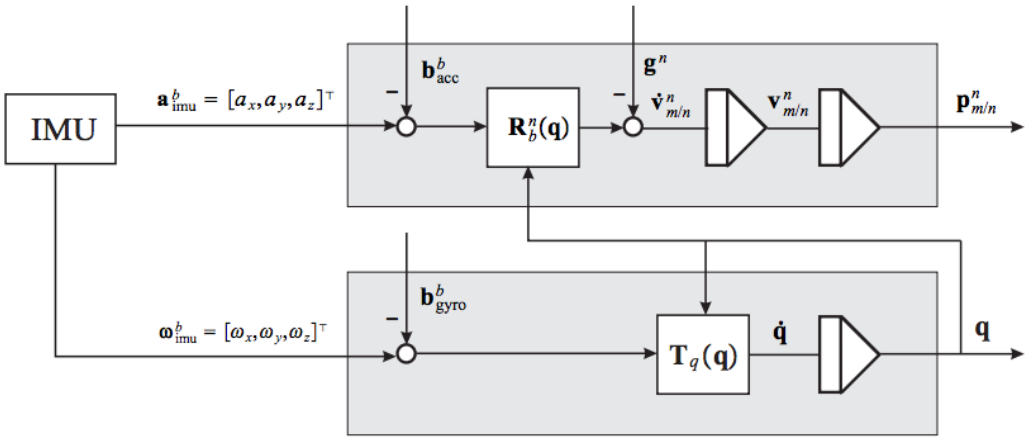

Figure 3.2: The strapdown INS equations, courtesy of Fossen (2012)

Typically three orthogonal accelerometers are used. The inertial sensor model is based on the strap-down assumption, which implies that the IMU is fixed to the BODY frame of the vehicle. This means that the reference frame for the IMU is aligned with the BODY frame, so that there are no misalignment errors between $\{m\}$ and $\{b\}$. Linear accelerations in NED are found by rotation of acceleration measurements obtained in BODY frame, as it also appears from Figure 3.2. The accelerometers in the IMU are subject to sensor biases. When these are double integrated, they cause an accumulative

error in position that grows quadratically with time. The acceleration measurements, $a^b_{imu} \in \mathbb{R}^{3\times1}$, are expressed by (3.26).

$$a^b_{imu} = R^b_n(q)[\dot{v}^n - g^n] + \varepsilon^b_{acc} + b^b_{acc} \tag{3.26}$$

where $R^b_n(q) \in \mathbb{R}^{3\times3}$ is the rotation matrix from $\{n\}$ to $\{b\}$, and $q = [\eta, \varepsilon_1, \varepsilon_2, \varepsilon_3]^\top$ is the unit quaternion. $\varepsilon^b_{acc} \in \mathbb{R}^{3\times1}$ is additive zero-mean measurement noise, and $b^b_{acc} = [b_u, b_v, b_w]^\top \in \mathbb{R}^{3\times1}$ represent accelerometer measurement biases, both obtained in the BODY frame. The acceleration noise is modeled as described in Section 3.3.1 and the acceleration biases are modeled as slowly time-varying disturbances, using a random-walk process, as described in Section 3.3.2. See Equation (3.27).

$$\dot{b}^b_{acc} = \varepsilon^b_{bacc} \tag{3.27}$$

where $\varepsilon^b_{bacc} \in \mathbb{R}^{3\times1}$ is Gaussian white noise. The gravity vector g^n is modeled as a constant vector in NED according to (3.28).

$$g^n = \begin{bmatrix} 0 \\ 0 \\ g \end{bmatrix} \tag{3.28}$$

The gravity vector varies across the globe, according to the distance away from the poles. The nominal "average" that typically is used is $g = 9.80665\, m/s^2$.

The INS strapdown assumption states that the IMU is fixed to the BODY frame, so that there are no misalignment errors between $\{m\}$ and $\{b\}$. The IMU can still be mounted with an offset with respect to the CO of $\{b\}$, denoted by $r^b_m = [x_m, y_m, z_m]^\top$. Instead of transforming the IMU measurements to the CO, a state estimator will usually be formulated in the measurement frame $\{m\}$. If desired, the estimated states can be transformed to the CO, using the lever arm, r^b_m (Fossen, 2012). This is especially important if control is made relative to this point. Control is not considered in this thesis, so all measurements are instead shifted to the position of the IMU on the ROV, ensuring that measurements are made relative to the same point.

Chapter 4

Integration filter design

Two different methods for integration inertial and pseudo-range measurements are considered. The selected filters are the TSF and the standard EKF. And in the following chapter the two different filter designs are described. In the set-up that is considered pseudo-range measurements are provided by four transponders, yielding four individual pseudo-range measurements. Acceleration measurements are made by an accelerometer triad, as a part of an IMU mounted on the ROV in motion. Both filters use pseudo-range and acceleration measurements to estimate position, velocity and bias parameters. The filters that are described is the novel formulation of the TSF, in addition to the standard EKF.

4.1 Observer model

The Kalman filter is formulated using the kinematic relations and the measurement models described in Chapter 3. The resulting system model is given by (4.1).

$$\begin{aligned} \dot{p}^n &= v^n \\ \dot{\beta} &= \varepsilon_\beta \\ \dot{v}^n &= R_b^n(q)[a_{imu}^b - \varepsilon_{acc}^b - b_{acc}^b] + g^n \\ \dot{b}_{acc}^b &= \varepsilon_{bacc}^b \end{aligned} \tag{4.1}$$

This includes acceleration measurements, modeled with a random-walk bias, and pseudo-range measurements. The slowly-varying bias parameter accounting for an unknown wave propagation speed is also estimated, in addition to the position and linear velocity. A

continuous state space model can be defined for the observer according to

$$\begin{aligned} \dot{x} &= Ax + Bu + Ew \\ y &= Hx + v \end{aligned} \tag{4.2}$$

where $y \in \mathbb{R}^{4\times 1}$ is the measurement vector, $H \in \mathbb{R}^{4\times 10}$ is the measurement matrix, and $w \in \mathbb{R}^{7\times 1}$ and $v \in \mathbb{R}^{4\times 1}$ is the process and measurement noise respectively. The system model is written on state space form and given by (4.1).

$$\begin{aligned} \dot{\chi} = &\begin{bmatrix} 0_{3\times 3} & 0_{3\times 1} & I_{3\times 3} & 0_{3\times 3} \\ 0_{1\times 3} & 0_{1\times 1} & 0_{1\times 3} & 0_{1\times 3} \\ 0_{3\times 3} & 0_{3\times 1} & 0_{3\times 3} & -R_b^n(q) \\ 0_{3\times 3} & 0_{3\times 1} & 0_{3\times 3} & 0_{3\times 3} \end{bmatrix} \chi + \begin{bmatrix} 0_{4\times 3} & 0_{4\times 3} \\ R_b^n(q) & I_{3\times 3} \\ 0_{3\times 3} & 0_{3\times 3} \end{bmatrix} u \\ &+ \begin{bmatrix} 0_{3\times 1} & 0_{3\times 3} & 0_{3\times 3} \\ 1 & 0_{1\times 3} & 0_{1\times 3} \\ 0_{3\times 1} & -R_b^n(q) & 0_{3\times 3} \\ 0_{3\times 1} & 0_{3\times 3} & I_{3\times 3} \end{bmatrix} \varepsilon \end{aligned} \tag{4.3}$$

where $\chi \in \mathbb{R}^{10\times 1}$ is the estimated state vector from the filter. The process noise in the system is defined as in (4.4).

$$\varepsilon = \begin{bmatrix} \varepsilon_\beta \\ \varepsilon_{acc}^b \\ \varepsilon_{bacc}^b \end{bmatrix} \tag{4.4}$$

The input to the system is given by

$$u = \begin{bmatrix} a_{imu}^b \\ g^n \end{bmatrix} \tag{4.5}$$

where a_{imu}^b are the acceleration measurements from the IMU, and g^n is the gravity vector.

4.2 Discretization

The observers that are implemented use the discrete Kalman filter design. The discrete state space formulation used is stated below.

$$\begin{aligned} x_{k+1} &= \phi x_k + \Delta u_k + \Gamma w_k \\ y_k &= H x_k + v_k \end{aligned} \tag{4.6}$$

where $x_{k+1} \in \mathbb{R}^{10\times 1}$ is the state vector containing the ten states. $\phi \in \mathbb{R}^{10\times 10}$ is the state transition matrix relating the previous state to the next, $\Delta \in \mathbb{R}^{10\times 6}$ relates the control input to the next state and finally $\Gamma \in \mathbb{R}^{10\times 7}$ relates white noise to the next state vector. The system matrices are discretized using Euler integration according to

$$\begin{aligned} \phi = exp(Ah) &\approx I + Ah \\ \Delta &= A^{-1}(\phi - I)B \\ \Gamma &= A^{-1}(\phi - I)E \end{aligned} \tag{4.7}$$

which can easily be obtained in MATLAB, by using the in-built function *c2d*. Above h is the sampling time.

4.3 Discrete Kalman Filter Design

The recursive discrete Kalman filter is developed based on the optimization criteria of minimizing the mean-square estimation error of a random process. It is assumed that the covariances of the process noise and the sensor noise are Gaussian distributed and given by $w \sim N(0, Q)$ and $v \sim N(0, R)$ respectively. Also, these are assumed uncorrelated with each other.

The Kalman equations were developed in Kalman (1960). Initial conditions are defined for the filter

$$\begin{aligned} \bar{x}_0 &= x_0 \\ \bar{P}_0 &= E\left[(x_0 - \hat{x}_0)(x_0 - \hat{x}_0)^\top\right] = P_0 \end{aligned} \tag{4.8}$$

where x_0 is the initial estimate of the filter, and P_0 is the initial covariance of the state estimate. P_0 is therefore an indication of how correct the initial estimate of the filter

is. The Kalman gain matrix is determined by computing previous covariances estimates weighing the sensor updates against the noise in the process.

$$K_k = \bar{P}_k H^\top [H \bar{P}_k H^\top + R_k]^{-1} \tag{4.9}$$

The corrected estimates for the states and the covariance are then found, using the Kalman gain, K_k.

$$\begin{aligned} \hat{x}_k &= \bar{x}_k + K_k[y_k - h(\bar{x}_k)] \\ \hat{P}_k &= [I - K_k H_k]\bar{P}_k[I - K_k H_k]^\top + K_k R_k K_k^\top \end{aligned} \tag{4.10}$$

where $R_k = R_k^\top$. The projected estimates for the next step are given by

$$\begin{aligned} \bar{x}_{k+1} &= \phi_k \hat{x}_k + \Delta u_k \\ \bar{P}_{k+1} &= \phi_k \hat{P}_k \phi_k^\top + \Gamma_k Q_k \Gamma_k^\top \end{aligned} \tag{4.11}$$

where $Q_k = Q_k^\top$. Based on the equations it is seen that a small R compared to Q, will give a large K_k favoring the measurements rather than the model. When R is large compared to Q, K_k is small, and the model is emphasized more than the measurements.

4.4 Three-Stage filter

The TSF as described in Section 2.6.5, is here described in more detail. In Figure 4.1 the different stages, and the information flow in the filter is illustrated. Σ_1, Σ_2 and Σ_4 are the three stages that give the filter its name.

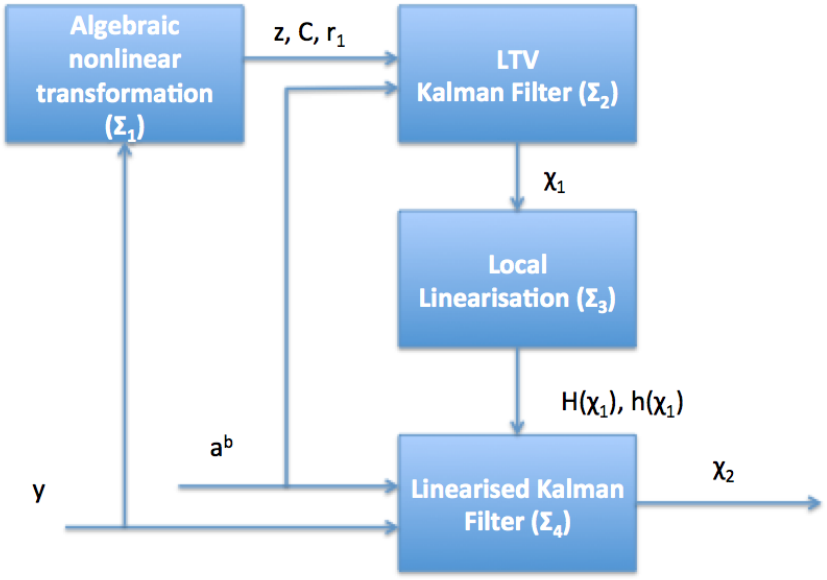

Figure 4.1: Structure of TSF

In Figure 4.1 $y \in \mathbb{R}^{4\times 1}$ denotes the pseudo-range measurements, and $a^b_{imu} \in \mathbb{R}^{3\times 1}$ are acceleration measurements obtained in $\{b\}$. χ_1 is the state estimate produced by the exogenous, LTV Kalman filter, and is used as linearization point for the second KF. This first state estimate is used to evaluate the linearized measurement matrix and model given by $H(\chi_1)$ and $h(\chi_1)$. The final estimate from the TSF is denoted χ_2 and is obtained from the linearized Kalman filter, in the last and third stage. In the following sections, each of the stages of the TSF are explained further.

4.4.1 Nonlinear algebraic transformation

The algebraic nonlinear transformation, as briefly described in Section 2.6.5, is used to construct "new measurements" from the pseudo-range measurements, so that the system can be described on a LTV form. The technique used for relating the states linearly to the measurements, is based on work done by B. Stovner et al. (2016). The constructed measurement equation with noise is given by

$$y_i^2 = \frac{1}{\beta}(\rho_i + 2\varepsilon_{y,i}\rho_i + \varepsilon_{y,i}^2) \tag{4.12}$$

where $\rho_i = (p^n - \breve{p}^n)^\top (p^n - \breve{p}_i^n)$ is the geometric range, and $\varepsilon_{y,i}$ is the noise contained in the pseudo-range measurements. Considering the mean of the constructed measurement,

it is found that these are biased due to the influence of noise. The estimated mean of a stochastic variable and a squared stochastic variable is given by $E[X] = 0$ and $E[X^2] \neq 0$ respectively. This results in the following bias of the constructed measurement

$$\begin{aligned} m_{y,i} = E(y_i^2 - \frac{1}{\beta}\rho_i^2) = \frac{1}{\beta}\sigma_y^2 \\ m_y = \frac{1}{\beta}\sigma_y^2 \end{aligned} \tag{4.13}$$

The bias, m_y, should be subtracted from the squared measurements, y_1^2, before these are used in the algebraic transformation.

Expanding and rearranging the left-hand side of the expression given by (4.12) gives

$$\beta y_i^2 = r - 2\breve{p}_i^{n\top} p^n + \|\breve{p}_i^n\|^2 + 2\varepsilon_{y,i}\rho_i + \varepsilon_{y,i}^2 \tag{4.14}$$

where $r = p^{n\top} p^n$. Considering the case of four transponders, the partial state vector and a selection matrix can be defined

$$x = \begin{bmatrix} p^n \\ \beta \end{bmatrix} \qquad M = \begin{bmatrix} 1 & 0 & 0 & 0 \\ 0 & 1 & 0 & 0 \\ 0 & 0 & 1 & 0 \\ 0 & 0 & 0 & 0 \end{bmatrix} \tag{4.15}$$

By using the selection matrix M, r can be expressed in terms of x according to

$$r = x^\top M x \tag{4.16}$$

Not considering noise in the measurements, (4.14) can now be written on the form

$$C_y x - rl = z \tag{4.17}$$

where

$$C_y = \begin{bmatrix} C_{yp} & C_{y\beta} \end{bmatrix} \qquad C_{yp} = \begin{bmatrix} 2\breve{p}_1^{n\top} \\ \vdots \\ 2\breve{p}_4^{n\top} \end{bmatrix} \qquad C_{y\beta} = \begin{bmatrix} y_1^2 \\ \vdots \\ y_4^2 \end{bmatrix} \tag{4.18}$$

where $l = [1, 1, 1, 1]^\top$ and $z = [\|\breve{p}_1^n\|^2, \ldots, \|\breve{p}_4^n\|^2]^\top$. If C_y has full rank, so that it is invertible, the position measurements and the bias parameter, β, contained in the state vector x, can be expressed as

$$x = rC_y^{-1}l + C_y^{-1}z = rc + w \tag{4.19}$$

where $c = C_y^{-1}l$ and $w = C_y^{-1}z$. Inserting (4.19) into (4.16), will give a second order equation with respect to r.

$$\begin{aligned} r &= (rc + w)^\top M(rc + w) \\ r &= r^2c^\top Mc + 2rc^\top Mw + w^\top Mw \\ r^2c^\top Mc &+ r(2c^\top Mw - 1) + w^\top Mw = 0 \end{aligned} \tag{4.20}$$

The second-order equation gives two solutions, expressed using the defined term h = $2c^\top Mw - 1$.

$$r_{1,2} = \frac{-h \pm \sqrt{h^2 - 4c^\top Mc \cdot w^\top Mw}}{2c^\top Mc} \tag{4.21}$$

Equation (4.21) has to possible solutions, where one of them is correct and the other one is wrong, denoted r_1 and r_2 respectively. In order to solve the ambiguity related to r_1 and r_2, domain knowledge can be used to exclude one of the solutions. In underwater navigation all the transponders will usually be located on the seabed and the vehicle will be above these at all times. Positions below the seabed can then be ruled out. Bounds on β can also be used to obtain the correct solution to the second-order equation, as the two solutions typically have significantly different estimates of β. Another approach is to introduce an additional depth measurement to rule out the ambiguity (A. Johansen et al., 2016). For this implementation the solution to the second order equation given by (4.21) is selected by choosing the solution of r that gives a pseudo-range bias parameter, β, closest to one.

Finally, the constructed measurement equation, which is now linearly time-varying in C(t), in the case of four transponders, $m = 4$, can be written as

$$C(t)\chi - lr_1 = z \tag{4.22}$$

where χ is the state vector, l is defined from earlier and r_1 is the chosen solution to

Equation (4.21). Written out in further detail

$$\begin{bmatrix} C_{yp} & C_{y\beta} & 0_{4\times 6} \end{bmatrix} \begin{bmatrix} p^n \\ \beta \\ v^n \\ b^b_{acc} \end{bmatrix} - lr_1 = z \tag{4.23}$$

It is worth mentioning that the quasi-linear time-varying measurement model, given by (4.23), is free of approximations in the noise-free case. However, in the case of noise in the pseudo-range measurements, nonlinear relationships are eliminated in order to perform the transformation and to get a global quasi-linear model. This causes sub-optimal estimation in presence of noise.

4.4.2 LTV Kalman filter

The dynamics of the LTV Kalman filter is described on matrix form as in (4.3), and the linear measurement model found from the algebraic transformation is described by (4.23). The state estimate produced by this filter is denoted χ_1. This state estimate is GES, but is sup-optimal in presence of noise, and is used as linearization point for the final linearized Kalman filter. Because of the new, constructed measurement model, the sensor covariance matrix must be found accordingly. The covariance for each constructed measurement is found from calculating the resulting variance of the squared range measurement given by (4.12). Using that the variance of a stochastic variable and a squared stochastic variable is defined as $Var[X] = \sigma^2$ and $Var[X^2] = 2\sigma^4$, results in the following variance of the constructed measurements

$$R_{y,i}(t) = Var(y_i^2) = \frac{2}{\beta^2}(2\rho_i^2\sigma_y^2 + \sigma_y^4) \tag{4.24}$$

Finally, the sensor variance matrix for the LTV Kalman filter is given by (4.25).

$$R(t) = diag([R_{y,1}(t), ..., R_{y,4}(t)]) \tag{4.25}$$

4.4.3 Linearized Kalman filter

The linearized Kalman filter is described using the same process model as given by (4.3), but uses the original nonlinear measurement model. In order to linearize the measurement model, a first-order Taylor-series approximation of the measurement function is used. The linearized measurement matrix is given by

$$H(\chi_1) = \left[\begin{array}{c} \frac{dh_1(\chi)}{d\chi} \\ \vdots \\ \frac{dh_{m(\chi)}}{d\chi} \end{array}\right]\Bigg|_{\chi=\chi_1} \in \mathbb{R}^{m\times 10} \tag{4.26}$$

where $h(\chi)$ is the nonlinear measurement model defined for each of the pseudo-range measurements. Using four acoustic range measurements, so that m = 4, and using the definition of the geometric range, (3.23), the measurement matrix can be written as in (4.27).

$$H = \begin{bmatrix} \frac{(p^n-\check{p}_1^n)^\top}{\sqrt{\beta}\|p^n-\check{p}_1^n\|} & -\frac{\|p^n-\check{p}_1^n\|}{2\beta^{\frac{3}{2}}} & \cdots & 0 \\ \vdots & \cdots & \cdots & 0 \\ \frac{(p^n-\check{p}_4^n)^\top}{\sqrt{\beta}\|p^n-\check{p}_4^n\|} & -\frac{\|p^n-\check{p}_4^n\|}{2\beta^{\frac{3}{2}}} & \cdots & 0 \end{bmatrix} \in \mathbb{R}^{4\times 10} \tag{4.27}$$

A first-order Taylor approximation of the measurement function is found as

$$h(\chi) \approx h(\chi_1) + H(\chi_1)(\chi - \chi_1) \tag{4.28}$$

where χ_1 is the state estimate obtained from the first KF. As linearization point either $\hat{\chi}_1$ or $\bar{\chi}_1$ can be used. The projected estimate, $\bar{\chi}_1$, is more noisy, while the corrected estimates, $\hat{\chi}_1$, is subject to less noise, but correlated with the measurements (B. Stovner et al., 2016). Here the latter is used. For the linearized Kalman filter, the estimate χ in (4.28) is the filters own projected estimate, here denoted $\bar{\chi_2}$.

Because the linearized Kalman filter keeps the nonlinear measurement model, the sensor covariance matrix is straightforward to find, and is simply given by the variance of the noise present in each pseudo-range measurement.

$$R(t) = diag([\sigma_y^2, ..., \sigma_y^2]) \tag{4.29}$$

The sensor covariance matrix (4.29), is the same for the linearized KF as the EKF.

4.5 Extended Kalman Filter

The EKF is described by the same kinematic model as given by (4.3). In fact, the only difference between the linearized KF and the EKF, is that the EKF is linearized about its own state estimate. This implies that the linearized measurement matrix given by (4.27) is evaluated at the EKF's own projected estimate, $\bar{\chi}$. And because the EKF uses no external estimate, $\chi = \chi_1$, and the nonlinear measurement model reduces to the first term only given by (4.28). Figure 4.2 shows the structure of the EKF, and clearly illustrates the feedback-loop that can potentially cause the filter to diverge (Johansen and Fossen, 2016a).

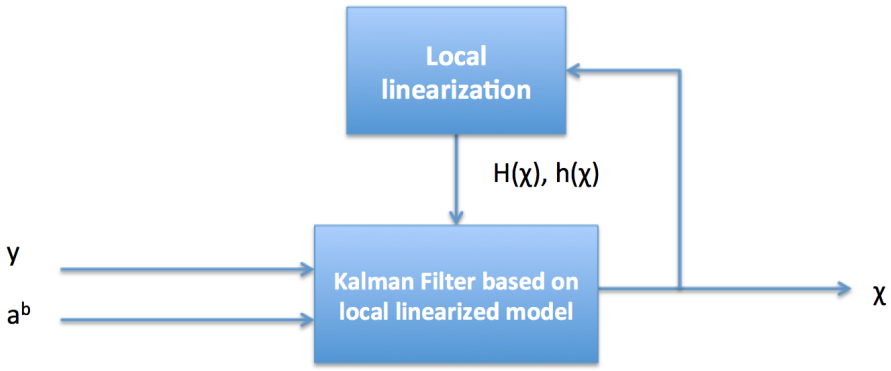

Figure 4.2: Structure of EKF

In Figure 4.2 y and a^b_{imu} denote pseudo-range and acceleration measurement respectively, like before. The state estimate from the EKF, χ, is used to evaluate the measurement matrix, $H(\chi)$, and the measurement model, $h(\chi)$.

4.6 Observability

The ultimate goal of an observer is to reconstruct unmeasured states from the available sensor and input measurement, denoted y and u respectively. For this to be possible, the system needs to be *observable*. Observability of a system implies that for any possible sequence of state and control vectors, the current state can be estimated using only the

outputs. The observability proof for the TSF follows the procedure as describe in the work by Stovner et al. (2017).

According to Kalman and Bucy (1961) a linear time-varying system is UGES if the pair *(A(t),C(t))* is uniformly completely observable (UCO), and if *(A(t),E(t))* is also uniformly completely controllable (UCC), where *(A(t), C(t))* and *E(t)* are the general process, measurement and process noise matrices respectively.

4.6.1 Uniform observability

In order to show observability for a linearly time-varying system, Theorem 6.012 from Chen (2013) is used. The pair *(A(t), C(t))* is observable if the observability co-distribution, given by (4.30)

$$d\mathcal{O} = \begin{bmatrix} N_0(t) \\ N_1(t) \\ \vdots \\ N_{n-1}(t) \end{bmatrix} \tag{4.30}$$

has rank n for all t, where n is the dimension of the state space, and where

$$N_{m+1}(t) = N_m(t)A(t) + \frac{d}{dt}N_m(t) \tag{4.31}$$

for $m = 0, 1, ..., n-1$. $N_0(t)$ is given by

$$N_0 = C(t) \tag{4.32}$$

In order to complete the observability proof, two assumptions regarding the algebraic transformation and the transponder placement must be made.

Assumption 1: The ambiguity regarding the algebraic solution, r_1 and r_2 can be solved, for example using domain knowledge, when the number of transponder, is m = 4.

Assumption 2: The transponder placement must be non-coplanar, i.e. the transponders cannot lie in the same plane.

In order to simplify the observability and controllability proof, the following corollary is used.

Corollary 1: For the block triangular matrix as given below

$$M = \begin{bmatrix} D & 0 \\ E & F \end{bmatrix} \tag{4.33}$$

D, E and F are matrices of arbitrary dimensions. M has full rank if D and F have full rank, indicating that E is insignificant when it comes to evaluating the rank of the matrix.

4.6.2 Uniform controllability

The controllability proof follows a very similar procedure, and is obtained from Chen (2013), Theorem 6.12. The pair *A(t), E(t)* is controllable if the controllability co-distribution given by (4.34)

$$d\mathcal{C} = \begin{bmatrix} M_0(t) & M_1(t) \dots M_{n-1}(t) \end{bmatrix} \tag{4.34}$$

has rank n for all t, where

$$M_{m+1}(t) = -A(t)M_m(t) + \frac{d}{dt}M_m(t) \tag{4.35}$$

where $m = 0, 1, ..., n-1$. $N_0(t)$ is given by

$$M_0 = E(t) \tag{4.36}$$

4.6.3 Observability for LTV Kalman filter

When conducting the observability proof, it turns out that it is sufficient to evaluate the first 3m rows of the observability distribution given by (4.30), where m is the number of range measurements. The measurement matrix for the LTV KF was found using the algebraic transformation, and is given by (4.23). The system matrix, $A(t)$, is defined as in (4.3). Calculations yield a observability co-distribution according to

$$d\mathcal{O}_{\chi_1} = \begin{bmatrix} C_{yp} & C_{p\beta} & 0_{4\times3} & 0_{4\times3} \\ \star & \star & C_{yp} & 0_{4\times3} \\ \star & \star & \star & -R_b^n(q)C_{yp} \end{bmatrix} \tag{4.37}$$

where C_{yp} and $C_{p\beta}$ is defined from earlier, and $R_b^n(q)$ is the rotation matrix from {b} to {n}. Assumption 1 must be valid, so that the LTV measurement matrix, $C(t)$, can be defined. And under assumption 2, the matrix $C = [C_{yp},\ C_{p\beta}]$ has full rank. Using Corollary 1 as stated in the previous section, the observability co-distribution, given by $d\mathcal{O}_{\chi_1}$ must have full rank. Consequently, it is found that for the linearized Kalman filter, $\text{rank}(d\mathcal{O}_{\chi_1}) = 10$, and the system is UCO.

4.6.4 Observability for linearized Kalman filter

Similarly for the second Kalman filter, only the first 3m rows of the observability distribution is needed in order to prove observability. For the linearized Kalman filter, the original nonlinear measurement matrix is linearized, and given by (4.27). The process matrix $A(t)$ is the same as for the LTV Kalman filter. The resulting 3m rows of the observability co-distribution becomes

$$d\mathcal{O}_{\chi_2} = \begin{bmatrix} H_{\chi_2}(\hat{\chi_1}) & 0_{4\times3} & 0_{4\times3} \\ \star & H^*_{\chi_2}(\hat{\chi_1}) & 0_{4\times}3 \\ \star & \star & -R_b^n(q)H^*_{\chi_2}(\hat{\chi_1}) \end{bmatrix} \tag{4.38}$$

where $H^*_{\chi_2}(\hat{\chi_1})$ is the extracted first column of the measurement matrix $H_{\chi_2}(\hat{\chi_1})$, which is given by

$$H^*_{\chi_2}(\hat{\chi_1}) = \begin{bmatrix} \frac{(p^n - \check{p}_1^n)^\top}{\sqrt{\beta}\|p^n - \check{p}_1^n\|} \\ \vdots \\ \frac{(p^n - \check{p}_4^n)^\top}{\sqrt{\beta}\|p^n - \check{p}_4^n\|} \end{bmatrix} \in \mathbb{R}^{4\times3} \tag{4.39}$$

This observability proof also requires assumption 2 to hold, because the measurement matrix H_{χ_2} contains the transponder positions. Again, Corollary 1 is used to establish $rank(d\mathcal{O}_{\chi_2}) = 10$. The linearized KF is also UCO.

The observability proof conducted for the second Kalman filter, Σ_4, is the same as for the EKF, because the measurement matrix H and the process matrix $A(t)$ are defined

equally. The EKF is also UCO.

4.6.5 Stability for TSF and EKF

Because the filters Σ_2, Σ_4 and the EKF share the same dynamics, the controllability proof is the same. The controllability co-distribution found by evaluating the process and the process noise matrices , $A(t)$ and $E(t)$, was found to be

$$d\mathcal{C}_\chi = \begin{bmatrix} 0_{3\times1} & 0_{3\times3} & 0_{3\times3} & 0_{3\times1} & R_b^n(q) & 0_{3\times3} \\ 1 & 0_{1\times3} & 0_{1\times3} & 0 & 0_{1\times3} & 0_{1\times3} \\ 0_{3\times1} & -R_b^n(q) & 0_{3\times3} & 0_{3\times1} & 0_{3\times3} & R_b^n(q) \\ 0_{3\times1} & 0_{3\times3} & I_{3\times3} & 0_{3\times1} & 0_{3\times3} & 0_{3\times3} \end{bmatrix} \tag{4.40}$$

Because $rank(d\mathcal{C}_\chi) = 10$, the unforced system dynamics as described in (4.3) are UCC. The LTV KF in the first stage of the TSF is shown to be both UCO and UCC. According to Kalman and Bucy (1961) the LTV system is then UGES. The matrix pairs (A(t), H(t)) and (A(t), E(t)) for the linearized KF, are also found to be UCO and UCC respectively.

Stability for the TSF is established using Theorem 2.1 from Johansen and Fossen (2016a). The LTV system is proved UGES, and the tuning parameters used in the filters, P(0), Q and R are symmetric and positive definite. From Theorem 2.1, using GES estimates, χ_1, to linearize about, the error dynamics of the cascaded system, Σ_1-Σ_4, are GES if the linearized KF is also UCO and UCC.

The EKF state estimate cannot be proved GES using the same procedure, because the proof by Kalman and Bucy (1961) applies only to LTV systems. Consequently the linearization is not made using a GES estimate, and the filter obtains only local stability.

4.6.6 Condition number and degree of observability

The standard tool for checking observability of a nonlinear dynamic system is the observability rank condition, which is checked in Section 4.6.3 and 4.6.4. However, this will only provide a yes or no answer to the question if the system is observable. But considering the estimation condition number, that is the condition number of the measurement matrix in the filter, the *degree of unobservability* can in stead be evaluated. The estimation condition number is the ratio of the largest local singular value to the smallest. When the condition number becomes high, the estimation problem becomes ill-conditioned. The

effect on the output because of a small change in the initial condition in one direction can then be overwhelmed by the effect on the output of a change in another direction (Bayat and Aguiar, 2012). This means that if the condition number becomes large enough, the system can in practice become unobservable.

Chapter 5

Implementation of navigation system

The TSF and EKF were implemented in MATLAB according to the description given in Chapter 4. A simulator was built in order to verify the implementation of the filters, and to compare their performance. Two different experiments were also conducted to collect sensor data that was tested in the filters. This chapter aims to give an overview of how the simulator works and a further explanation of the experimental work that was conducted.

5.1 Simulator

A simulator was developed in MATLAB, based on the kinematic model and measurement equations as explained in Chapter 3. It was assumed that the ROV operates within the range of a LBL transponder network, and that it operates with an IMU, and that these are the measurements available for navigation. The EKF and the TSF were implemented in MATLAB as described in Chapter 4, and were tested in simulations. In Figure 5.1 an effort is made to illustrate the overall structure of the code running the simulator. Here a^b_{imu} denotes acceleration measurements from the IMU, and $y_1, .., y_n$ denote pseudo-range measurements delivered by the LBL network. In addition to bias parameters, the filters estimate the position and linear velocities, given by p^n_{est} and v^n_{est} respectively in the figure below.

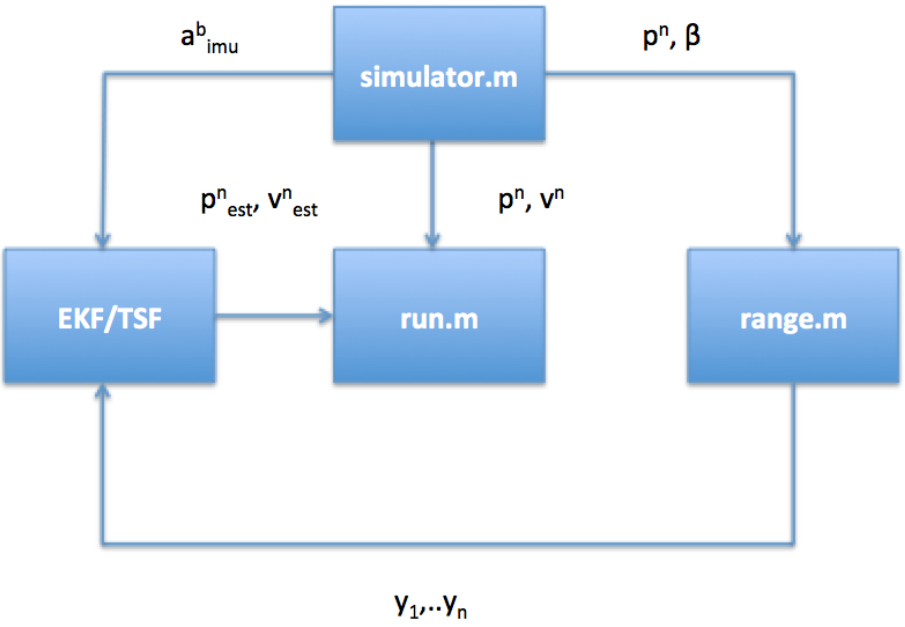

Figure 5.1: Structure of MATLAB simulator

The simulator was built based on an object-oriented approach. This implies that logical subgroups are implemented as separate *classes* or *objects*. This is a way of collecting variables and functions that naturally fit together, which will contribute to more structured programs for large applications. It can also help the process of debugging and introducing changes to the code.

In order to generate pseudo-range measurements during simulations, transponder positions had to be constructed. The configuration could be chosen arbitrary but aimed at being non-coplanar, as reasoned in Section 4.6. The placement of the transponders was assumed on the seabed, which allowed little vertical separation, typical for underwater range-based positioning. The transponder positions in NED frame are listed below (5.5).

$$\begin{aligned} \breve{p}_1^n &= [10, 10, 0]^\top & \breve{p}_2^n &= [10, -10, 1]^\top \\ \breve{p}_3^n &= [-10, 10, 2]^\top & \breve{p}_4^n &= [-10, -10, 0]^\top \end{aligned} \tag{5.1}$$

All measurement noise was modeled as Gaussian white noise, defined by zero mean and a standard deviation. The acceleration measurements were modeled to contain Gaussian white noise given by $\sigma_v = 0.01$ and the pseudo-range measurements contained white noise with standard deviation $\sigma_y = 0.1$. The variance of the unknown wave speed parameter was tuned empirically, and set to $\sigma_\beta = 10^{-2}$. The sensor covariance matrices

are specified in Chapter 4, as these depend on how the measurement model is defined. The process covariance matrix was similar for all filters, and is defined by the wave speed bias, acceleration noise and acceleration bias variance, according to (5.2).

$$Q = diag([\sigma_\beta^2, \sigma_v^2, \sigma_v^2, \sigma_v^2, \sigma_{bacc}^2, \sigma_{bacc}^2, \sigma_{bacc}^2]) \tag{5.2}$$

where $\sigma_{bacc} = 10^{-2}$. The filters were updated with a frequency of 100 Hz, equivalent to a sampling time of h = 0.01 seconds. Measurements from the IMU were assumed gathered with a frequency of 100 Hz, while pseudo-range measurements were available at a frequency of 2 Hz.

In order to evaluate the estimation error, the Root-Mean-Square (RMS) error was calculated. The formula for RMS is given by Equation (5.3).

$$RMS = \sqrt{\frac{1}{N}\sum_{i=1}^{N}(\hat{x}(i) - x_{true}(i))^2} \tag{5.3}$$

where N is the number of samples in a time-series, $\hat{x}(i)$ is the estimated value and $x_{true}(i)$ is the true value for sample i.

5.1.1 Simulation I

For steady-state behavior the filters were initiated with correct initial conditions for all states. In the simulator the ROV was tested for a lawn-mower trajectory, which corresponded to initial conditions $p_0 = [0, 0, 0]^\top$, $\beta_0 = 1$, $v_0 = [0, 0, 0]^\top$ and $b_{acc,0} = [0.1, 0.05, -0.13]^\top$. Simulations were run for 300 seconds. The initial covariance for all filters were set to $P(0) = diag([5 \cdot 10^{-4}, 5 \cdot 10^{-4}, 5 \cdot 10^{-5}, 10^{-5}, 10^{-4}, 10^{-4}, 10^{-4}, 10^{-4}, 10^{-4}, 10^{-4}])$.

5.1.2 Simulation II

For transient behavior the filters were initiated with erroneous initial conditions for all states. For the lawn mower trajectory $p_0 = [10, -15, -10]^\top$, $\beta_0 = 0.8751$, $v_0 = [0.1, 0.2, 0.1]^\top$ and $b_{acc,0} = [0, 0, 0]^\top$ were used. Simulations were like before run for 300 seconds. The initial covariance was now changed to $P(0) = diag([10, 10, 10, 10^{-3}, 10^{-3}, 10^{-3}, 10^{-3}, 5 \cdot 10^{-3}, 5 \cdot 10^{-3}, 5 \cdot 10^{-3}])$ for the LTV KF and the linearized KF, while for

the EKF $P(0) = diag([10^{-2}, 10^{-2}, 10^{-2}, 10^{-4}, 5 \cdot 10^{-4}, 5 \cdot 10^{-4}, 5 \cdot 10^{-4}, 10^{-4}, 10^{-4}, 10^{-4}])$ was used.

5.1.3 Execution time

The computing power demanded by an integration filter is an important aspect if it should be implemented on embedded hardware. The need for computer power is decided by the execution time of the filter. An indication of how much computer power is needed for each of the filters is found by measuring the mean execution time per iteration for each of the filters. This was done using the *tic/toc* function in MATLAB.

5.2 Physical experiments

The following sections aim to describe the physical experiments, which were done to collect sensor data, that was later used for testing the integration filters in offline runs. Offline testing in this context means that sensor data that was logged during experiments, later was run through the integration filters. The benefit of doing offline tests, is that tuning and debugging can be done after data is collected, and in many turns, without having to carry out the experiments again. In other words, offline estimation can save a lot of time. All experimental work was executed in the MC-lab at NTNU, which has a small-scale test basin that facilitates underwater experiments. Experiments were conducted using both the Videoray Pro 4 ROV as well as the Seabotix LBV600-6 ROV. More information about the ROVs and sensors will be given next.

5.2.1 Experiment I

In the first experiment conducted, the Videoray Pro 4 ROV was used. QMT was used to obtain the position and attitude estimates of the ROV under water. More details about the QMT system is given in Section 5.2.5. The QMT position estimates were for these experiments used for constructing pseudo-range measurements, in addition to being used as ground truth for the position estimated by the integration filters. The orientation estimates it provides were also used for rotating the IMU acceleration measurements from $\{b\}$ to $\{n\}$. The IMU acceleration measurements were logged with a frequency of 100 Hz, while the pseudo-range measurements were made available at 2 Hz.

For the collected sensor data, two different offline tests were run. The initial conditions were known so that the filters could be tested in steady-state behavior by initializing the filters correctly. By making the initial conditions inaccurate, the filters were also tested in transient behavior.

5.2.2 Experiment II

The second experiment was conducted by Bård B. Stovner and Eirik Henriksen, using the the SeaBotix LBV600-6 in the test basin. This time the Water Linked system was installed in the basin, and acoustic range measurements were obtained for the SeaBotix during testing. Similarly for this experiment, QMT position served as ground truth for the position estimated by the filters. Orientation was also needed this time to rotate the IMU acceleration measurements.

The IMU measurements were available with a frequency of 100 Hz, while Qualisys was logged at approximately 5 Hz. The acoustic range measurements were available at approximately 0.8 Hz, but with slight variations during the experiment. All sensor data was logged during the experiment, and used to test the filters in both steady-state as well as transient behavior.

5.2.3 The Videoray Pro 4 ROV

The Videoray Pro 4 ROV is a small observation class ROV that is used at NTNU, Tyholt for scientific purposes. It has a thruster configuration that allows motion in surge, heave, yaw as well as sway. The ROV is equipped with navigation sensors, and can also be used with a number of additional sensors, cameras and tools, such as manipulator arms. It can be controlled manually using a PlayStation controller, or from a lab computer, which is a Dell latitude e7440 loaded with Videoray control software. The Videoray ROV was purchased configured with standard communications protocols, sample codes and interfaces. All other code is made by scratch by Bent O. Arnesen, parts of which are documented in Arnesen and Schjølberg (2016). A picture of the Videoray is seen in Figure 5.2.

Figure 5.2: Videoray Pro 4, courtesy of AtlantasMarine

The Videray Pro 4 ROV is equipped with an embedded navigation solution, VectorNav VN-100. This is developed using MEMS-based sensor technology, and combines a set of 3-axis accelerometers, 3-axis gyroscopes, 3-axis magnetometers and a pressure sensor (VectorNav).

5.2.4 SeaBotix LBV600-6 ROV

LBV600-6 is a small work class ROV produced by SeaBotix, seen in Figure 5.3. The SeaBotix can be controlled manually using a dedicated control unit or using control software. It has six thrusters, where 4 of them work in forward direction, giving the ROV 4-axis maneuverability.

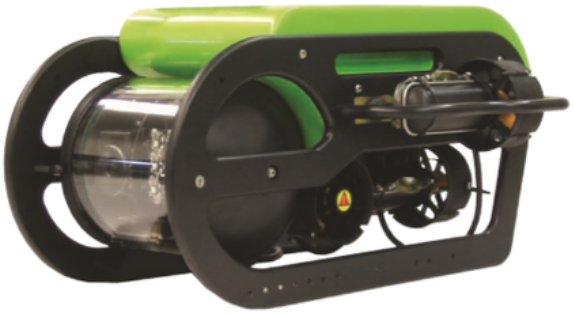

Figure 5.3: SeaBotix LBV600-6, courtesy of BlueSolutions

The SeaBotix used at NTNU is equipped with both a manipulator arm as well as a high-resolution camera that can film during an operation. A MEMS-based IMU is mounted on the top of the SeaBotix, placed inside a cylinder. As for the Videoray, the IMU contains accelerometers, gyroscopes and magnetometers. A pressure sensor is also mounted on the ROV.

5.2.5 Qualisys Motion Tracking system

The QMT system is a tracking system used in the MC-lab to obtain position and orientation fixes. The motion capture technology is based on a set of cameras, used for detecting markers mounted on a body in motion, which also can be used for underwater applications. A minimum of four markers is needed in order to determine the position uniquely.

In the MC-lab at Tyholt 6 high-speed infrared cameras are mounted to function in the test basin. Qualisys will work within an area where these 6 cameras have sufficient coverage. This is decided by the camera configuration, water quality, light and shadowing effects as well as marker configuration. Registrations made by the cameras are transmitted to a computer dedicated to running Qualisys software. Based on camera recognition of the markers under water, triangulation principles are used to determine position and orientation data, which is broadcasted over the wireless network in the MC-lab. The cameras are configured to update measurements at a frequency up to 100-150 Hz.

Qualisys produces orientation estimates for the registered body given in Euler angles. These were converted to quaternions, to fit the formulation of the observers, see Section 4.1. When determining the orientation of the ROV, the system will define a BODY frame for the body that is detected, coinciding with the NED frame defined by Qualisys. It was assumed that $\{b\}$ defined by QMT was coinciding with the actual BODY frame for the ROV.

Because Qualisys position estimates were available and very accurate, these were used as ground truth during all experiments. The derivative of the QMT position measurements were also used as a reference for the linear velocity estimates. Because the position estimates contained noise, these also gave a noisy velocity estimate. The velocity reference was therefore low-pass filtered. This induced some delay to the reference, but provided an estimate good enough for evaluating the velocity estimation errors for the filters.

Constructing range measurements

From the QMT position estimates, pseudo-range measurements were constructed, according to the definition of the geometric range (3.23). Transponder positions also had to be invented, and were fabricated so that they would be realistic considering the dimensions of the test basin.

$$\begin{aligned} \breve{p}_1^n &= [10, -3.25, -0.5]^\top \qquad \breve{p}_2^n = [-10, -1.75, -0.8]^\top \\ \breve{p}_3^n &= [10, 3.35, -0.3]^\top \qquad \breve{p}_4^n = [-10, 1.75, 0]^\top \end{aligned} \tag{5.4}$$

Lever arm compensation

In order to use the QMT system to obtain measurements for the Videoray, a custom made rig had earlier been made in order to mount markers on the ROV. The rig enables markers to be fixed with good spread, in order for the underwater cameras to identify the body from a variety of angles. The marker configuration is shown in Figure 5.4, where the ROV lies upside down to reveal the marker rig and the markers. The QMT will then estimate position and orientation for the geometric center of the markers that are registered. Due to the geometry and the placement of the markers, shadowing of markers and otherwise loss of markers may affect how well Qualisys measures position and orientation of the ROV.

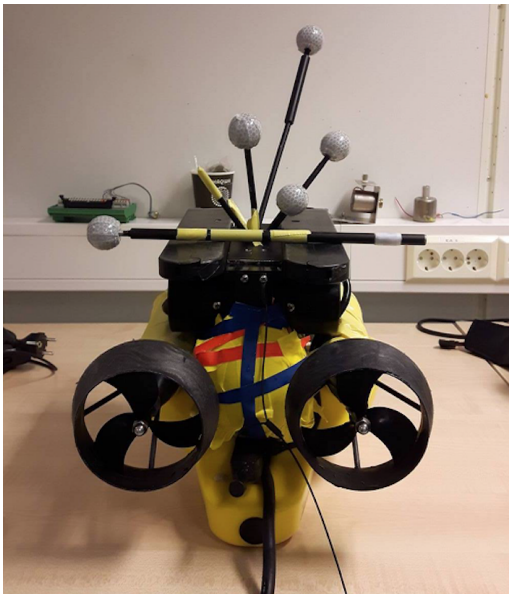

Figure 5.4: Videoray marker configuration

When combining Qualisys measurements with other measurements, it is important that these are made relative to the same point on the ROV. The pseudo-range measurements that were constructed using QMT were found relative to the geometric center of the marker configuration, while acceleration measurements were found relative to the placement of the IMU on the ROV. This meant that the point for which acceleration and the pseudo-range measurements were found were separated by a lever arm. In order to obtain high accuracy, the lever arm should be compensated for. This was done according

to Equation (3.25).

In order to determine the lever arm separating the INS and range measurements obtained for the Videoray, it was assumed that the point measured by the QMT system lied straight under the IMU, so that the lever arm only had a component in Down. The lever arm could then by found using the difference in the measurement in Down from the pressure sensor and the QMT Down measurement.

For the SeaBotix Qualisys markers were mounted on individual rods sticking out from the body, see Figure 5.5, placed in order to lay their geometric center as close as possible to the position of the IMU. The IMU lies inside the cylinder mounted on top of the ROV seen in the picture. Similarly the Water Linked acoustic receiver, used to obtain the TOA measurements, was placed close to the IMU, though not visible in the picture. It is therefore assumed that all measurements are made relative the same point, so no lever-arm compensation is done. This should only yield small inaccuracies for the marker configuration applied in experiments using the SeaBotix.

Figure 5.5: SeaBotix marker configuration

5.2.6 Water Linked acoustic system

Water Linked is an acoustic system based on fixed subsea transponders. TOA measurements are found from acoustic waves signals, and are obtained for underwater vehicles by a receiver mounted on the body. The acoustic set-up follows the principles applied by LBL acoustic positioning as described in Section 2.3, only at a smaller scale.

For the experiments in the test basin, the wave speed was unknown, so that only pseudo-

range measurements were available. Unlike the range measurements generated in experiment I, the frequency of the actual acoustic ranges was more lower and probably also contained more noise.

During experiment II using the Water Linked System, 4 transponders were placed in the test basin in the MC-laboratory. Two of them were mounted on stakes, in order to achieve some variation in the transponder position in Down. In addition each transponder had a Qualisys marker attached, so that the QMT system could be used to determine the transponder positions accurately. During experiments they were as listed below.

$$\begin{aligned} \breve{p}_1^n &= [-2.356, 1.259., -0.757]^\top \qquad \breve{p}_2^n = [2.965, 1.009, -0.148]^\top \\ \breve{p}_3^n &= [2.150, -0.677, -0.769]^\top \qquad \breve{p}_4^n = [-1.642, -1.610, -0.193]^\top \end{aligned} \tag{5.5}$$

5.2.7 Determining measurement noise

Qualisys Motion Tracking System

QMT produces position and orientation measurements with high accuracy. The variances for the noise present in each of the position measurements were found experimentally in work done by Sandøy et al. (2016), and are reproduced in the table below. The variance for each measurement was found by logging a series of measurements at 10 Hz and using MATLAB's *var* function on the resulting time series.

Table 5.1: Qualisys measurement noise variance, courtesy of Sandøy et al. (2016)

Qualisys	Measurement	Variance, σ^2	Unit
Position	x	2.727425e-08	$[m^2]$
	y	2.584928e-08	$[m^2]$
	z	1.987803e-09	$[m^2]$

Because position measurements were used to construct range measurements, the Gaussian distributions for the noise on the position measurements were used to find the Gaussian distribution of the noise on the range measurements. For the experiments performed, Qualisys measurements were generated with a frequency of 100 Hz. The variances of the position measurements were assumed to be the same at 10 Hz and 100 Hz. The method used to find the resulting Gaussian distribution for the noise present in the range measurement is illustrated in Figure 5.6.

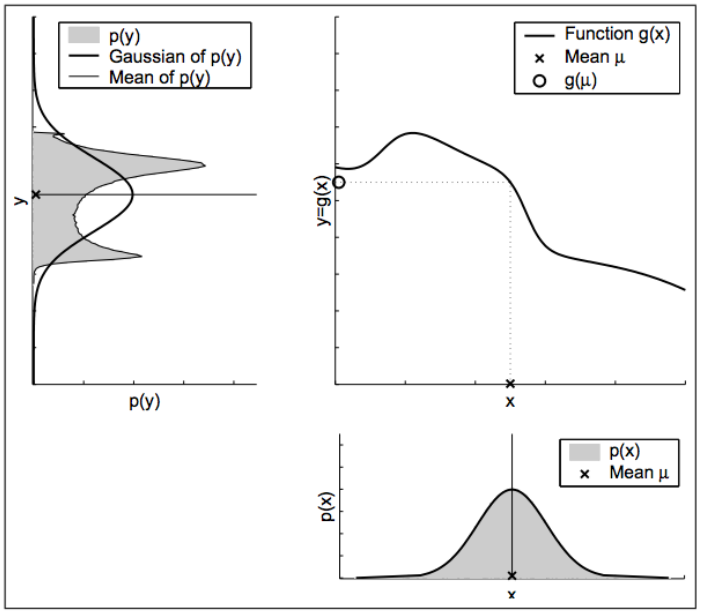

Figure 5.6: Nonlinear transformation of a Gaussian variable, courtesy of Thrun et al. (2005)

The MATLAB function *normrnd* was used to generate noise present in measurements for x, y and z, using their Gaussian distribution, $\varepsilon \sim (0, \sigma^2)$, and the variances defined in Table 5.1. The definition of the geometric range was then used to calculate the noise that would be present in the pseudo-range measurements, when using the Qualisys position measurements to find the constructed range. The function *fitdist* was then employed to define a new Gaussian distribution based on the noise found for the range. The variance of the resulting distribution is given in Table 5.2.

Table 5.2: Range measurements noise variance

Range measurements	Standard deviation, σ	Unit
y_i	1.6376e-04	[m]

Water Linked Acoustic system

The noise present in the Water Linked range measurements was decided based on tuning, which resulted in a standard deviation of $\sigma = 1e - 04$.

5.2.8 Determining process noise

The process noise in the filters is defined by the variance of the wave speed bias, acceleration measurements in addition to the variance for which the acceleration biases vary.

Acceleration measurement noise

For the Videoray the IMU accelerometer noise variance was found by logging 16105 acceleration measurements for the ROV in static condition, at a frequency of 100 Hz. The variance of the acceleration measurements for the ROV at rest should therefore only be because of noise. The measurement variance was found using the in-built function *var* in MATLAB on the resulting acceleration data series. The resulting variances of the noise present in the acceleration in a_x^b, a_y^b and a_z^b are given in Table 5.3.

Table 5.3: IMU accelerometer measurement noise variance

Accelerometers (IMU)	Variance, σ^2	Unit
Noise in a_x^b	1.6765331232158308e-04	$[m/s^2]$
Noise in a_y^b	1.623284546288902e-04	$[m/s^2]$
Noise in a_z^b	3.342784513438293e-04	$[m/s^2]$

The SeaBotix was also equipped with a MEMS-based IMU, and the same variances were used initially for the other experiments. These were later modified during the tuning process of the filters. These and the other sensor specifications used in offline runs with the experimental data, are summarized in Table 7.2 in Chapter 7.

Wave speed and acceleration bias

The variance for which the wave speed bias varied, was found tuning empirically to achieve the best overall performance, and were in offline tests set to $\sigma_\beta^2 = 10^{-6}$ in experiment I and $\sigma_\beta^2 = 10^{-7}$ in experiment II. The variance of the acceleration measurement biases was set to $\sigma_{bacc}^2 = 10^{-8}$ in offline runs of both experiments.

5.2.9 Calibration of acceleration measurements

The calibration process that was performed for the accelerometers mounted on the Videoray estimated scale-factors, the orthogonalization matrix to account for orthogonality misalignment errors in addition to offsets of the accelerometer triad. This was done using a finished calibration script, which is based on a nonlinear optimization algorithm, explained in the work by Rohac et al. (2015). Having defined the Sensor Error Model (SEM) from calibration, the compensated acceleration measurements can be found according to (A.1)

$$u_a = T_a S_a (y_a - b_a) \tag{5.6}$$

where y_a is the vector of measured acceleration, b_a is a vector of offsets, S_a represents the matrix of scale factors, T_a transforms the vector from the non-orthogonal coordinate system to an orthogonal one, all of which were found by the calibration algorithm. This was run for a series of acceleration data collected for approximately 24 different orientations. For each orientation acceleration was measured under static conditions, so that the mean of the measurements for each orientation could be used in order to reduce the effect of random noise. Based on this the vector of compensated acceleration measurements, u_a, was found (Rohac et al., 2015).

The accelerometers for the SeaBotix were not calibrated.

5.2.10 Handling sensor drop-outs

Every once in a while, the QMT system would suffer from drop-outs of measurements. This happens when for some reason not all markers are captured by a sufficient number of cameras. During the experiments using Videoray, Qualisys was used for generating range measurements, and drop-outs of position measurements would also cause drop-outs of range measurements. If the IMU acceleration data had been more accurate, the filter could benefit from just dead reckoning whenever the range measurements for some reason were not available. Because the acceleration data was not that accurate, and because the drop-outs usually only occur for short periods of time, the previous QMT measurements were used to generate ranges, whenever an drop-out occurred.

Drop-outs of QMT also meant that orientation estimates were lost. These were needed in order to transform the acceleration measurements to the inertial frame, whenever new

acceleration measurements were available. This was solved using the previous orientation measurement, until a new one was available.

Chapter 6

Simulation results

The following chapter covers the results from simulations as described in Chapter 5. Simulation analysis is particularly useful as both the actual and the estimated states are known. Therefore the estimation error can be directly observed. In this thesis simulations are used to verify the implementation of the filters, in addition to comparing the performance of the TSF and the EKF. The filters were tested in steady-state and transient behavior. Relevant plots and tables are presented, followed by a short discussion related to these specific results.

6.1 Summary of simulation specifications

Simulations were run for 300 seconds, and the filters were updated at a frequency of 100 Hz. In Table 7.2 the most important sensor specifications are summarized.

Table 6.1: Sensor specifications used in simulations

	Simulations		
	Noise $[\sigma^2]$	Bias	[Hz]
y_i	1e-02	n/a	2
a^b_{imu}	1e-04	$\begin{bmatrix} 0.1 \\ 0.05 \\ -0.13 \end{bmatrix}$ $[m/s^2]$	100

6.2 Simulation I: Steady-state behavior

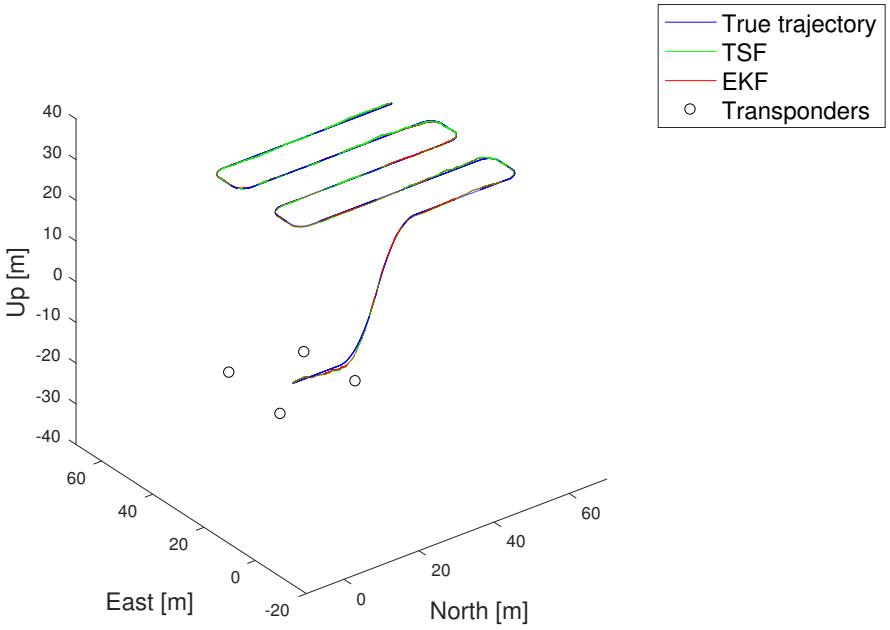

Figure 6.1: Simulation I: Trajectory in 3D

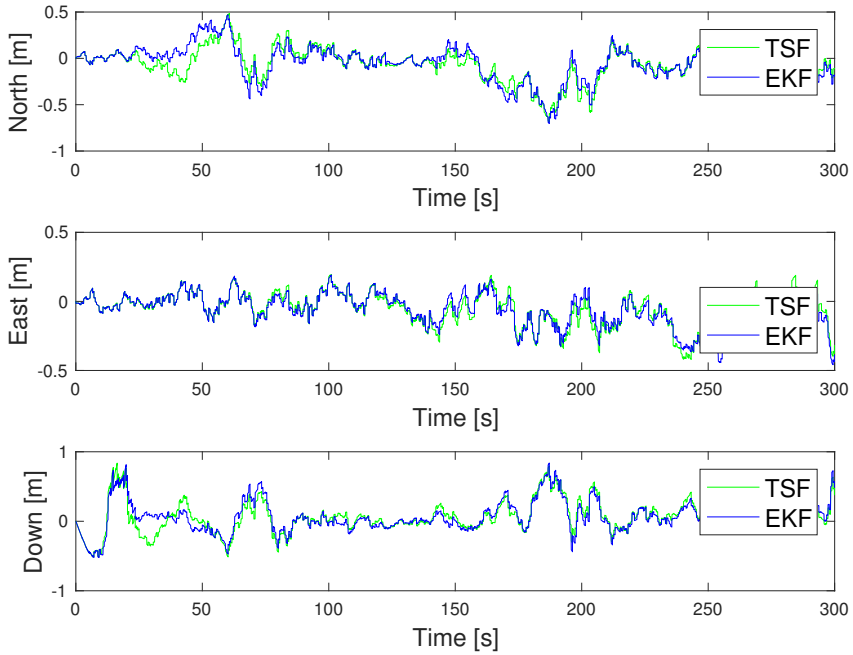

Figure 6.2: Simulation I: Position estimation error

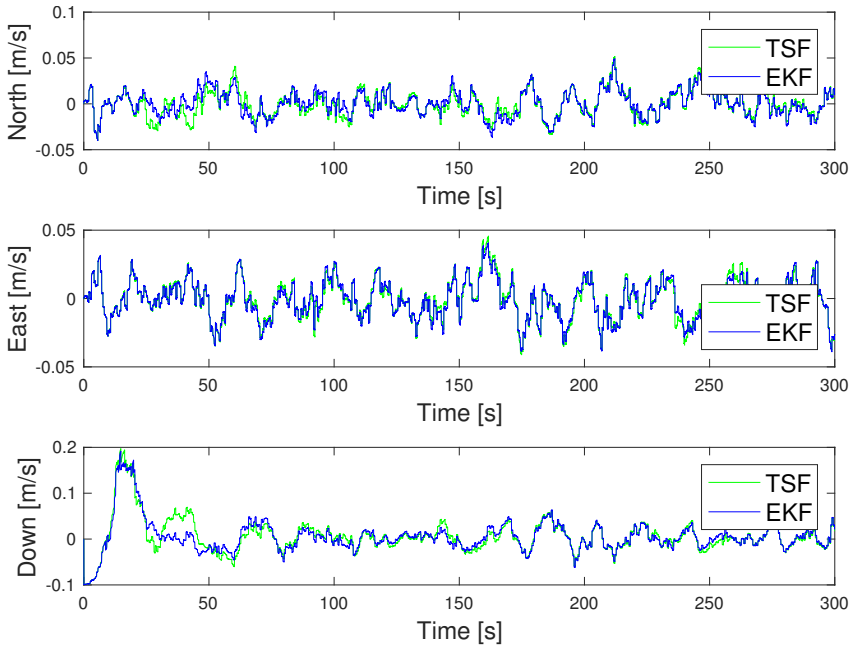

Figure 6.3: Simulation I: Velocity estimation error

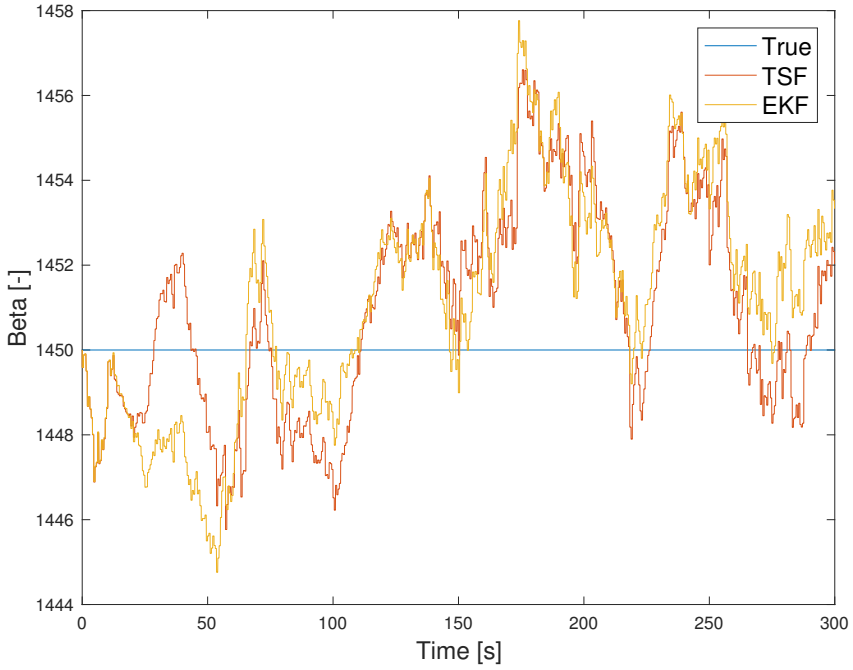

Figure 6.4: Simulation I: Wave speed estimate

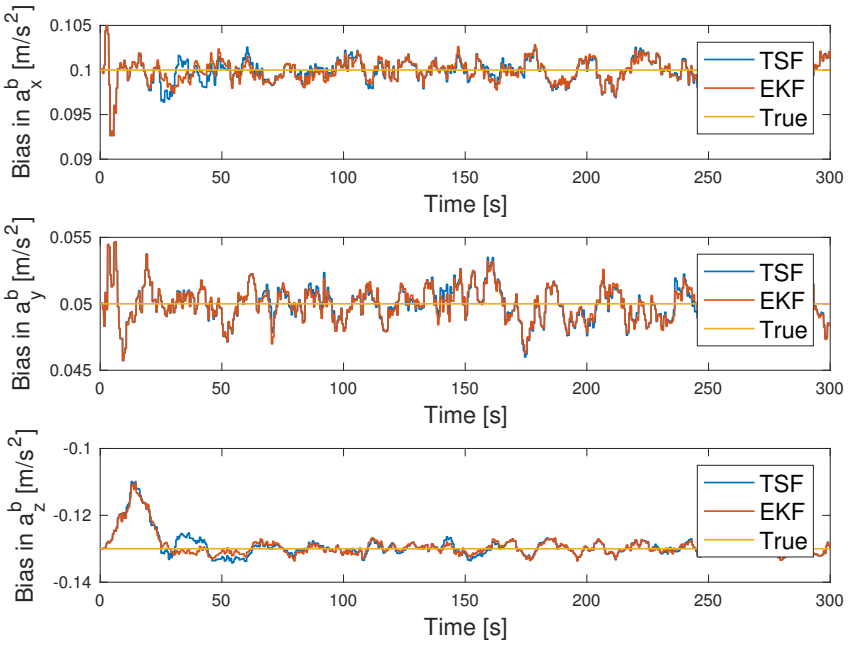

Figure 6.5: Simulation I: Acceleration bias estimates

6.2.1 Analyzing the steps of the TSF

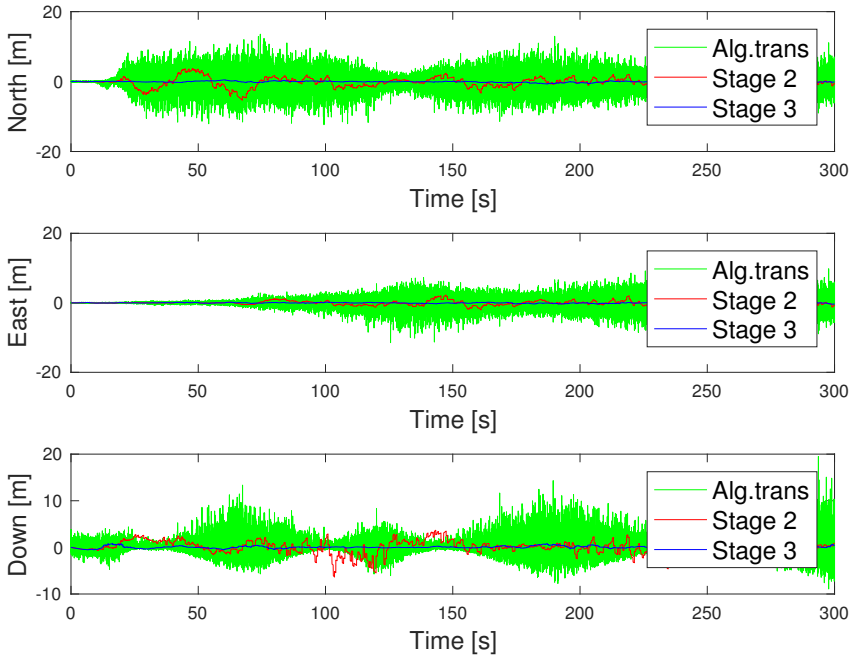

Figure 6.6: Simulation I: Steady-state behavior of second and third stage of the TSF

6.2.2 Resolving the ambiguity between r_1 and r_2

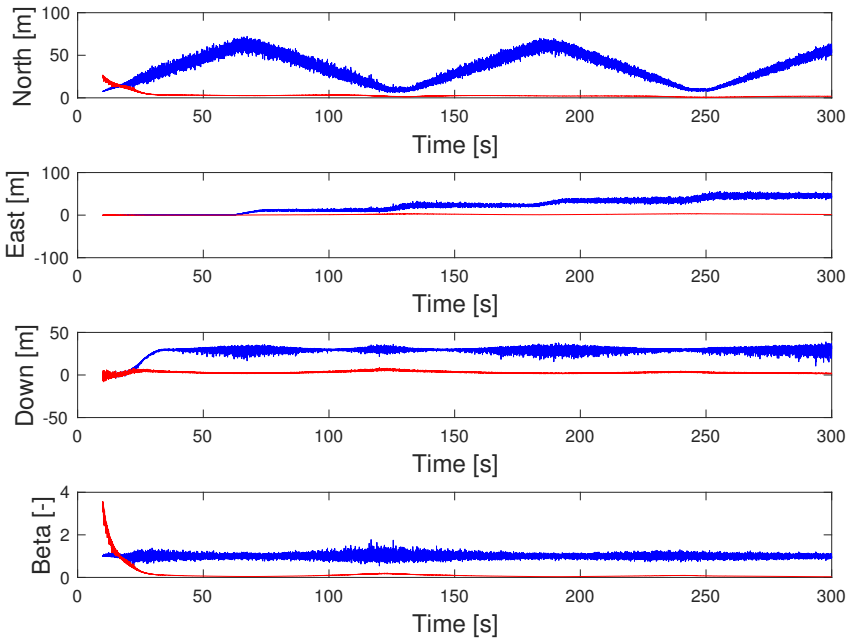

Figure 6.7: Simulation I: Solution to algebraic transformation

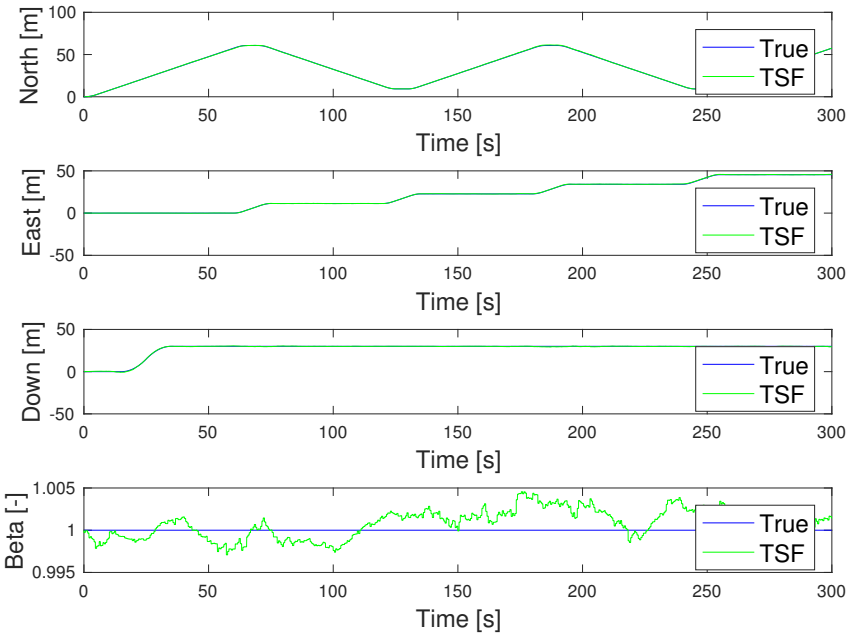

Figure 6.8: Simulation I: Estimated and true position and wave speed bias

In Figure 6.7 the blue graph is the solution to position and β found using the selected solution of r, while the red graph applies to the value of r not selected.

6.3 Simulation II: Transient behavior

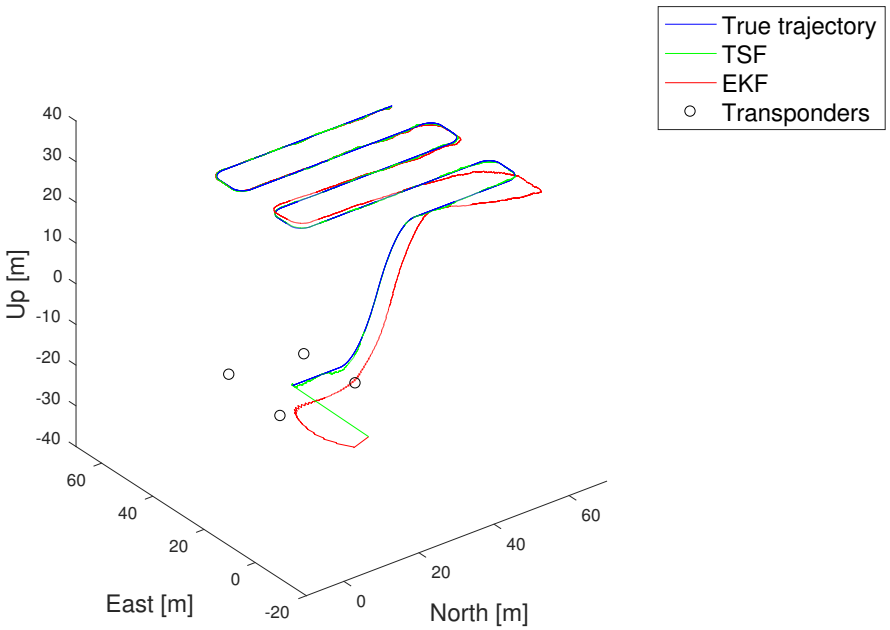

Figure 6.9: Simulation II: Trajectory in 3D

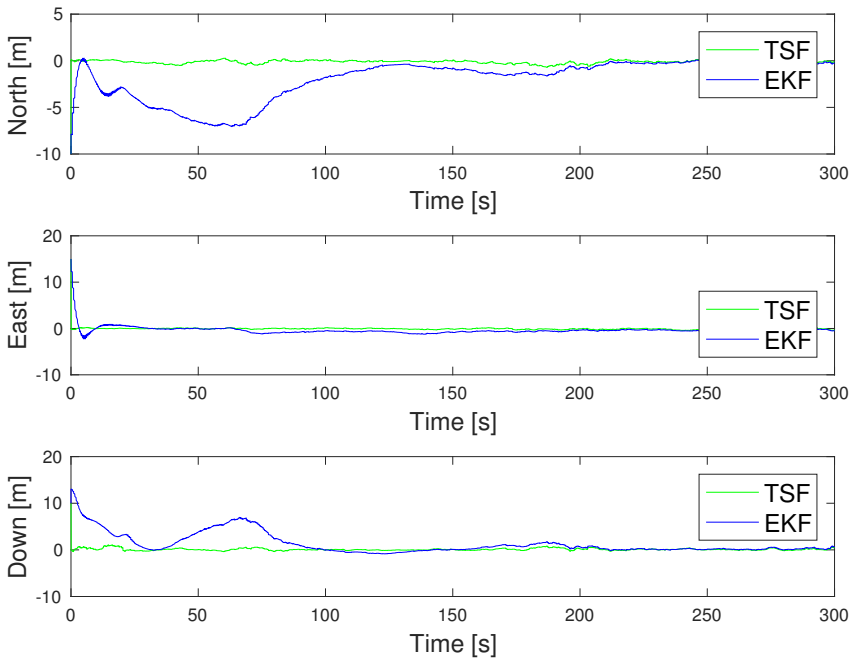

Figure 6.10: Simulation II: Position estimation error

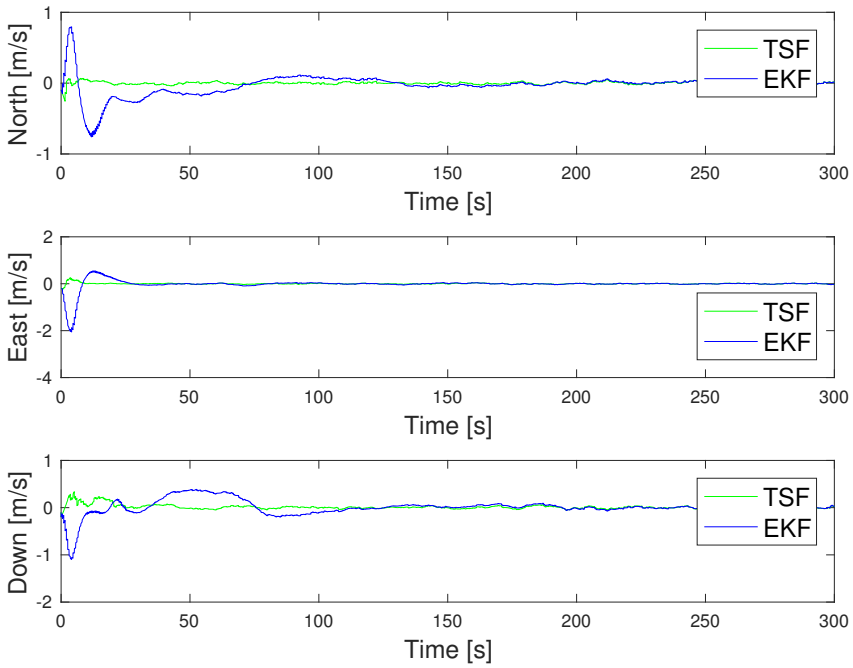

Figure 6.11: Simulation II: Velocity estimation error

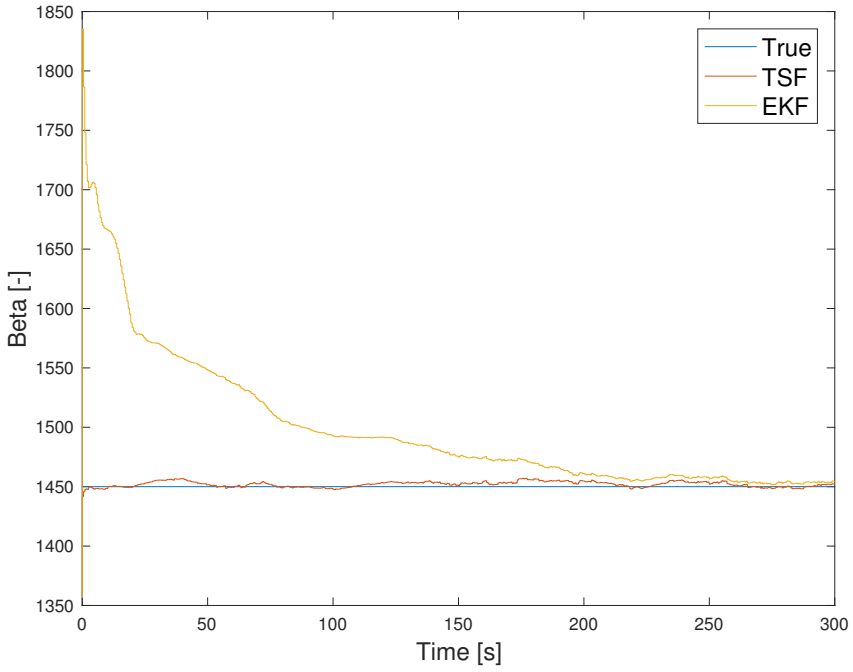

Figure 6.12: Simulation II: Wave speed estimate

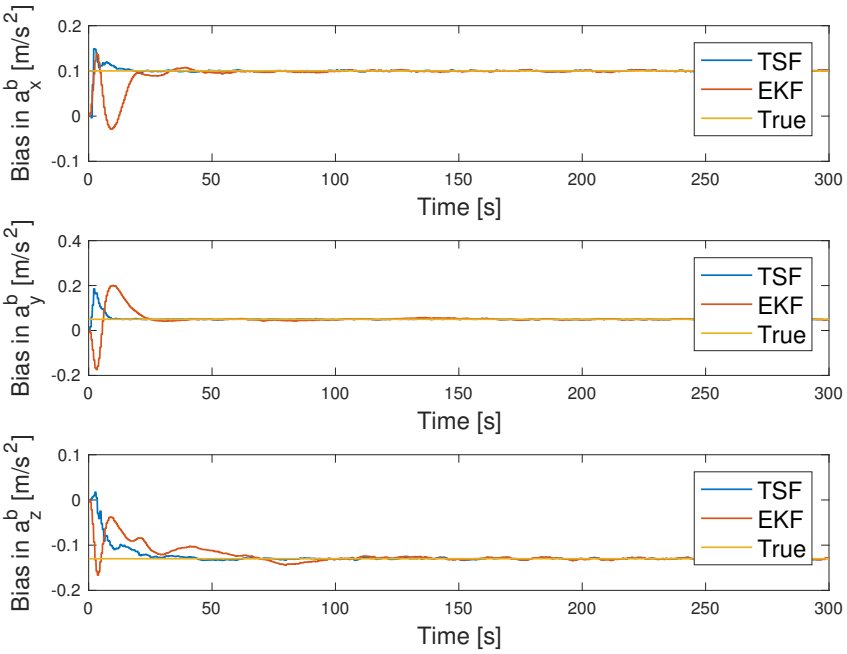

Figure 6.13: Simulation II: Acceleration bias estimates

6.4 RMS in simulations

Table 6.2: Position RMS error in simulations

	Simulation I		**Simulation II**	
	TSF	**EKF**	**TSF**	**EKF**
North [m]	0.1798	0.1892	0.2096	2.8749
East [m]	0.1357	0.1370	0.1661	0.9189
Down [m]	0.2318	0.2328	0.2605	2.5841

6.5 Execution time

Table 6.3: Average execution time per iteration

	TSF	**EKF**
Execution time [ms]	1.3581	0.5343

6.6 Discussion of simulation results

6.6.1 Range navigation solution accuracy

The position estimation error in Down reached its maximum during the first few seconds of the simulation, referring to the initial peak in Figure 6.2. This can be related to range signal geometry. The effect of signal geometry is quantified with the Dilution of Precision (DOP) concept. The position information along a given axis obtained from ranging signals is maximized when the angle between the axis and the line of sight is minimized (Groves, 2008). When the ROV is located right above the area in the middle of the four transponders, the angle between the line of sight and the Down axis is instead large. These range signals will result in poor accuracy in Down. Vertical accuracy is instead optimized when the ROV is located at a higher elevation with respect to the transponders.

The horizontal accuracy is best when the ROV is operating at lower elevations and when the line-of-sight vectors from the ROV to the transponders are evenly distributed. This means that as the ROV moves further away from the transponder set-up the signal geometry becomes worse in North and East. Considering the position estimation errors in Figure 6.2 it is seen that the initial position estimation error in North and East was smaller.

For range-based positioning, moving further away from the transponders will deteriorate the overall position estimation error. This is not easily seen in the resulting position estimation errors, because a number of different influences are present during simulations. It would also become clearer if the ROV were to move even further away from the transponders. This has a pure mathematical explanation, categorized in the form of the condition number of the measurement matrix. Moving further away from the transponders, causes more similar range measurements. This will lead to badly conditioned measurement matrices, meaning high condition numbers, resulting in less accurate estimates. As described in Section 4.6.6, the filter's degree of unobservability will decrease as the condition number of the measurement matrix becomes higher.

6.6.2 Analyzing the steps of the TSF

Estimates of the position and the bias parameter, β, can be found using the algebraic transformation, according to (4.19). In Figure 6.6 the position estimates from the alge-

braic transformation and the 2^{nd} and 3^{rd} stage of the TSF are plotted. The 2^{nd} stage is the estimate from the LTV KF, and the 3^{rd} stage is the estimate from the linearized KF. It is important to stress that the solution to the algebraic transformation is not part of the TSF. The first stage in the filter uses the algebraic transformation to create the LTV measurement model used in the 2^{nd} stage KF, but does not apply the resulting position or β which is plotted in Figure 6.6. This is included in the plot simply to illustrate that the algebraic transformation is influenced by noise, and gives a position estimation error in the order of $\pm 15m$. The second estimate is also sub-optimal with respect to noise. This is because the algebraic transformation used to derive the quasi-linear measurement model cancels out nonlinearities, which will affect the estimation accuracy in presence of measurement noise. Because of the nonlinear transformation, the measurement noise in the pseudo-ranges are amplified linearly with increased pseudo-range (Jørgensen et al., 2016). Noise in the pseudo-range measurements cause a bias in the constructed measurements, that was defined in Equation (4.13). When the noise level increases, and the noise variances are unknown, the bias is hard to compensate for and can reduce performance. The 3^{rd} and final state estimate obtains better accuracy, and reduces the effect of noise which is present in the 2^{nd} estimate.

6.6.3 Resolving the ambiguity between r_1 and r_2

A pre-condition for the TSF to be observable, see Section 4.6, is that the ambiguity between r_1 and r_2 can be solved for $m = 4$ transponders. In this implementation this was solved by selecting the solution to the second order equation, r, that gave a wave speed bias, β, closest to 1, which was used as blueprint for the simulations. However, in presence of measurement noise, and in certain limited areas, depending on the transponder positions, both values of r can give very similar estimated values of β. This means that the correct solution can be hard to determine. In Figure 6.7 the resulting position and wave speed bias, β, from the algebraic transformation, is plotted for each of the solutions of r. And in Figure 6.8 the true and estimated position and β are plotted. The result obtained for the selected r, matches the true position and β. This is an indication that the correct solution of r was selected, for the simulations that were run. However, in general this is not a guarantee, and may vary with the amount of noise in the pseudo-range measurements and for certain areas around the transponders.

6.6.4 Execution time

It was found in simulations that it took more than twice as long to calculate the estimate produced by the TSF, compared to the EKF, based on the average execution time per iteration, see Table 6.3. This makes sense as the TSF in theory uses two KF's, while the EKF uses only one. Higher execution time in simulations is an indication that more computer power will be needed to apply the TSF. The state estimates will also be updated slightly faster when using the EKF. Nonetheless, the efficiency will also depend on how the filters are implemented and the operating system.

Chapter 7

Experimental results

Chapter 7 includes the experimental results for the integration filters. Experimental work is a useful method to verify simulations in addition to pointing out some of the practical considerations and challenges that usually present themselves in real-life experiments.

The experimental results that are presented proceed from offline runs, based on sensor data logged during experiment I and II, as explained in Chapter 5. The filters were tested and compared in steady-state as well as transient behavior. A short discussion specific for each of the experiments is included after the results. The final discussion considers the results as a whole, and is given in Chapter 8.

7.1 Summary of experiment specifications

In Table 7.1 the most important specifications for experiment I and II are listed, in order to give the reader a better overview and understanding of how the experiments were executed.

Table 7.1: Experiment specifications

	Experiment I	**Experiment II**
ROV	Videoray	SeaBotix
Range measurements	Qualisys	Water Linked
Acceleration measurements	IMU (MEMS-based)	IMU (MEMS-based)
Length of data series $[s]$	60	≈ 200

Table 7.2 lists the sensors specifications that applied under each of the experiments.

These were slightly different, as different sensors were used for both acceleration and range measurements.

Table 7.2: Sensor specifications during experiments

	Experiment I			**Experiment II**		
	Noise $[\sigma^2]$	Bias	[Hz]	Noise $[\sigma^2]$	Bias	[Hz]
y_i	2.68e-08	n/a	2	10e-04	n/a	≈ 0.8
a^b_{imu}	$\begin{bmatrix} 1.68e-04 \\ 1.62e-04 \\ 3.34e-04 \end{bmatrix}$ $[m/s^2]$	$\begin{bmatrix} 0.01 \\ -0.3 \\ 0.5 \end{bmatrix}$ $[m/s^2]$	100	$\begin{bmatrix} 1e-02 \\ 1e-02 \\ 51e-01 \end{bmatrix}$ $[m/s^2]$	n/a	≈ 100

In Table 7.2 the bias is stated as n/a if it is either not available, as for the IMU accelerometers in the second experiment, or not applicable, as for the range measurements. The filters were run slightly faster than the IMU measurements were available, at approximately 100 Hz. For the final process and sensor covariances, in addition to the initial covariance, P(0), for the filters, the reader is referred to the Attachments. The folder including the implementation of the filters used in offline runs is specified in B.3.

During experiment I Qualisys position and orientation was logged with a frequency of 100 Hz. In experiment II Qualisys was logged with approximately 5 Hz. The velocity reference was in both experiments found from low-pass filtering the derivative of the Qualisys position estimates. The velocity reference contained more spikes in experiment II, because position was updated less often.

Because the data series in experiment II were longer, only the first 10 seconds of the transient behavior was plotted, to make it easier to distinguish between the estimates produced by the different filters. The estimates would eventually converge, and obtain steady-state behavior, which is also plotted for the entire data series.

7.2 Experiment I: Results using Videoray

7.2.1 Steady-state behavior

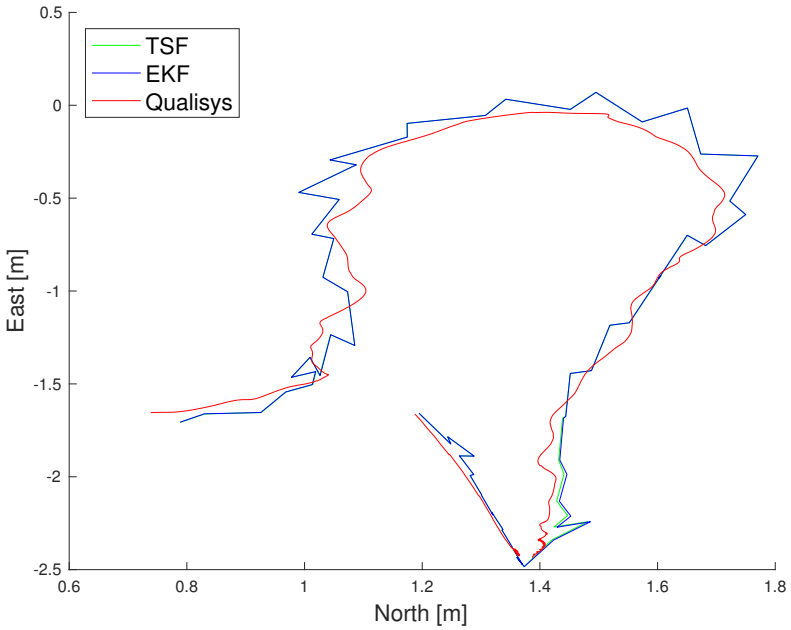

Figure 7.1: Experiment I: Trajectory in 2D

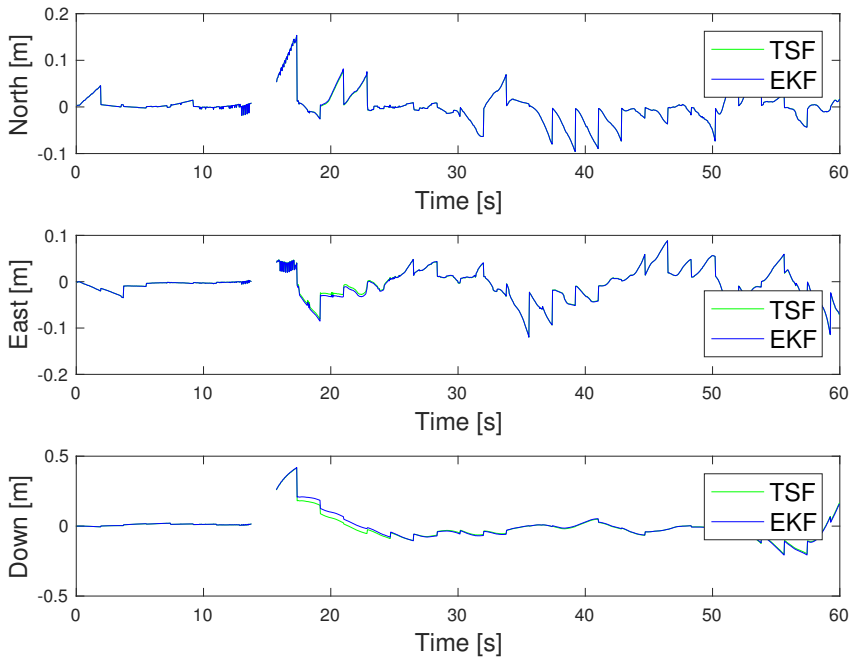

Figure 7.2: Experiment I: Position estimation error

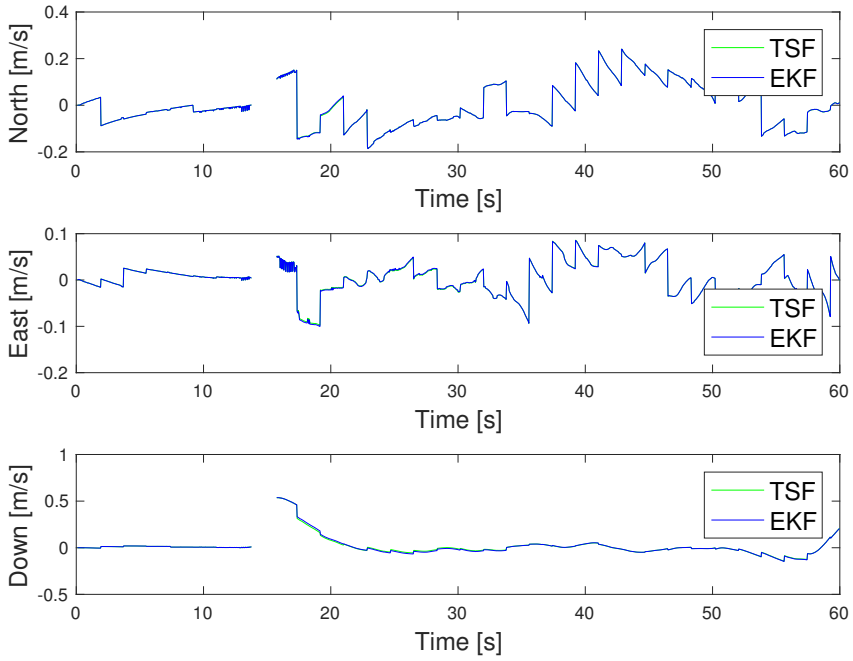

Figure 7.3: Experiment I: Velocity estimation error

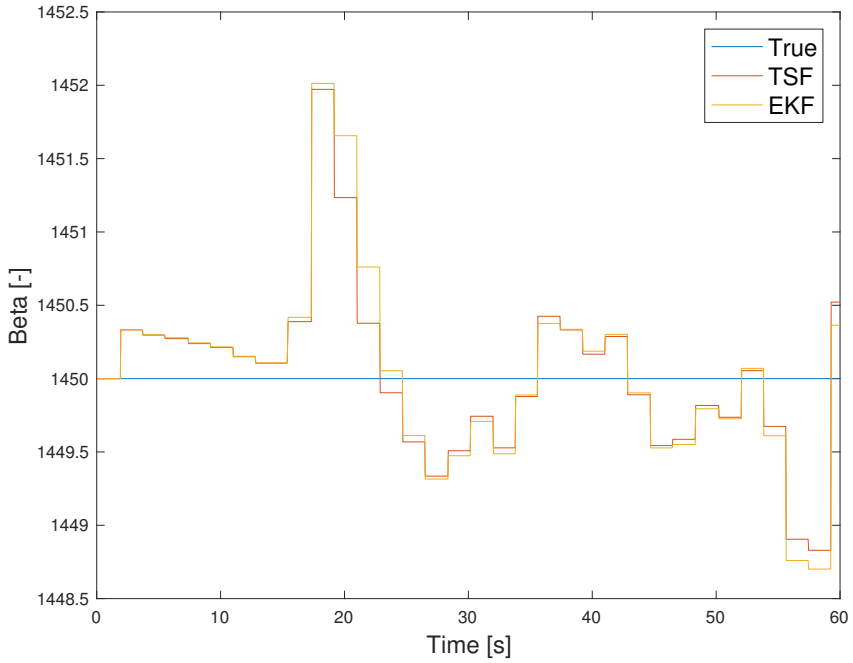

Figure 7.4: Experiment I: Wave speed estimate

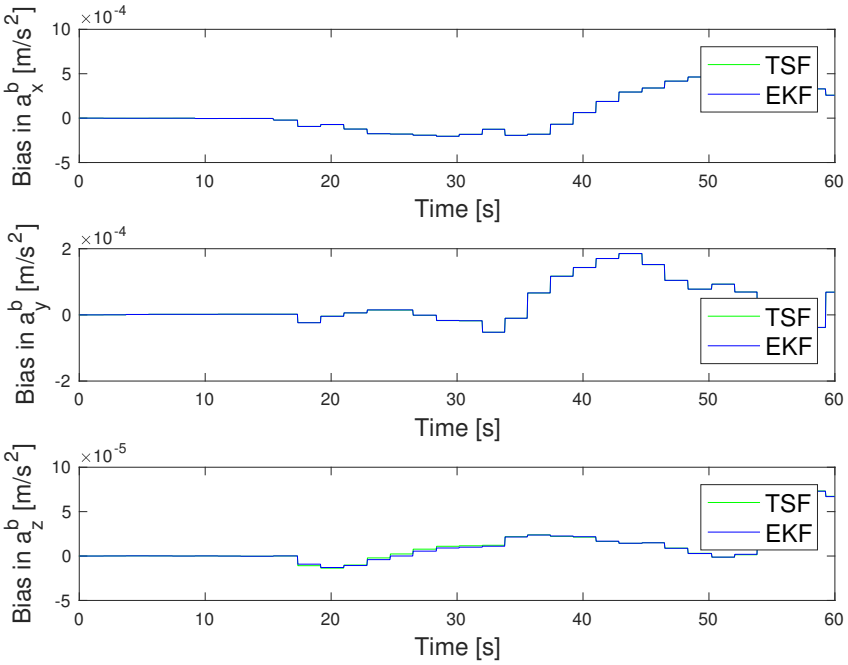

Figure 7.5: Experiment I: Acceleration bias estimates

7.2.2 Transient behavior

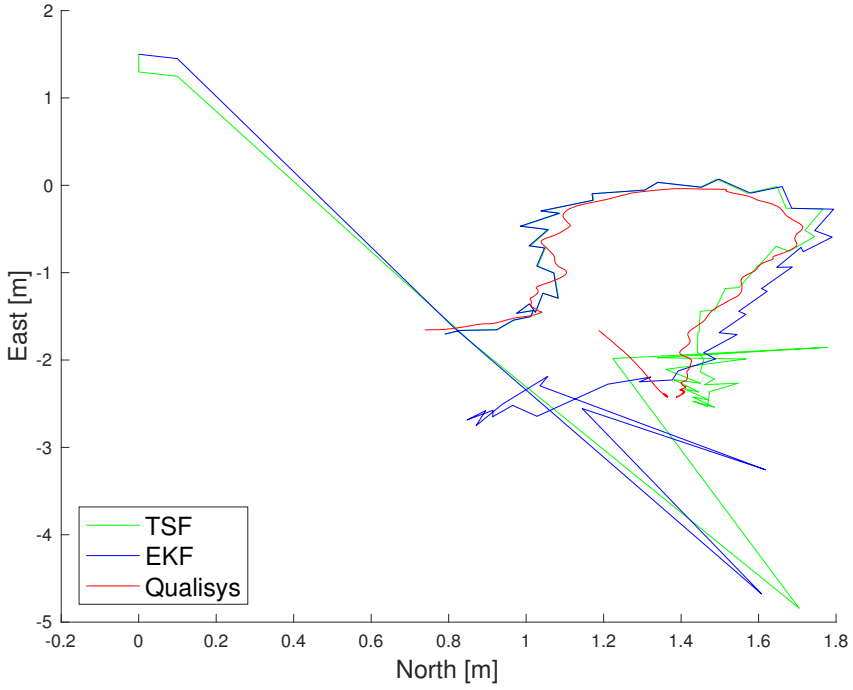

Figure 7.6: Experiment I: Trajectory in 2D

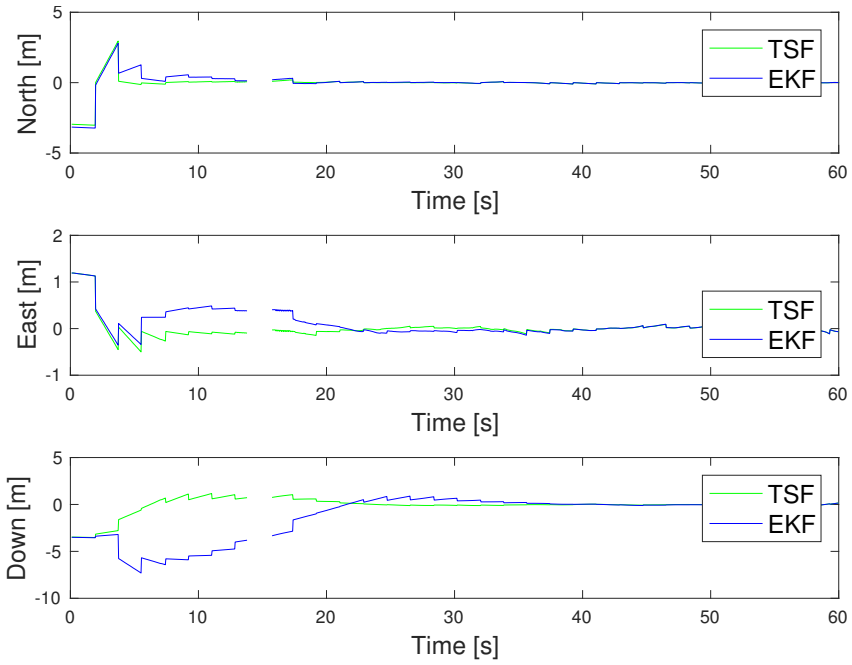

Figure 7.7: Experiment I: Position estimation error

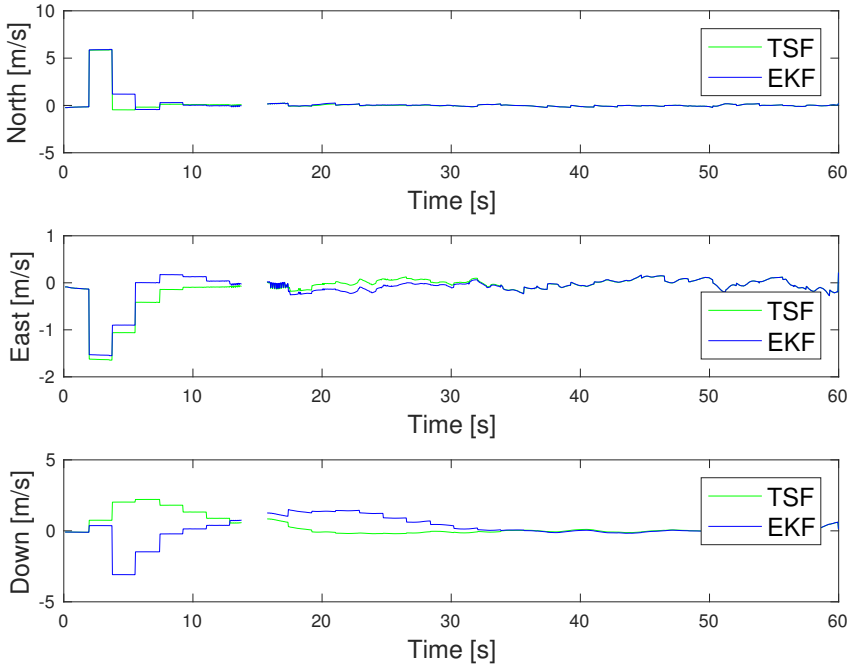

Figure 7.8: Experiment I: Velocity estimation error

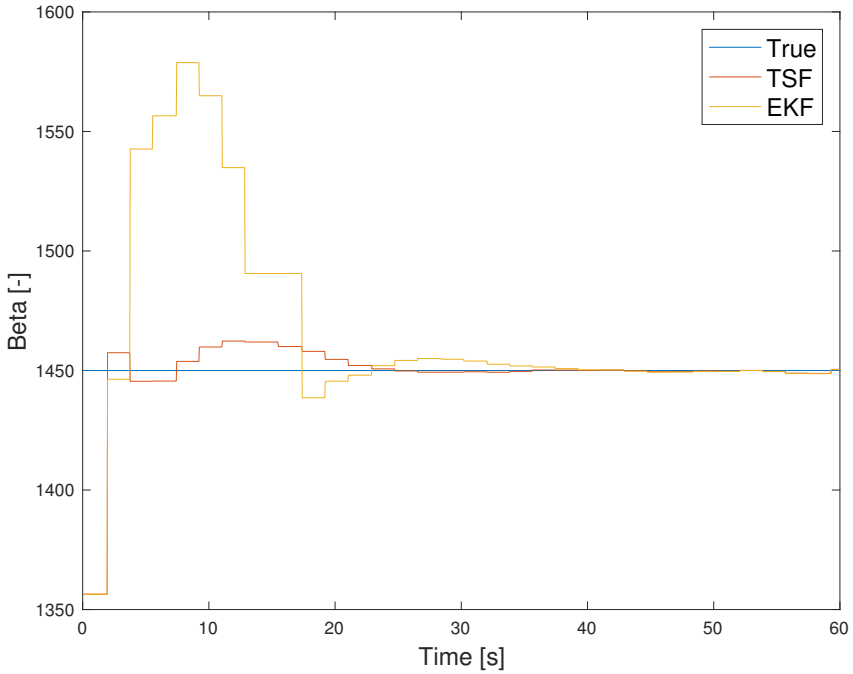

Figure 7.9: Experiment I: Wave speed estimate

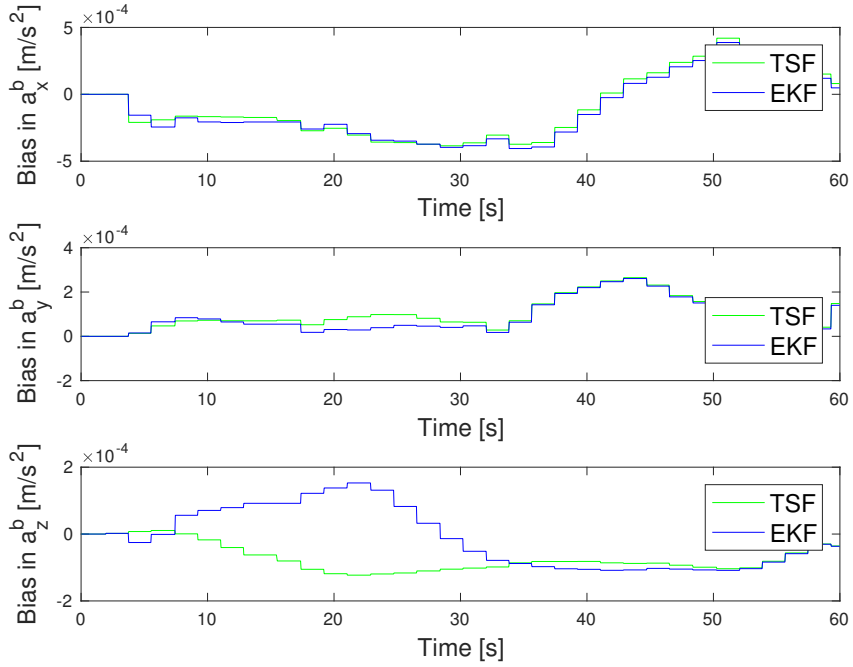

Figure 7.10: Experiment I: Acceleration bias estimates

7.2.3 Discussion of results obtained using Videoray

Considering the position estimation error in North and East in Figure 7.2, this is rather choppy. This suggests that the dead-reckoning performance in between range updates was not very good. The acceleration measurements were calibrated in order to compensate

for scale-factors, orthogonality and offsets. In addition the filters estimated the biases that possibly remained after calibration. However, misalignment errors were not as well catered for. The INS-strapdown assumption implies that the IMU sensor-axes are aligned with the ROV BODY-axes. The QMT system was used to obtain orientation estimates, which were made relative to a BODY frame defined for the detected body by the Qualisys system. It was assumed that this was also coinciding with the true BODY frame of the Videoray. Both assumptions could have been be the source of misalignment errors that influenced the dead-reckoning performance, because the acceleration measurements were not rotated accurately.

Because the accelerometers used in this experiment were calibrated for constant offsets, the estimated acceleration biases obtained small values, see Figure 7.5. In transient behavior, see Figure 7.10, the bias estimates behaved quite similarly.

As earlier mentioned, the QMT system suffered from occasional drop-outs of measurements. This can be caused by the ROV moving outside the area where a sufficient number of cameras are able to detect a body, or for other reasons that the markers are not spotted by the cameras so that the body cannot be positioned. In this experiment this also caused drop-outs of range measurements and orientation estimates. And because of these drop-outs spikes are seen in the plotted position and velocity estimation errors in Figure 7.2 and Figure 7.3. This also caused gaps in the same figures, because no reference was available for evaluating the estimation error.

The wave speed estimate in steady-state is plotted in Figure 7.4. Because the range measurements in experiment I were constructed, the true wave speed was known, and $\beta = 1$ was used to generate pseudo-range measurements. The wave speed estimate oscillated with small amplitude, quite similar as in simulations, see Figure 6.4.

7.3 Experiment II: Results using Seabotix

7.3.1 Steady-state behavior

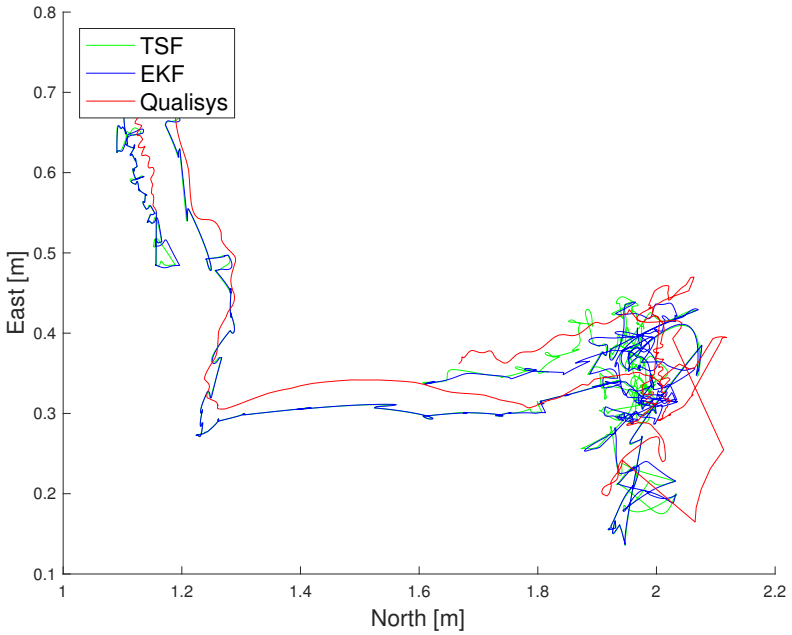

Figure 7.11: Experiment II: Trajectory in 2D

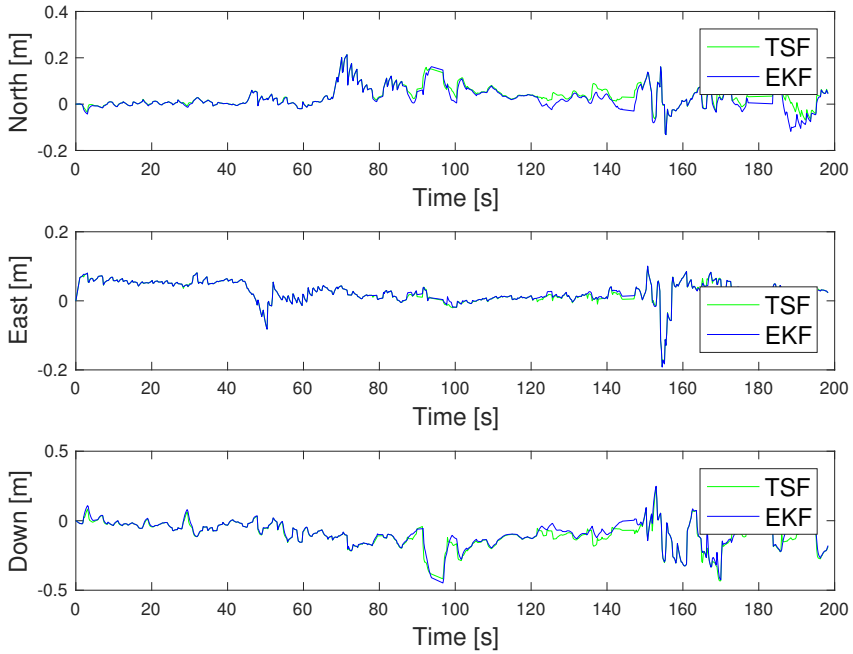

Figure 7.12: Experiment II: Position estimation error

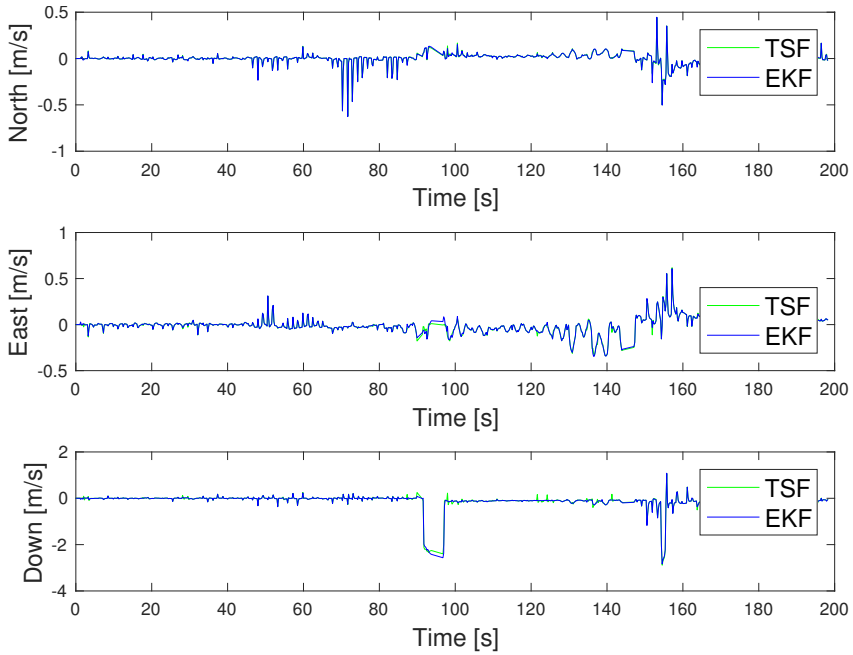

Figure 7.13: Experiment II: Velocity estimation error

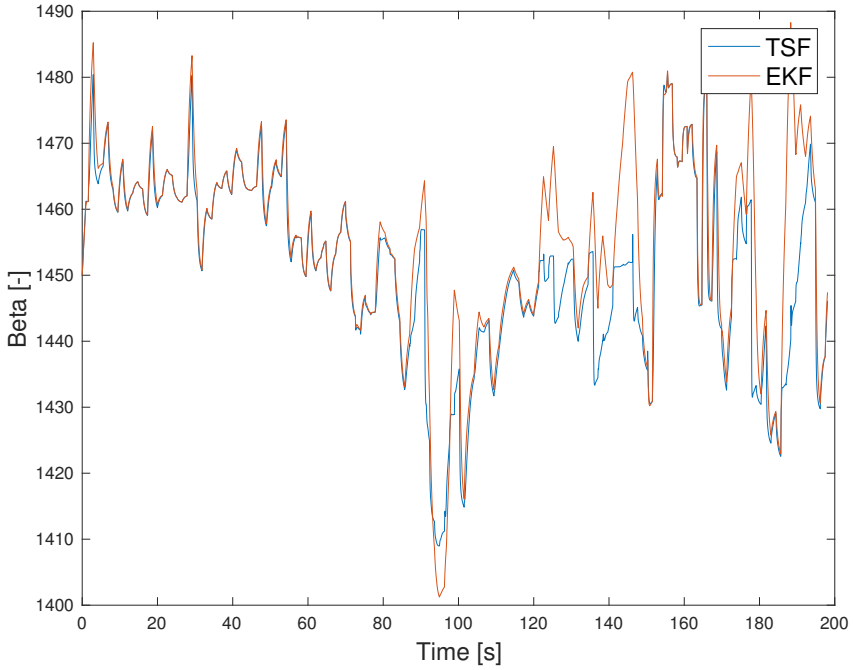

Figure 7.14: Experiment II: Wave speed estimate

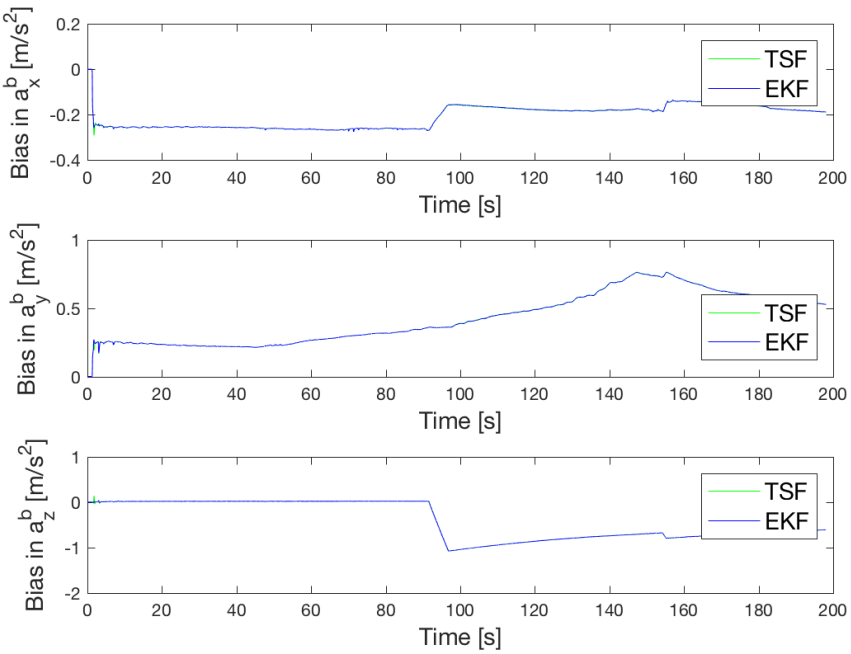

Figure 7.15: Experiment II: Acceleration bias estimates

7.3.2 Transient behavior

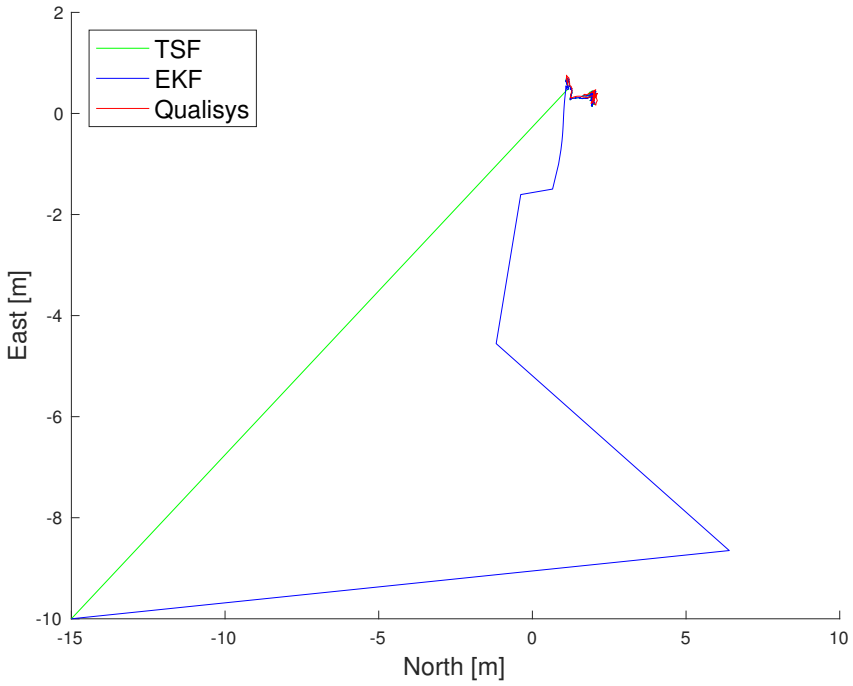

Figure 7.16: Experiment II: Trajectory in 2D

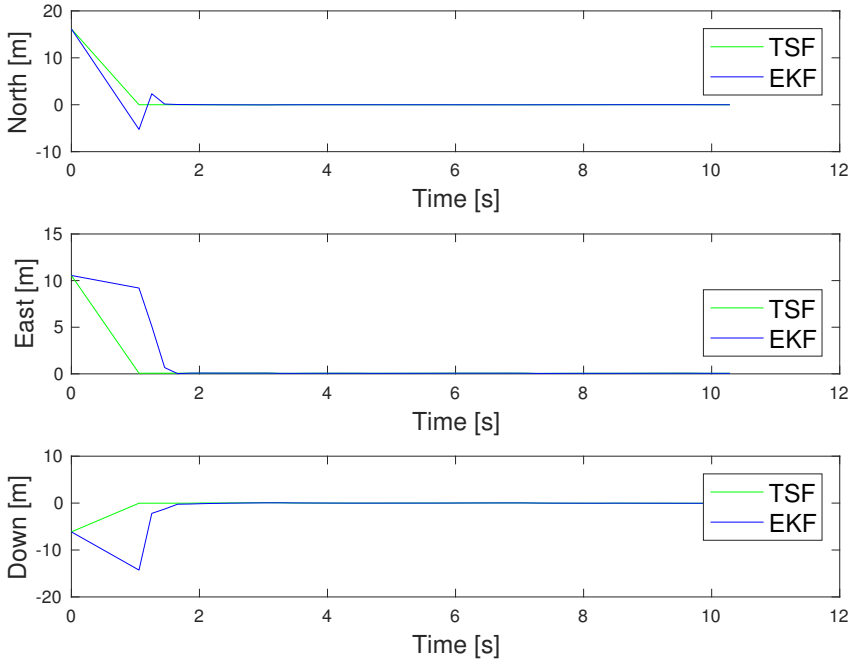

Figure 7.17: Experiment II: Position estimation error

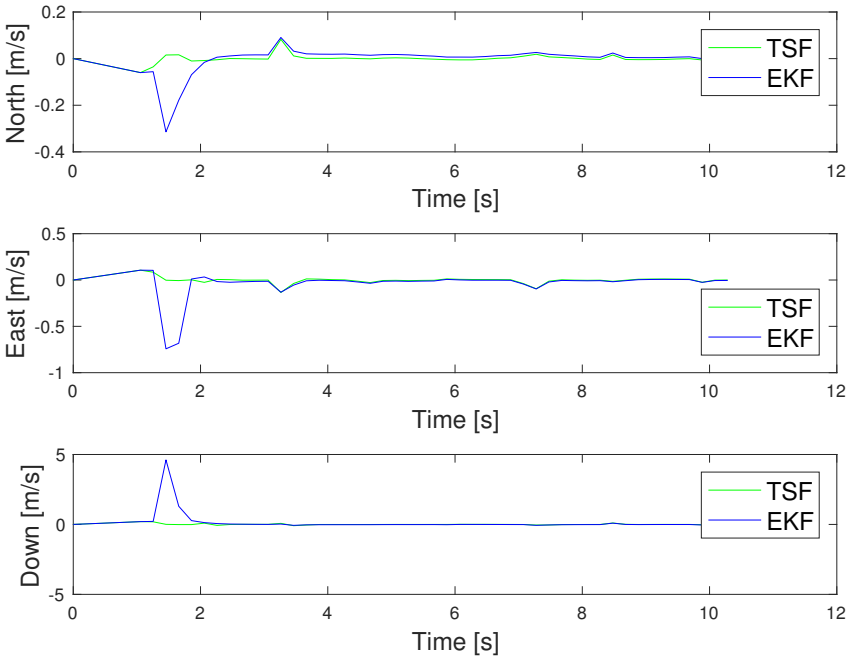

Figure 7.18: Experiment II: Velocity estimation error

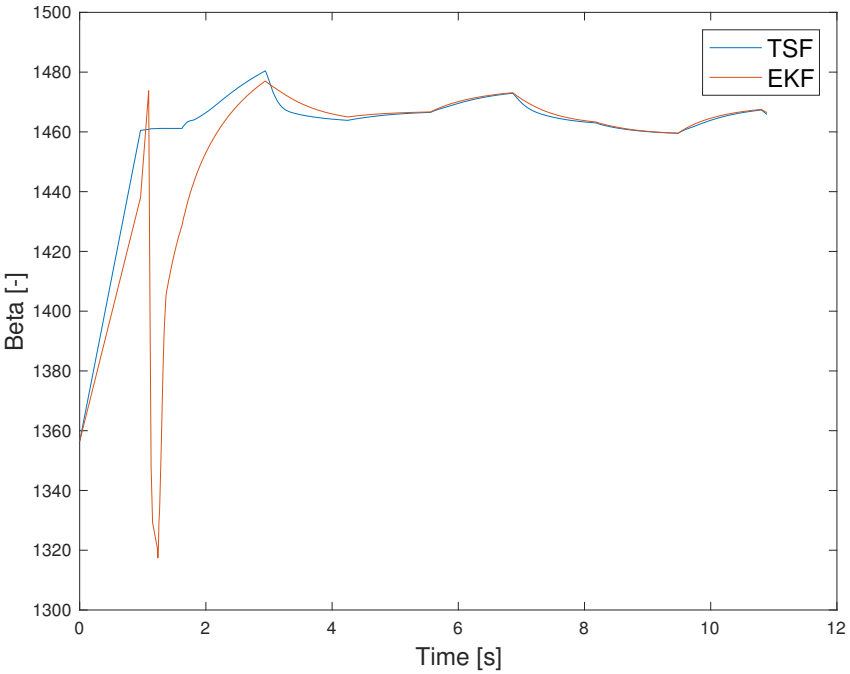

Figure 7.19: Experiment II: Wave speed estimate

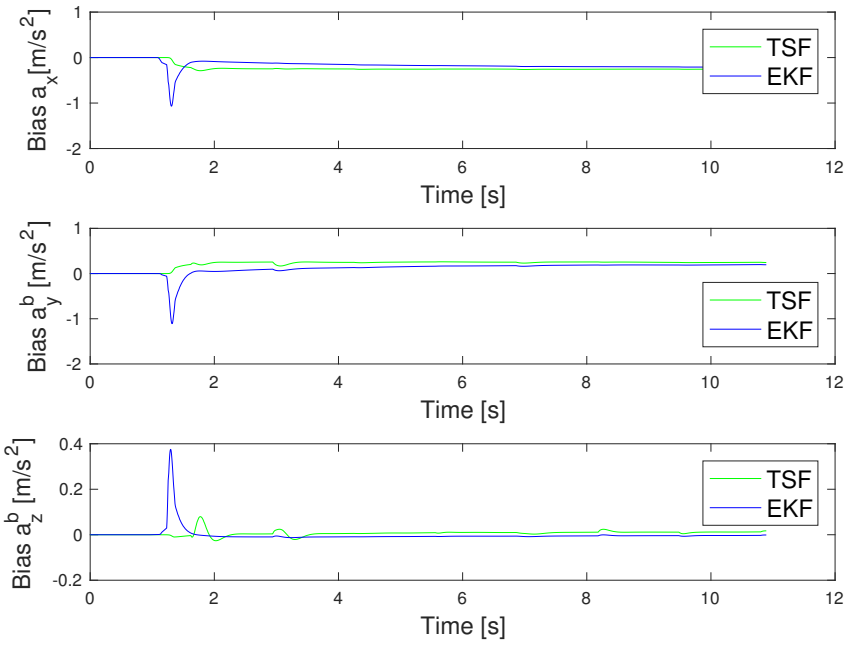

Figure 7.20: Experiment II: Acceleration bias estimates

7.3.3 Discussion of results obtained using Seabotix

Figure 7.11 shows that the estimated 2D trajectory for both filters were quite similar. This is also seen for the position estimation error, in Figure 7.12. In the same plot, a small bump in the Down position estimation occurs at $t \approx 91\,s$, and bumps are also seen in the position estimation error in North and East at $t = 153\,s$. The same disorders are recognized in the plotted velocity estimation errors in Figure 7.13. This was investigated further, and it was found that this was caused by very sudden, large changes in the attitude of the ROV during the experiment. This is clearly seen in Figure 7.21 for the same points of time as the distortions in the estimates. Figure 7.21 shows the orientation estimated by Qualisys, and is here plotted in Euler angles, for better intuition. Because the attitude was updated using only 5 Hz, a fast maneuver will have seemed very sudden. And because attitude updates were also much slower than the states in the filters were estimated, the use of an "old attitude" estimate has caused some error to persist for a couple of seconds. An erroneous attitude will result in a poor gravity compensation, which will give inaccurate velocity and position estimates when the acceleration measurements are integrated.

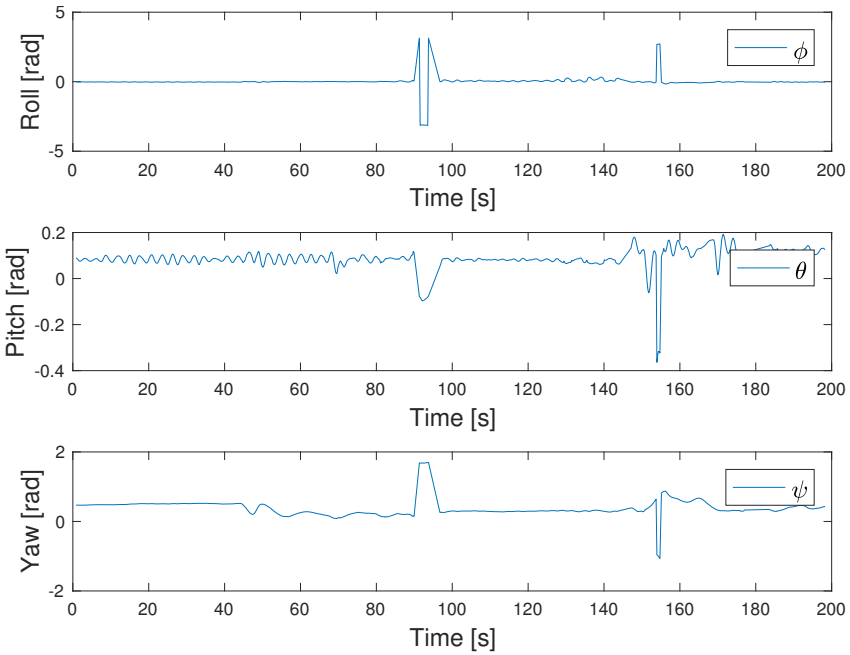

Figure 7.21: Experiment II: Attitude estimates

The sudden jumps in the attitude reference, also caused errors in the acceleration bias estimates in a_x^b and a_z^b. Simultaneously with the attitude jumps, the estimated biases experience sudden breaks, see Figure 7.15. Without the sudden changes in attitude, the bias estimates would have been expected to give smoother estimates.

The estimate of the wave speed bias oscillated with larger amplitude than in the other results, see Figure 7.14. When using the Water Linked acoustic system, the exact wave speed was not known. The wave speed was in this experiment affected by the properties of the water in the test basin. The wave speed estimate seems to converge to a value of approximately $\approx 1450\, m/s$. A theory is that the acoustic measurements were reflected by the concrete walls in the test basin, contributing to increased acoustic noise in the measurements. In turn, this could cause the wave speed estimate to oscillate with large amplitudes. Thruster noise on the ROV could also have contributed to increased acoustic noise.

In realistic field trials reflections can also occur if the acoustic signal bounces off a subsea structure, seabed riser, ship hull or the sea surface. However reflections are considered to be a bigger challenge in the test basin, because the operation site is very confined. The acoustic noise can also increase as a result the wave speed changing with salinity, pressure and temperature. The latter effects are assumed compensated for by estimating the wave speed in the filters.

Considering the 2D trajectory, the position estimation error and all other plotted states,

see Figure 7.16, 7.17, 7.18, 7.19 and 7.20 respectively, it is seen that the TSF estimates converged faster and with smaller overshoots than the EKF in transient phase. In the same figures it also appears that the transient behavior was slightly delayed, because the initial peaks do not appear before after approximately 1 second. This is because the first IMU acceleration measurements were not received before t = 0.96 seconds, and the filters were not updated before after this.

7.4 RMS in experiments

Table 7.3: Position RMS error in experiments

	Experiment I				**Experiment II**			
	Steady		**Transient**		**Steady**		**Transient**	
	TSF	**EKF**	**TSF**	**EKF**	**TSF**	**EKF**	**TSF**	**EKF**
North [m]	0.0325	0.0327	0.6137	0.6692	0.0542	0.0523	0.5375	0.5699
East [m]	0.0323	0.0328	0.2242	0.2715	0.0395	0.0398	0.3514	0.4953
Down [m]	0.0859	0.0898	0.9033	2.5767	0.1365	0.1273	0.2445	0.5364

Chapter 8

Discussion of results

In this chapter some general remarks regarding the results presented in Chapter 6 and 7 are made. The simulation preconditions and the circumstances, for which the physical experiments were conducted, were quite different. For example the set-up of transponders and the trajectory for which the ROV moved were not the same. In simulations noise and biases were perfectly modeled, while in real-life experiments these had to be tuned, calibrated or estimated.

Despite this, an attempt is made to compare the results obtained in simulations with the experimental results. However, the comparison is limited to evaluating only general trends. A broader discussion on integration of inertial and pseudo-range measurements is also included in this chapter.

8.1 Comparing simulation and experimental results

In order to compare the performance of the filters, the RMS error is evaluated in simulations and in experiments. These are stated in Table 6.2 and 7.3 respectively. During experiments, the position measurement from Qualisys was used as ground truth, and used to calculate the RMS error. Based on the resulting RMS error, in addition to the plots included in Chapter 6 and 7, the following general trends are pointed out.

- The TSF and EKF performed similarly in steady-state behavior
- The RMS error was always largest in Down
- The TSF state estimates converged faster than the EKF in transient behavior

- As a result of the previously mentioned point, the RMS error was also smaller for the TSF in transient behavior

8.1.1 Steady-state behavior

The steady-state trajectory plots from simulation and experiment, see Figure 6.1, 7.1 and 7.11, show that the filters perform very similarly in steady-state. This is also confirmed by the calculated RMS position estimation errors.

The steady-state behavior of both filters in experiment I and II obtained a position estimation error that was in fact smaller than in simulations, see Table 6.2 and 7.3. This is most likely due to poorer ranging signal geometry in simulations. As earlier discussed, this gradually became worse as the ROV moved horizontally further away from the transponders. While during experiments, the ROV operated more in the area in the middle of the transponders. Also, the range measurements that were generated in experiment I, contained less noise than those generated in simulations.

It was found in both simulations and in experimental results, that the position estimation errors were always largest in Down. This was expected because the transponders have smallest separation this direction, and because the body is placed sub-optimal with respect to the vertical DOP, as discussed in Section 6.6.

In Figure 6.3, 7.3 and 7.13 the steady-state velocity estimation errors are plotted. For the experimental results, the Qualisys position derivative is used as reference for the linear velocity. This provided noisy references, especially for experiment II, because Qualisys was logged with only 5 Hz. It was found that the velocity estimation errors in contrast to the position estimation errors were larger than in simulations. This suggests that the acceleration measurements were less accurate than in simulations. This is not surprising, considering that the real-life error sources in the IMU acceleration measurements were not known exactly, and the acceleration measurements were integrated to obtain the velocity estimates.

Overall, the position estimation accuracy was best in experiment I. To the extent that the simulation and experimental results can be directly compared, it appears that the TSF showed better performance when range-measurements were subject to less noise. This is supported by the fact that pseudo-range measurement noise is amplified in the first stage of the TSF. The results also emphasized the importance of ranging signal geometry for the position estimation accuracy.

8.1.2 Transient behavior

The transient trajectories, plotted in Figure 6.9,7.6 and 7.16 from simulations and experiments, illustrate how the TSF estimates converged quicker to the correct position. This also resulted in a smaller RMS position estimation error for the TSF, as the initial error was removed faster.

Considering the transient behavior of the velocity estimates in simulations and in experiment II, Figure 6.11 and Figure 7.18 respectively, the EKF has a larger overshoot and converges slower than the TSF. The transient estimates for experiment I, see Figure 7.8 both filters obtain quite large initial values, before they converge. This could possibly have been improved with more extensive tuning.

When the filters were tested in transient behavior, the TSF was usually not re-tuned, while the EKF required additional tuning of the initial covariance P(0). The initial covariance used in the EKF had to be smaller, which means more unrealistic, than P(0) used in the TSF. In general the performance of the EKF is very dependent on tuning of the initial covariance, P(0), and process noise, Q. The feedback loop and the unnecessary P(0) will have slowed down the convergence rate of the EKF, while the initialization provided by the LTV KF and the algebraic transformation ensured fast convergence of the TSF (Jørgensen et al., 2016).

8.2 Dead-reckoning performance

In all realistic acoustic set-ups, range measurements will only be available at slow update rates. This means that in between measurements, navigation must rely on dead reckoning. The dead reckoning performance was for these specific filters decided by the quality of the acceleration measurements in addition to the accuracy of the attitude estimates used for rotating the acceleration measurements.

MEMS-based accelerometers are improving, but are known to contain a considerable amount of noise. Noise levels will typically be measured for the ROV at rest. While during experiments these can increase because of vibrations caused by the thrusters. The applied noise characteristic will in this case not reflect the actual condition of the ROV in operation. In addition, other error sources are present in the acceleration measurements, such as scale-factors, orthogonality or misalignment errors, and bias offsets. If acceleration biases are not good enough compensated for, this will cause the position and velocity estimates to drift rapidly in between range measurements. Sufficient drift in the position

and velocity estimate can cause choppy estimates. This is perhaps most obvious in the position and velocity estimation error from experiment I, seen in Figure 7.2 and 7.3.

The attitude estimate was needed in order to define the rotation matrix, for rotating acceleration measurements obtained in $\{b\}$ to the inertial frame, $\{n\}$. Errors in the attitude estimate will results in an erroneous gravity compensation, which will deteriorate the acceleration measurements, as discussed in Section 7.3.3. During experiments the QMT system was used to obtain the orientation, which is very accurate. Under more realistic conditions, the attitude will need to be estimated, based on other IMU data, and might not be as accurate. However, Qualisys did suffer from drop-outs in the experiments performed. And in experiment II Qualisys, providing the attitude estimate, was logged only at 5 Hz. It was clearly visible in the results from experiment II, how both the position and velocity estimate was affected by inaccurate and outdated attitude estimates.

8.2.1 Acceleration bias estimation

In Figure 7.5 and 7.15 the steady-state acceleration bias estimates are plotted. For experiment I the IMU was calibrated on beforehand, and the estimated biases oscillate around quite small values. The IMU in experiment II was not calibrated, and in addition sudden attitude jumps during the experiment caused the bias estimates to converge to quite large values. With a faster logging of attitude, and perhaps a more smooth movement of the ROV, it is expected that the acceleration bias estimation would be more similar to the bias estimation in simulations, see Figure 6.5. This means that the drift in the position and velocity estimate will be somewhat compensated for, even though the IMU is not calibrated on beforehand.

Chapter 9

Conclusion

In this thesis two different filters have been presented to solve integration of inertial and pseudo-range measurements, that could be suited for underwater navigation of an ROV. The purpose is to estimate position, velocity, wave speed and acceleration biases.

Simulations were carried out to verify the implementation of the two filters, and to compare their performance in steady-state and in transient behavior. The filters showed very similar performance in steady-state, measured in form of the RMS position estimation error and based on the plotted states. In transient behavior all TSF estimates converged faster than the EKF. Simulations were also used to evaluate the time it took to compute the estimates produced by the filters. It was found that the execution time for the TSF was more than twice as long as for the EKF.

Experiments were conducted in the test basin in the MC-laboratory at Tyholt, using a Videoray ROV and a SeaBotix ROV. Two different sensor systems were used to generate range measurements, and all relevant measurements were logged during the experiments. Offline runs were done to test once again the steady-state and transient behavior of the filters. Overall, the results using experimental data showed many of the same trends as those observed in simulations. The TSF and EKF behaved similarly in steady-state, while the TSF estimates converged faster in transient state.

The EKF is currently the standard choice for integration of measurements for nonlinear estimation problems. It is argued that the additional work it took to implement the TSF, was not much, because the third stage of the TSF and the EKF is so similar. Also, the work of re-tuning the EKF in transient behavior proved to be more challenging and time-consuming than for the TSF. While the performance of the EKF was sensitive to the tuning of P(0), the performance of the TKF was less dependent on tuning. The

TSF therefore proved to be more robust when it came to inaccurate initialization. The stability proof for the TSF also guarantees the state estimates will converge, because it is globally stable, while the EKF could possibly diverge.

The performance of the filters could vary beyond what has been found in this thesis, due to uncertainties related to the "true values" available during experiments, tuning of the filters or variations that come with different transponder set-ups. However, results from both simulations and two different experiments indicate good performance of the TSF when benchmarked against the EKF. To conclude, the TSF, based on the investigation done in this thesis, is recommended for the estimation problem considered. This inspires further work to continue examining the performance and the potential of the TSF in use for underwater navigation of ROVs.

Chapter 10

Further work

One of the general trends observed in both simulation and experimental results, was that the RMS error was always largest in Down. For subsea navigation problems, the vertical DOP will typically be poor, as the underwater vehicle in operation most likely will operate with little elevation with respect to the transponder network. A depth measurement is therefore an effective method to improve the estimation accuracy in Down, and is in practice always available on an underwater vehicle. A new formulation must then be developed for the measurement matrix in the LTV KF in the second stage of the TSF, to include the depth measurement. And consequently the sensor covariance matrix must be established for this formulation. The depth measurement could also be exploited in the algebraic transformation, as done in the work by (Jørgensen et al., 2016), to increase robustness with respect to pseudo-range measurements.

An other improvement that would also increase robustness with respect to pseudo-range measurements noise, is an additional step for calculating the correct solution to the second order equation of r, see Section 4.4.1. Jørgensen et al. (2016) proposes to solve an nonlinear optimization problem to determine the correct solution of r. And in the same optimization the noise in r is modelled using a numerical method, as opposed to this formulation, where r is assumed noise-free. This strategy is assumed to increase the performance of the 2^{nd} stage LTV KF.

A truly realistic navigation system will use the estimated attitude for rotating the acceleration measurements. This will require some reconstructing of the filter, and the attitude must then be estimated based on other IMU data. It would be interesting to do further experimental testing with this modification.

Bibliography

I. Fossen Thor A. Johansen, Tor. Nonlinear observer for inertial navigation aided by pseudo-range and range-rate measurements. *European Control Conference (ECC)*, 2015. doi: 10.1109/ECC.2015.7330778.

Tor A. Johansen, Thor I. Fossen, and Graham C. Goodwin. Three-stage filter for position estimation using pseudo-range measurements. *IEEE Transactions on Aerospace and Electronic Systems*, 52(4):1631–1643, 2016.

Bent Oddvar Arnesen and Ingrid Schjølberg. *Motion Control Systems for ROVs - Underwater Path-Following for a Videoray Pro 4 ROV*. Thesis, 2016.

AtlantasMarine. URL `http://www.atlantasmarine.com/product/videoray-pro-4`. (Accessed 08.04.2017).

Bård B. Stovner, Tor A. Johansen, Thor I. Fossen, and Ingrid Schjølberg. Three-stage filter for position and velocity estimation from long baseline measurements with unknown wave speed. *American Control Conference*, 2016.

Pedro Batista. Ges long baseline navigation with unknown sound velocity and discrete-time range measurements. *Control Systems Technology, IEEE Transactions on*, 23(1): 219–230, 2015. ISSN 1063-6536. doi: 10.1109/TCST.2014.2321973.

Pedro Batista, Carlos Silvestre, and Paulo Oliveira. A sensor-based long baseline position and velocity navigation filter for underwater vehicles. *IFAC Proceedings Volumes*, 43 (14):302–307, 2010. ISSN 1474-6670. doi: 10.3182/20100901-3-IT-2016.00173.

Mohammadreza Bayat and A. Pedro Aguiar. Observability analysis for auv range-only localization and mapping measures of unobservability and experimental results. *IFAC Proceedings Volumes*, 45(27):325–330, 2012. ISSN 1474-6670. doi: 10.3182/20120919-3-IT-2046.00055.

BlueSolutions. URL `https://www.bluesolution.no/`. (Accessed 02.05.2017).

James C. Kinsey, Ryan M. Eustice, and Louis L. Whitcomb. A survey of underwater vehicle navigation: Recent advances and new challenges. 2006.

Mauro Candeloro, Asgeir J. Sørensen, Sauro Longhi, and Fredrik Dukan. Observers for dynamic positioning of rovs with experimental results. *IFAC Proceedings Volumes*, 45 (27):85–90, 2012. ISSN 1474-6670. doi: 10.3182/20120919-3-IT-2046.00015.

Chi-Tsong Chen. *Linear system theory and design*. The Oxford series in electrical and computer engineering. Oxford University Press, New York, international 4th ed. edition, 2013. ISBN 9780199959570.

Robert D. Christ and Sr Robert L. Wernli. *The ROV Manual : A User Guide for Remotely Operated Vehicles*. ROV Manual - A User Guide for Remotely Operated Vehicles. Elsevier Science, Burlington, 2nd ed. edition, 2013. ISBN 0-08-098288-3.

Fredrik Dukan. *ROV motion control systems*. Phd thesis, Norwegian University of Science and Technology, Faculty of Engineering Science and Technology, Department of Marine Technology, 2014.

Thor I. Fossen. *Handbook of marine craft hydrodynamics and motion control = Vademecum de navium motu contra aquas et de motu gubernando*. Vademecum de navium motu contra aquas et de motu gubernando. Wiley, Chichester, 2011. ISBN 9781119991496.

Thor I. Fossen. Low-cost integrated navigation systems for autonomous underwater vehicles. *XXXIII Jornadas de Automatica , 5-7 September, Vigo, Spain*, 2012.

Paul D. Groves. *Principles of GNSS, inertial, and multi-sensor integrated navigation systems*. Artech House, Boston/ London, 2008. ISBN 9781580532556.

Øyvind Hegrenas, Kenneth Gade, Ove Kent Hagen, and Per Espen Hagen. Underwater transponder positioning and navigation of autonomous underwater vehicles. pages 1–7, 2009. ISSN 978-1-4244-4960-6.

Tor A. Johansen and Thor I. Fossen. The exogenous kalman filter (xkf). *International Journal of Control*, pages 1–7, 2016a. ISSN 0020-7179. doi: 10.1080/00207179.2016.1172390.

Tor A. Johansen and Thor I. Fossen. Nonlinear filtering with exogenous kalman filter and double kalman filter. *European Control Conference, Aalborg*, 2016b.

Erlend K. Jørgensen, Tor A. Johansen, and Ingrid Schjølberg. Enhanced hydroacoustic range robustness of three-stage position filter based on long baseline measurements

with unknown wave speed. *IFAC PapersOnLine*, 49(23):61–67, 2016. ISSN 2405-8963. doi: 10.1016/j.ifacol.2016.10.322.

R. E. Kalman. A new approach to linear filtering and prediction problems. *Journal of Basic Engineering*, 82(1):35, 1960. ISSN 00219223. doi: 10.1115/1.3662552.

R. E. Kalman and R. S. Bucy. New results in linear filtering and prediction theory. *Journal of Basic Engineering*, 83(1):95, 1961. ISSN 00219223. doi: 10.1115/1.3658902.

Hassan K. Khalil. *Nonlinear Control, Global Edition*. Nonlinear Control. Pearson Education Limited, 2015. ISBN 1-292-06050-6.

N. H. Kussat, C. D. Chadwell, and R. Zimmerman. Absolute positioning of an autonomous underwater vehicle using gps and acoustic measurements. *Oceanic Engineering, IEEE Journal of*, 30(1):153–164, 2005. ISSN 0364-9059. doi: 10.1109/JOE.2004.835249.

Martin Ludvigsen. *An ROV toolbox for optical and acoustical seabed investigations*. Phd thesis, Norwegian University of Science and Technology, Faculty of Engineering Science and Technology, Department of Marine Technology, 2010.

M. Morgado, P. Oliveira, and C. Silvestre. Tightly coupled ultrashort baseline and inertial navigation system for underwater vehicles: An experimental validation. *Journal of Field Robotics*, 30(1):142–170, 2013. ISSN 1556-4959. doi: 10.1002/rob.21442.

Liam Paull, Sajad Saeedi, Mae Seto, and Howard Li. Auv navigation and localization: A review. *Oceanic Engineering, IEEE Journal of*, 39(1):131–149, 2014. ISSN 0364-9059. doi: 10.1109/JOE.2013.2278891.

Jan Rohac, Martin Sipos, and Jakub Simanek. Calibration of low-cost triaxial inertial sensors. *Instrumentation Measurement Magazine, IEEE*, 18(6):32–38, 2015. ISSN 1094-6969. doi: 10.1109/MIM.2015.7335836.

Elaine Rowan. Lbl underwater positioning. *Hydro International*, 12(1):18–21, 2008. ISSN 13854569.

Stian Skaalvik Sandøy, Roger Skjetne, Hans-Martin Heyn, and Mauro Candeloro. *System Identification and State Estimation for ROV uDrone*. Thesis, 2016.

Ingrid Schjølberg and Ingrid Bouwer Utne. Towards autonomy in rov operations. *IFAC PapersOnLine*, 48(2):183–188, 2015. ISSN 2405-8963. doi: 10.1016/j.ifacol.2015.06.030.

Ingrid Schjølberg, Tor B. Gjersvik, Aksel A. Transeth, and Ingrid B. Utne. Next generation subsea inspection, maintenance and repair operations. *IFAC PapersOnLine*, 49 (23):434–439, 2016. ISSN 2405-8963. doi: 10.1016/j.ifacol.2016.10.443.

SNAME. *Code on maneuvering and special trials and tests 1950.* SNAME, New York, 1950.

Bård B. Stovner, Tor A. Johansen, and Ingrid Schjølberg. Globally exponentially stable aided inertial navigation with hydroacoustic measurements from a single transponder. *American Control Conference (ACC)*, vol. 37, 2017.

Asgeir J. Sørensen. *Marine control systems : propulsion and motion control of ships and ocean structures*, volume UK-2013-76 of *Kompendium (Norges teknisk-naturvitenskapelige universitet. Institutt for marin teknikk).* Department of Marine Technology. Norwegian University of Science and Technology, Trondheim, 2013.

Francisco C. Teixeira and António M. Pascoal. Geophysical navigation of autonomous underwater vehicles using geomagnetic information. *IFAC Proceedings Volumes*, 41(1): 178–183, 2008. ISSN 1474-6670. doi: 10.3182/20080408-3-IE-4914.00032.

Sebastian Thrun, Wolfram Burgard, and Dieter Fox. *Probabilistic robotics.* Intelligent robotics and autonomous agents. MIT Press, Cambridge, Mass, 2005. ISBN 0262201623.

VectorNav. URL `http:www.vectornav.comdocsdefault-sourcedocumentationvn-100-documentation/UM001.pdf?sfvrsn=12`. (Accessed 11.04.2017).

Sarah Webster, Ryan Eustice, Hanumant Singh, Louis Whitcomb, and Sarah Webster. Advances in single-beacon one-way-travel-time acoustic navigation for underwater vehicles. *International Journal of Robotics Research*, 31(8):935–950, 2012. ISSN 0278-3649. doi: 10.1177/0278364912446166.

Appendix A

IMU accelerometer calibration

The IMU accelerometers on the Videoray, used in experiment I, were calibrated using a calibration algorithm made by Rohac et al. (2015). The Sensor Error Model (SEM) is defined according to (A.1)

$$u_a = T_a S_a (y_a - b_a) \tag{A.1}$$

where y_a is the measured acceleration data. And the result from the calibration script was

$$T_a = \begin{bmatrix} 1 & 0 & 0 \\ 0.0230 & 1 & 0 \\ -0.0834 & 0.0173 & 1 \end{bmatrix} \tag{A.2}$$

$$S_a = 1e-05 \cdot \begin{bmatrix} 0.1005 & 0 & 0 \\ 0 & 0.08130 & \\ 0 & 0 & -0.0494 \end{bmatrix} \tag{A.3}$$

$$b_a = \begin{bmatrix} -0.0408 \\ 0.0026 \\ -0.1295 \end{bmatrix} \tag{A.4}$$

It is worth mentioning that the gravity component present in the accelerometer measurements was estimated by the calibration algorithm, and therefore not compensated for in the filter. Gravity compensation was then already done when using the compensated

acceleration measurements, u_a.

Appendix B

Attachments

Appendix A contains the attachments to this thesis, which are stored in a ZIP-file delivered electronically together with the thesis. The file includes the following folders:

B.1 Poster

The A2 poster (2 x A3) has been included in .pdf-format, and is found in the folder *Poster*.

B.2 Simulator

All MATLAB codes needed to run simulations can be found in the folders *Simulation 1* and *Simulation 2*. Both folders also include a *figures* folder, which contain relevant figures generated from simulations results.

B.3 Experiments

The experimental results were based on logged measurement data, that were tested in the integration filters. For each experiment, all needed data, as well as scripts for reading this, are included so that offline tests can be re-run.

B.3.1 Experiment I

In *Experiment I* the relevant measurement data was stored as .mat-files. The nonlinear Gaussian transformation, for finding the variance of the noise present in the constructed range measurements, was performed using the script *covariance_range.m*. Within this folder, a *figures* folder contain all figures generated from offline results.

B.3.2 Experiment II

In *Experiment II*, all relevant measurement data was read from -txt-files. Within this folder, a *figures* folder contain all generated figures generated from offline results.